UNDERSTANDING EARTHQUAKE TRIGGERING AND FAULT SLIP BEHAVIOR BASED ON IMPROVED EARTHQUAKE CATALOGS

A Dissertation
Presented to
The Academic Faculty

by

Dongdong Yao

In Partial Fulfillment
of the Requirements for the Degree
DOCTOR OF PHILOSOPHY in the
School of Earth and Atmospheric Sciences

Georgia Institute of Technology
August 2018

UNDERSTANDING EARTHQUAKE TRIGGERING AND FAULT SLIP BEHAVIOR BASED ON IMPROVED EARTHQUAKE CATALOGS

Approved by:

Dr. Zhigang Peng, Advisor
School of Earth and Atmospheric Sciences
Georgia Institute of Technology

Dr. Yao Xie
School of H. Milton Stewart School of Industrial and Systems Engineering
Georgia Institute of Technology

Dr. Andrew V. Newman
School of Earth and Atmospheric Sciences
Georgia Institute of Technology

Dr. James H. McClellan
School of Electrical and Computer Engineering
Georgia Institute of Technology

Dr. Ken L. Ferrier
School of Earth and Atmospheric Sciences
Georgia Institute of Technology

Date Approved: July 28, 2018

To My Family

ACKNOWLEDGEMENTS

I would like to first thank my advisor Dr. Zhigang Peng for his patience and guidance of my doctoral work. When I started my Ph.D. work 6 years ago, I had no prior experience in processing large volume of seismic data. He worked with me from the beginning to overcome many challenges during all these years. I would also like to express my sincere gratitude to Dr. Andrew Newman for the opportunity to work on the Nicoya dataset, and his criticism and help to my research and academic studies. Last but not the least, I want to thank my committee members, Dr. Ken Ferrier, Dr. Yao Xie and Dr. James McClellan for their valuable discussions and comments.

Many collaborators provide useful suggestions/comments during my PhD study. Without their help, I don't think I can finish this work. These include Dr. Xiaofeng Meng, Dr. Jacob I. Walter, (soon to be Dr.) Tiegan E. Hobbs, Dr. Jing Wu, Dr. Lu Li, Dr. Susan Y. Schwartz, Dr. Marino Protti, Dr. Bill Fry, Dr. Yoshihiro Kaneko, Xiang Ruan, and Dr. Feng Long. I also would like to thank many colleagues and friends in Georgia Tech and other institutes for their support, including Dr. Zefeng Li, Dr. Chastity Aiken, Dr. Shuozhi Xu, Dr. Yanqing Su, (soon to be Dr.) Xin Cao, Chenyu Li, (soon to be Dr.) Longlei Li, Qiushi Zhai, Dr. Amy Williamson, Dr. Mary Beth Wilhelm, Dr. Lujendra Ojha, Jinxin Hou, Dr. Libo Han, and (soon to be Dr.) Hao Guo.

Finally, I would like to thank my parents, my brother Jin Yao and sister Lei Yao for their selfless love and faith in me.

TABLE OF CONTENTS

LIST OF FIGURES

SUMMARY

Large earthquakes can alter the subsurface stress field on active faults across broad spatial and temporal windows, which would promote or inhibit slip on these faults. Besides dynamic ruptures during regular earthquakes, faults can also slip at a steady rate without any seismic radiation. In between these two extremes, slow slip events have been documented within the conditionally stable transition zone. Recent advancements in seismic instrumentation and computer programs provide an unprecedented opportunity to capture weak seismic events, and the resulting complete catalogs can be used to understand physical mechanisms of earthquake interactions from nearby to long-range distances, as well as diverse faulting processes inside the Earth.

Earthquakes are routinely picked and located by analysts at seismic network centers. However, a significant fraction of events are missed, especially during intensive aftershock or swarm sequences. These missing events can be detected by a semi-automatic template matching method, which uses waveforms of existing events as templates to scan through continuous data for new events with high similarities.

This dissertation focuses on improved understanding of fault slip behaviors and earthquake interactions based on improved catalogs from the template matching method. I first present studies on earthquake interactions in both continental-continental (Tibet) and oceanic-continental (North Island of New Zealand and Nicoya Peninsula) convergent environments following large mainshocks at nearby and far-field distances. The obtained results suggest that transient stress carried by passing seismic waves can trigger fault slip at long-range distances, and the aftershock sequence can be driven by continuing fault

slip following the mainshock rupture. The second group of studies focuses on seismic activities prior to the 2008 M_w 7.9 Wenchuan earthquake, as well as the 2010 M_w 7.2 El Mayor-Cucapah earthquake. The primary target is to decipher diverse fault slip behaviors and understand their roles in mainshock nucleation.

In the following chapters, I first introduce the matched filter technique in CHAPTER 1, which utilizes waveforms of known catalog events as prior "matched filters" to cross correlate with continuous recordings to identify events with similar waveforms. This method has been widely applied to improve standard catalogs by detecting missing seismic events with low signal-to-noise ratios, including foreshocks, early aftershocks, earthquake swarms and low frequency earthquakes within deep tectonic tremors. Moreover, cross-correlated differential travel times can be extracted to further improve the relative locations of the improved catalog. The relative amplitudes between template and detected events can also be used to constrain their relative magnitudes.

In CHAPTER 2 [*Yao et al.*, 2015], I investigate the potential link between the 2005 M_w 6.3 Zhongba earthquake (2005/04/07 20:04:41 UTC) in South-Central Tibet and the 2005 M_w 8.6 Nias-Simeulue earthquake (2005/03/28 16:09:36 UTC) off the west coast of Northern Sumatra. Their close timings may indicate a delayed-triggering relationship at long-range distances. Moreover, a visual inspection of 5 Hz high-pass filtered waveforms reveals many locally triggered earthquakes during or immediately following large amplitude surface waves of both 2004 M_w 9.1 Sumatra-Andaman and 2005 M_w 8.6 Nias earthquakes. After manually picking their P- and S-wave arrivals, many of them were located near Gaize, ~200 km further north relative to the 2005 M_w 6.3 Zhongba earthquake. To further investigate the seismicity pattern, I apply the matched filter

technique to detect earthquakes near Zhongba and Gaize around the 2004 Sumatra and 2005 Nias events. The detected catalogs show no clear change of seismicity near Zhongba following both distant mainshocks. In comparison, the seismicity rate near Gaize increased significantly right after the passage of Rayleigh waves, lasting for hours to days followed by a relative quiescence and then returned to the background level. This study highlights the need to have better local station coverage in order to better understand the remote triggering relationship.

In CHAPTER 3 [*Yao et al.* (under review)], I conduct a systematic search for dynamically triggered earthquakes in the North Island of New Zealand following the November 13th, 2016 M_w 7.8 Kaikoura earthquake in the northern portion of the South Island (~300-600 km away). I carefully select template events, and apply the matched filter technique to obtain a more complete catalog within one month around the mainshock. Two types of responses to dynamic stress perturbation from the mainshock are observed. Abundant triggered earthquakes occurred immediately following the mainshock in the shallow crust around the Taupo Volcanic Zone, likely related to the activation of crustal faults associated with back-arc rifting and volcanism. In comparison, a burst of seismicity (including a M_L 5.55 mainshock) occurred ~8.5 days later along the shallow subduction interface near Porangahau off the Wairarapa coast. This burst of seismicity is associated with a ~M_w 7.1 shallow slow slip event dynamically triggered by the mainshock. These results highlight the heterogeneous nature of dynamic triggering in a plate boundary region that has been subject to recent large earthquake sequences and aseismic transients.

In CHAPTER 4 [*Yao et al.*, 2017], I apply the waveform matching technique to obtain a detailed earthquake catalog following the 5 September 2012 M_w 7.6 Nicoya earthquake in Central America. Starting from a preliminary catalog, I relocate ~7,900 events using the earthquake location package TomoDD to better quantify their spatio-temporal behaviors. Relocated aftershocks are mostly clustered in two groups. The first is immediately above the major coseismic slip patch, partially overlapping with shallow afterslip following the mainshock. The second one is 50 km SE of the mainshock nucleation point and near the terminus of the coseismic rupture, in a zone that exhibited little resolvable afterslip. Using the relocated events as templates, I scan through the continuous recording from 29 June 2012 to 30 December 2012, detecting approximately 17 times more than template events. I find 190 aftershocks in the first half hour following the mainshock, mostly along the plate interface. Later events become more scattered in spaces, showing moderate expansion in both along-trench and down-dip directions. These observations suggest that transient loading from nearby afterslip along the plate interface drives spatio-temporal evolution of aftershocks just above the mainshock rupture patch, while aftershocks in the SE group are to the SE of the observed afterslip and their physical mechanisms are not well constrained.

In CHAPTER 5 of my dissertation [*Yao et al.* (in prep)], I examine the background seismicity around the 2008 M_w 7.9 Wenchuan earthquake in Southwest China, and its relationship to the nearby Zipingpu water reservoir. I first locate ~2,630 catalog events based on manually picked arrivals using an absolute earthquake location software called Hypoinverse. A refined and more complete catalog from 2004/10/01 to 2007/12/31 is obtained via waveform matching detection and subsequent relocation with the double-

difference relative location package HypoDD. Specifically, ~7,700 more events are detected and ~7,100 are further relocated with waveform cross-correlated differential times. The results show a clear increase of shallow seismicity following the initial impoundment on steeply dipping faults to the southwest of the reservoir, and the correlation between the seismicity rate and the change of water level is clear. In comparison, the northeastern region was active prior to the impoundment, likely being obscured by events from anthropogenic activities. Moreover, the resolved hypocentral depth of the mainshock initiation is above 10 km using the reservoir network, shallower than previous determined depths using regional and teleseismic stations. These results suggest that the impoundment of the Zipingpu reservoir changed the seismicity pattern around the epicentral region, and likely promoted the occurrence of the Wenchuan mainshock.

In CHAPTER 6 [*Yao et al.* (in prep)], I study the foreshock sequence preceding the 2010 M_w 7.2 El Mayor-Cucapah earthquake in Baja California, Mexico. This sequence contains several clusters, and many foreshocks were reported within a few kilometers of the mainshock epicenter, with magnitudes ranging from M 1.5 to M 4.4. I use 76 events as templates to scan through the continuous waveforms starting from 21 days before and up to the mainshock to detect possible missing events. I also relocate the foreshock sequence by combining stations in both the Southern California Seismic Network (SCSN) and the Red Sísmica del Noroeste de México (RESNOM). The relocated seismicity shows that an earthquake swarm immediately before the mainshock occurred in a smaller region surrounding the mainshock epicenter, while seismicity two or more days earlier distributes across a broader area. This space-time evolution may indicate that foreshocks

were likely driven by certain aseismic processes that eventually lead to the mainshock rupture.

In CHAPTER 7, I introduce an ongoing effort to investigate aseismic slip using repeating earthquakes, which rupture nearly the same fault patches and are likely driven by aseismic deformation process. I compare different ways to export repeating pairs, and discuss the possibility of combining with further event detection using NMFT. Some preliminary results of searching for repeaters along the central San Jacinto Fault are shown as well.

Finally, I summarize major findings from these studies, discuss limitations of the current methods and future work in the last CHAPTER 8.

CHAPTER 1. INTRODUCTION

1.1 An overview of earthquake triggering

Earthquake occurs when the shear stress along a fault interface exceeds its frictional resistance, also known as Coulomb failure criterion [*Scholz*, 1990]. External stress perturbations can promote failure on critically stressed fault systems by increasing static stress, lowering the resistance or a combination of both. For instance, aftershocks seem to occur in regions of elevated static stress changes [*King et al.*, 1994; *Stein et al.*, 1997], and earthquakes can also be triggered or induced by fluid injection [*Ellsworth*, 2013] passing seismic waves [*Kilb et al.*, 2000; *Gomberg et al.*, 2001], tidal stress [*Cochran et al.*, 2004], and atmospheric pressure changes [*Gao et al.*, 2000; *Liu et al.*, 2009]. In addition, external stress perturbations can prohibit failures where faults are relaxed or put into the so-called stress shadow [*Harris and Simpson*, 1998].

Currently the most well documented cases of triggering studies are earthquake-earthquake interactions [*Hill and Prejean*, 2015]. The triggering mechanisms include static stress change from fault displacement field, quasi-static stress change from postseismic deformation, or dynamic stress change carried by passing seismic waves. The relative contribution of above mechanisms is likely determined by a combination of distance and time: static and quasi-static stress changes decrease rapidly with distances (i.e., r^{-3}), and become negligible at remote distances [*Freed*, 2005]. In comparison, dynamic stress change is transient and decreases slowly with distance (i.e., $r^{-1.5}$) and dominates in triggering local seismicity at teleseismic distances [*Hill and Prejean*, 2015]

and possibly in the intermediate or near-field as well [*Kilb et al.*, 2002; *Felzer and Brodsky*, 2006].

1.2 Matched filter technique

Recent developments in data gathering, transmission and storage enable seismic stations to record continuously at much higher sampling rates and long durations. How to extract earthquake signals accurately and efficiently from the increasing amount of seismic data becomes a new challenge. Traditionally, earthquake data center or seismic observatory produces standard earthquake catalogs from the following routine steps: manual phase detection/picking, or automatic phase detection on continuous recording using one or more detectors, such as the short-term-average/long-term average function [*Allen*, 1982], followed by an event association based on calculated travel time grids. Analysts need to visually scan identified events and locate them by manually adjusting the phase picks. The above process can be time consuming and fails to detect events with either low signal-to-noise ratios (SNR) or short event recurrence intervals (i.e., high seismicity rates). Moreover, several recent studies have shown that improving earthquake catalog completeness can provide important new clues on earthquake nucleation, fault structure, earthquake statistics and interaction [e.g., *Peng et al.*, 2007; *Enescu et al.*, 2007; *Mignan*, 2014].

The recently developed network-based matched-filter technique (NMFT) [*Gibbons and Ringdal*, 2006] employs the waveform similarity to identify new events by cross-correlating clear *P*- and *S*-waveforms from existing catalog events with continuous recordings. It utilizes the fact that earthquakes close to each other produce similar

waveforms at the same station if their focal mechanisms and ray paths are similar. The method is suitable over a range of magnitudes and can be used to identify small events with low signal-to-noise ratios (SNR). The method was first used to identify LFEs within continuous tremor [*Shelly et al.*, 2007], and was later widely adopted to detect potentially missing aftershocks, foreshocks, induced earthquakes, and remotely triggered seismicity following large earthquakes [*Peng and Zhao*, 2009*; Yang et al.*, 2009; *Meng et al.*, 2013*; Meng and Peng,* 2016; *Kato et al.*, 2012; *Kato and Nakagawa*, 2014*; Wu et al.*, 2014*; Skoumal et al.*, 2014; *Walter et al.*, 2015*; Yao et al.*, 2015, 2017; *Li et al.*, 2017, 2018].

1.3 Thesis organization

The overarching goal of this thesis is to apply the NMFT to several regions to improve earthquake catalog completeness, and use the new catalogs to refine our understanding of earthquake triggering and fault slip behaviors (seismic vs. aseismic processes). The dissertation includes two published papers [*Yao et al.*, 2015; *Yao et al.*, 2017], one manuscript under review [*Yao et al.* (under review)], and several in preparation. In CHAPTER 2, I present a study of remote dynamic triggering in South-Central Tibet following two M_w 8.5+ earthquakes in Northern Sumatra. CHAPTER 3 investigates different types of response in North Island of New Zealand to dynamic stress perturbation from the 2016 M_w 7.8 Kaikoura earthquake. In CHAPTER 4, I examine the aftershock sequence of the 2012 M_w 7.6 Nicoya mainshock by carefully relocating and detecting earthquakes. CHAPTER 5 focuses on evolution of microseismicity before the 2008 M_w 7.9 Wenchuan earthquake and its relationship with a nearby water reservoir. I also summarize results on the foreshock sequence of the 2010 M_w 7.2 El Mayor-Cucapah

earthquake in CHAPTER 6 and ongoing work on searching for repeaters along the central segment of San Jacinto Fault in CHAPTER 7.

CHAPTER 2. REMOTELY TRIGGERED EARTHQUAKES IN SOUTH-CENTRAL TIBET FOLLOWING THE 2004 M_W 9.1 SUMATRA AND 2005 M_W 8.6 NIAS EARTHQUAKE

2.1 Introduction

In this study, we conduct a systematical investigation of dynamic triggering in South-Central Tibet following the 12/26/2004 M_w 9.1 Sumatra and 03/28/2005 M_w 8.6 Nias earthquakes. These two events triggered numerous microearthquakes and tectonic tremors around the world [e.g., *West et al.*, 2005; *Miyazawa and Mori*, 2006; *Peng et al.*, 2009; *Ghosh et al.*, 2009; *Tang et al.*, 2010; *Chao et al.*, 2012]. We select South-Central Tibet mainly because the M_w 6.3 Zhongba earthquake occurred in this region on 04/07/2005, ~10 days after the Nias earthquake (Figure 2.1a). *Ryder and Bürgmann* [2011] speculated that the 2005 Zhongba earthquake may be delay-triggered by the Nias earthquake, due to their close timings. If true, the 10-day interval between the two events indicates that one or more secondary triggering mechanisms (e.g., triggered creep; fluid migration; fault weakening) may take place. Elevated seismic activities can be used to verify the existence of such secondary triggering mechanisms [*Anderson et al.*, 1994; *Papadopoulos*, 2002; *Shelly et al.*, 2011; *van der Elst et al.*, 2013]. Hence, a detailed examination of continuous waveforms is needed to determine the existence (or absence) of dynamic triggering and reveal possible connections between the two events.

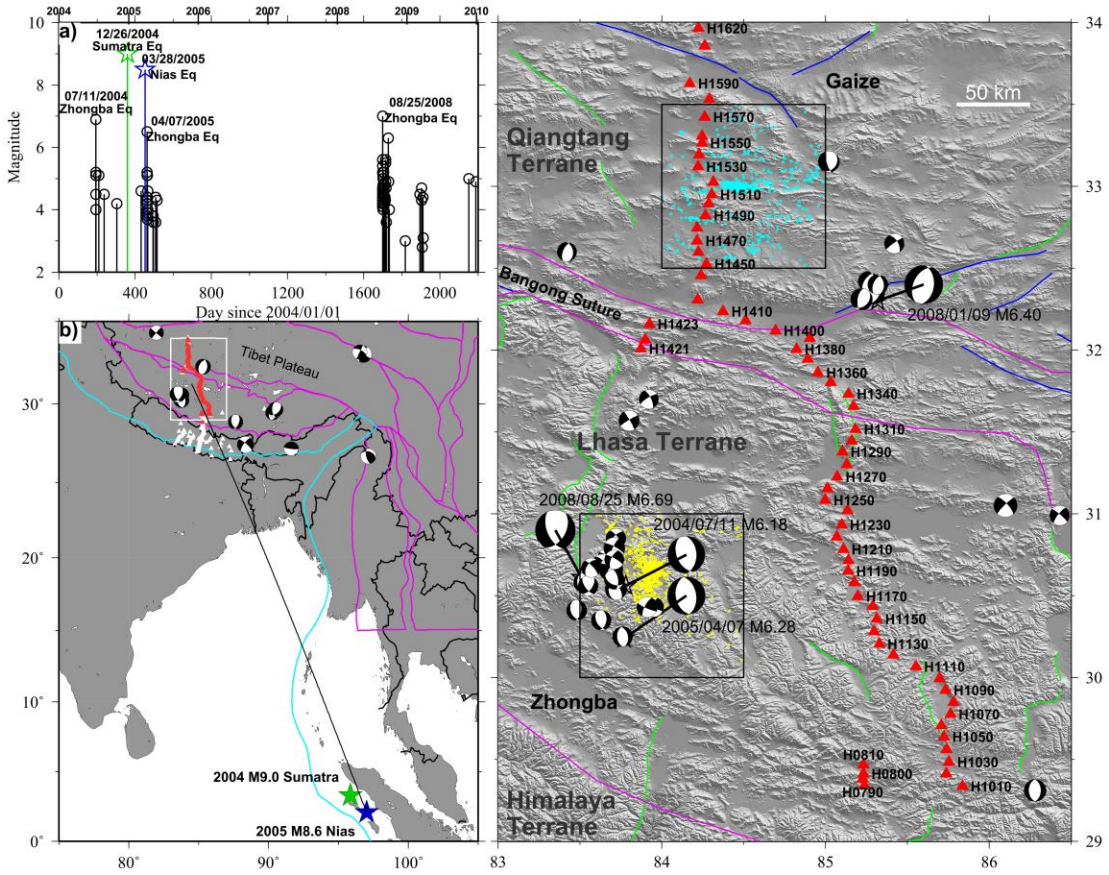

Figure 2.1 a) Magnitude versus time for catalog events from 2004 to 2009 near Zhongba. b) Map of Southeast Asia. Cyan and purple lines are major plate boundaries and major blocks in China. The study region is shown as the white rectangle, and the triangles are stations in Hi-CLIMB project. The stations marked in red recorded both Sumatra (green star) and Nias (blue star) mainshocks. Beachballs are focal mechanisms of events with magnitude larger than 6.0 in the past 30 years from the global CMT catalog. c) Map of study region in South-Central Tibet. Yellow and cyan dots mark events used in the waveform matched filter analysis. The focal mechanisms of the 2004, 2005 and 2008 Zhongba earthquakes and the 2008 Nima-Gaize earthquake are plotted. Smaller beachballs are available focal mechanisms of *M*<6 events from the CMT catalog in the past 30 years. Green and blue lines are normal and strike-slip faults in Tibetan Plateau, respectively [*Taylor and Yin*, 2009].

Previous studies on earthquake triggering mainly use microearthquakes based on manual phase picking [e.g., *Gomberg et al.*, 2004; *Peng et al.*, 2007; *Wu et al.*, 2011; *Aiken and Peng*, 2014], or automatic detectors [e.g., *Velasco et al.*, 2008] based on the short-time average/long-time average (STA/LTA) ratio method. However, manual picking can be time consuming, and while both methods provide timings and magnitudes,

they do not provide locations of the identified events. Recent studies mostly utilized a Network Waveform Matched Filter Technique (NWMFT) to detect remotely triggered seismicity following large distant earthquakes [*Yukutake et al.*, 2013; *Wang et al.*, 2015]. In this study, we used the same technique to detect missing local events in the South-Central Tibet around the origin times of the 2004 Sumatra and 2005 Nias earthquakes.

2.2 Study Region and Data

The continuous collision between the Indian Plate and the Eurasian Plate gives rise to the highest plateau in the world, the Tibetan Plateau [*Royden et al.*, 2008]. It consists of different terranes (Figure 2.1b), namely the Himalaya, Lhasa, Qiangtang, Songpan-Ganzi (or Bayan Har), and Kunlun terranes. The continental-continental convergence between the India and Eurasian plates causes relative motions among these terrains and makes Tibetan Plateau one of the most complex tectonic environments in the world. Recent geodetic studies indicate that the motion within the Tibetan Plateau is predominantly E-W extension and N-S shortening [*Zhang et al.*, 2004]. The occurrences of large normal faulting earthquakes with $M > 6.0$ in the past decade are consistent with this observation (Figure 2.1b). Among those normal faulting earthquakes, three occurred in Zhongba county in 2004, 2005 and 2008 [*Ryder et al.*, 2012], including the M_w 6.3 earthquake that occurred ~10 days after the 03/28/2005 M_w 8.6 Nias earthquake.

The Tibetan Plateau has been extensively instrumented by PASSCAL and other temporary seismic deployments since 1990s. From 2002 to 2005, the Himalayan-Tibetan Continental Lithosphere during Mountain Building (Hi-CLIMB) experiment (XF network) was conducted in South-Central Tibet, extending from the Ganges lowland, across the

Himalayas and onto the central Tibetan Plateau (Figure 2.1c). Over 200 sites were occupied during this experiment (Figure 2.1b and Figure 2.1c), providing unprecedented continuous recordings for imaging crustal and upper mantle structures in this region [*Nabelek et al.*, 2009]. This network also recorded the 2004 Sumatra and the 2005 Nias earthquakes and their numerous aftershocks. Figure 2.2a shows waveforms recorded at selected stations during the 2005 Nias mainshock. After applying a nominal 5 Hz high-pass filter, it is evident that many high-frequency signals occurred during and immediately following the large-amplitude surface waves. By comparing the envelope function (Figure 2.2b) and spectrogram (Figure 2.2c), we confirm that those are locally triggered earthquakes. After picking their *P*- and *S*-wave arrivals, many of these events were located north of the Bangong suture zone near Gaize. This finding motivated us to look further into the seismicity pattern in the Gaize region, as well as the epicentral region of the 2005 Zhongba earthquake.

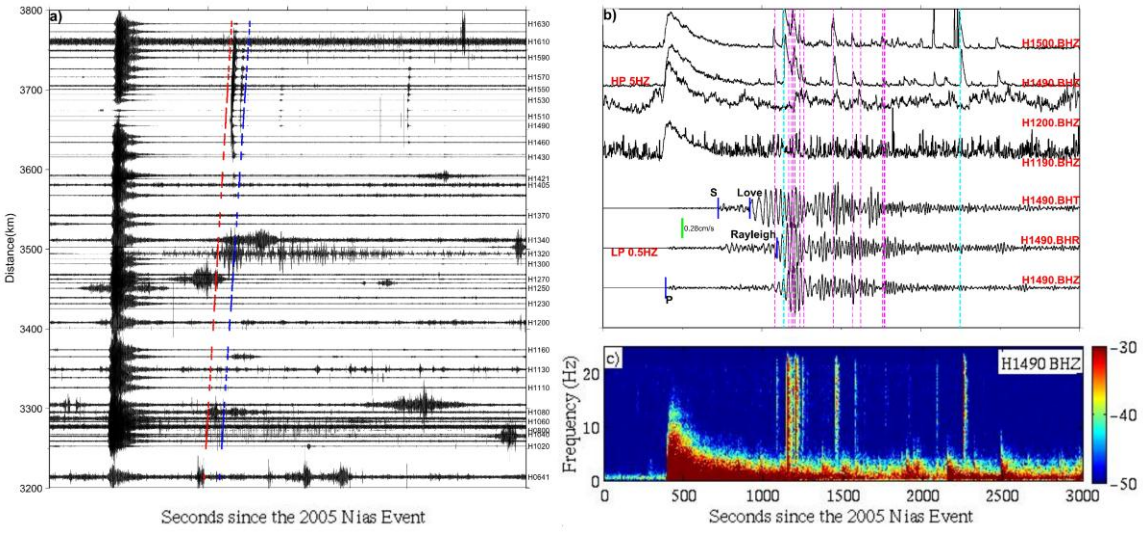

Figure 2.2 a) 5-Hz high-pass filtered vertical-component waveforms aligned with epicentral distances during the 2005 M_w 8.6 Nias mainshock. The dashed red and blue lines mark the predicted Love and Rayleigh wave arrival (with a nominal phase velocity of 4.1 and 3.5 km/s). b) Log10 envelope function of 5-Hz high-passed seismograms at stations near Gaize (H1490 and H1500) and Zhongba (H1190 and H1200). The bottom three traces are

broadband recordings rotating to transverse, vertical and radial components. *P, S,* Love and Rayleigh phases are marked. Pink vertical dashed lines denote detected events, and cyan lines denote templates used for detection. c) Spectrogram of vertical component recorded at station H1490.

2.3 Analysis Procedure

Our analysis procedure mainly follows that of *Wang et al*. [2015] and is briefly described here. Using the *Antelope* software, we first manually picked and located events within two 1°×1° grids: N30°-31° and E83.5°-84.5° around the Zhongba region and N32.5°-33.5°, E84°-85° around Gaize county (Figure 2.1c) between 12/01/2004 and 05/01/2005. We also computed their local magnitudes using the 'dbevproc' command within *Antelope*. During the 6-month study period, we obtained 623 and 547 events near Zhongba and Gaize, respectively. We then used these events as templates for waveform detection. We applied a bandpass filter of 2-10 Hz to both template and continuous waveforms in order to suppress teleseismic signals. We utilized a 12s time window (2s before and 10s after the S- and P-arrivals are used for the two horizontal channels and the vertical channel, respectively) to compute the cross-correlation coefficient (CCC) near Zhongba due to relatively large source-receiver distance. For templates near Gaize, we used a 5s time window (1s before and 4s after) to compute the CCC, mainly because most events occurred within 100 km of the array. Finally, we only employed channels of template waveforms with signal-to-noise ratio (SNR) no less than 5, following *Peng and Zhao* [2009].

We defined the detection threshold as the mean CCC plus 12 times the Median Absolute Deviation (MAD) near Zhongba. Since there are fewer stations near Gaize, we used a higher detection threshold (i.e., 15 times MAD) in this region to remove possible

false detections due to the small number of stations. We assigned the epicenter of a detected event to be the same as the corresponding template with the highest CCC value [*Peng and Zhao*, 2009]. In addition, we estimated local magnitudes of detected events by computing the peak *S*-wave amplitude ratio of the detected and corresponding template events. Figure 2.3 shows an example of a positive detection near Zhongba. The template event has a local magnitude of 3.74 and occurred on 04/08/2005, 10:47:04. The detected event occurred earlier on the same day at 01:25:21, and the inferred local magnitude is 2.34. The detected event is not identified manually, mainly because of its relative low SNR.

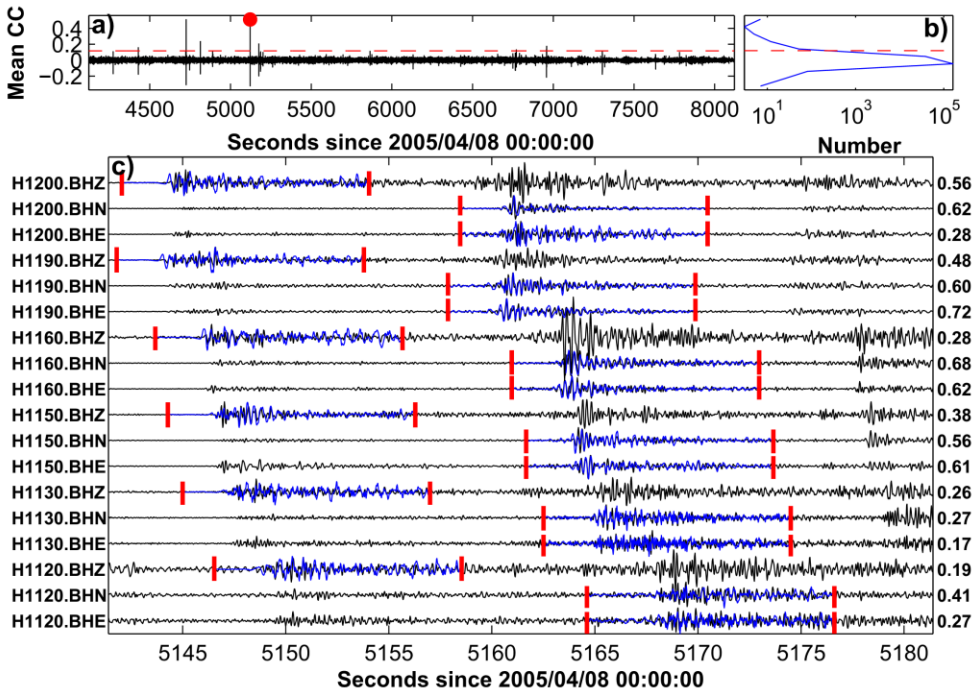

Figure 2.3 An example of positive detection by template 20050408104704 (*M*3.74) with mean cross-correlation coefficient (CCC) =0.583 and an inferred local magnitude 2.34. a) Distribution of CCC value 1000s before and 3000s after the origin time of the detection (red circle). Red dashed line marks the threshold for positive detections (12 times the median absolute deviation). b) Histogram of the CCC value. c) Waveform comparison of template waveforms (blue) and continuous waveforms (black). The station name and channel as well as corresponding CCC value are shown on both sides.

2.4 Results

2.4.1 *Detection result near Zhongba*

Using 623 earthquakes near Zhongba as templates, we detected a total of 1100 and 6453 events around the 2004 Sumatra event (12/25/2004-01/09/2005) and 2005 Nias event (03/21/2005-04/14/2005), respectively. We computed the magnitude of completeness (M_c) for the detected catalogs using the best-combined method in ZMAP [*Wiemer*, 2001]. The obtained values are 1.1 and 1.7 around the Sumatra and Nias mainshocks, respectively (Figure 2.4). Although we detected 6453 events around the 2005 Nias mainshock in Zhongba, 6278 of them (~95%) occurred shortly after and around the epicenter of the 2005 Zhongba event, which are considered as its aftershocks. We found no clear change in seismic activity between the 2005 Nias and 2005 Zhongba earthquakes, nor did we observe a clear change in seismic activity following the 2004 Sumatra earthquake (Figure 2.5). We evaluated the significance of seismicity changes by computing the β-value (Eq. 1),

$$\beta = \frac{N_a - N(T_a / T)}{\sqrt{N(T_a / T)(1 - T_a / T)}} \qquad \text{(Eq. 1)}$$

which measures the differences between the observed numbers of events after a mainshock and the predicted numbers based on the rates before the mainshock [*Matthews and Reasenberg*, 1988; *Aron and Hardebeck*, 2009]. If the resulting β-value is greater than 2, it indicates a significant increase in the seismicity rate. A significant decrease occurs when the β-value is smaller than –2. We computed the β-value in the time windows of 1 to 24 hours after the mainshocks with 1-hour increment (Figure 2.6). To

avoid potential bias in the resulting β-value with different pre-mainshock time windows, we used the longest pre-mainshock time to estimate the background rate (250 hours before Sumatra and 180 hours before Nias). The resulting β-value shows moderate to significant decrease of seismicity rate following the two mainshocks in all time windows (Figure 2.6a and Figure 2.6b), confirming our visual observation.

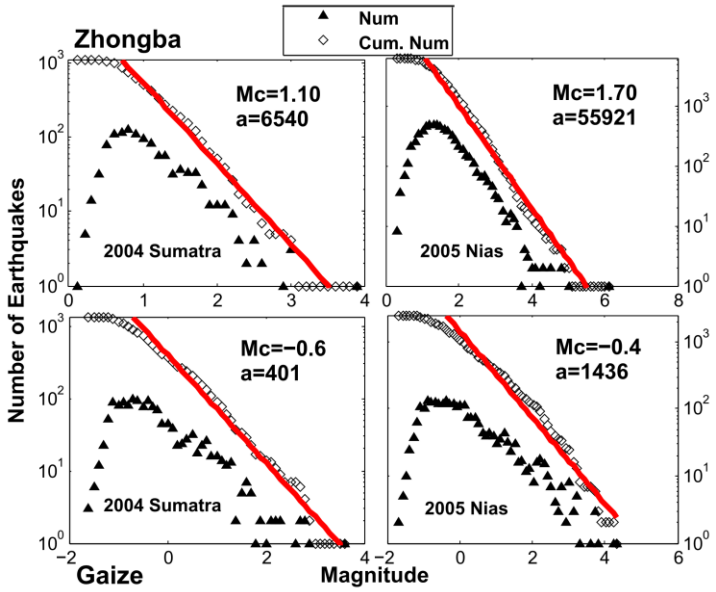

Figure 2.4 Gutenberg-Richter (G-R) relationship at different space-time windows. Diamonds show the cumulative number of earthquakes; black triangles are number of events for different magnitude bins. Top two panels show detected catalogs around the 2004 Sumatra and 2005 Nias events near Zhongba, and bottom two are near Gaize. Red bold curves are maximum-likelihood G-R fitting. The *Mc* and a values are labeled in each panel.

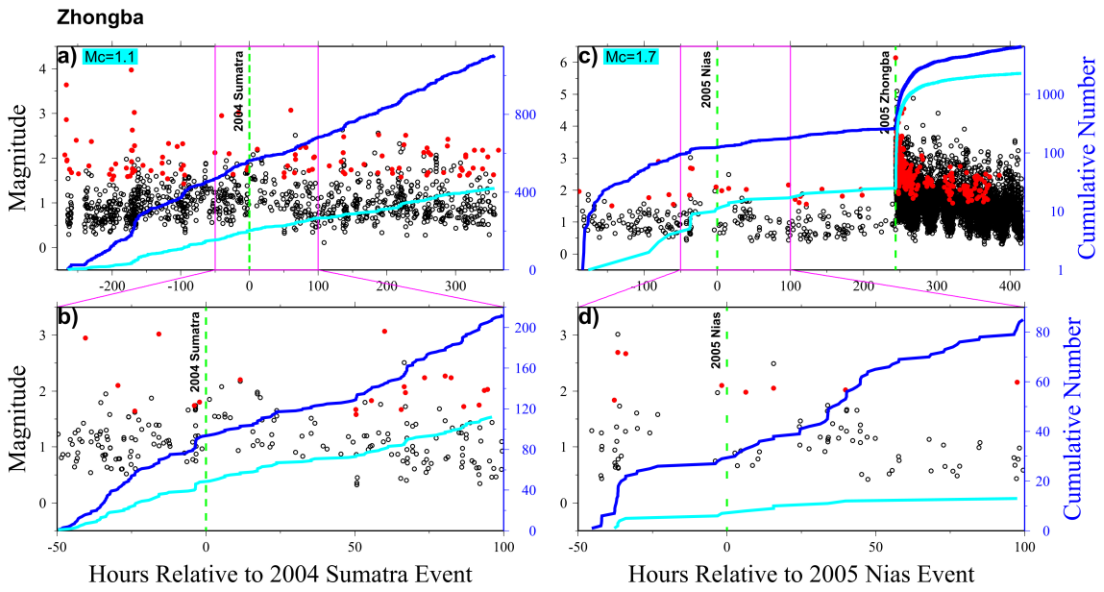

Figure 2.5 Detection results near Zhongba. a) Magnitude versus origin time of detected events around the 2004 Sumatra event. The red dots mark the template events. Blue and cyan lines denote cumulative number for all events and events with magnitude larger than M_c, respectively. b) A zoom-in plot showing the detections 50 hours before and 100 hours after the Sumatra mainshock. c) Detection results around the 2005 Nias event near Zhongba. Symbols and notations are the same as in (a). d) A zoom-in plotting showing 50 hours before and 100 hours after the Nias event.

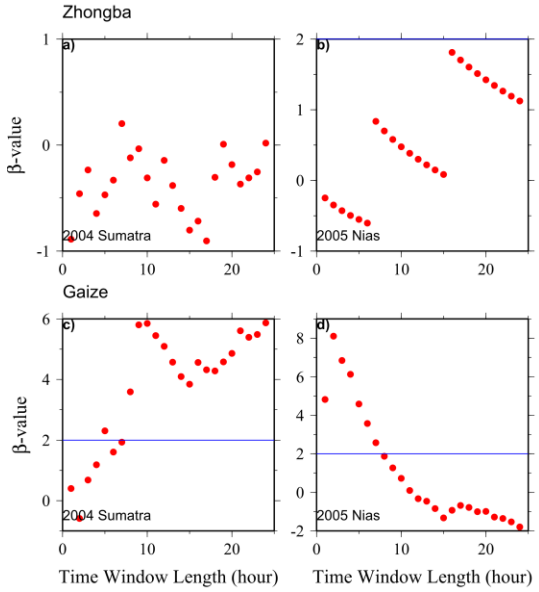

Figure 2.6 β-value for varying window length of 1-24 hours with 1-hour increment. Top two panels show results near Zhongba, and bottom two show results near Gaize. The longest

pre-mainshock window is used for calculating background seismicity rate (250 hours before Sumatra and 180 hours before Nias). Blue horizontal line shows 95% confidence level.

2.4.2 *Detection result near Gaize*

In comparison, many microearthquakes occurred during and immediately after the passage of the teleseismic surface waves of both mainshocks near Gaize (Figure 2.2 and Figure 2.7). The largest triggered earthquakes have local magnitudes of 3.64 and 3.80, respectively, and both were instantaneously triggered during the large-amplitude surface waves. Near Gaize, we used 547 templates for detection around the 2004 Sumatra and 2005 Nias events. As a result, 1350 and 2500 events are detected 10 days before and 15 days after the two mainshocks, respectively. The M_c is –0.6 and –0.4 for the Sumatra and Nias cases (Figure 2.4), respectively. Clear increases of microearthquakes are found following both mainshocks (Figure 2.8b and Figure 2.8d). The seismicity rate increase was steady immediately following surface waves of the Sumatra mainshock and lasted nearly 2 days. The seismicity rate suddenly dropped below the pre-mainshock level afterwards (Figure 2.8b). In comparison, the increase following the Nias mainshock was dominated by two bursts, one right after the surface waves and another one ~2 hours later. We also computed the β-values, and the results suggest significant seismicity rate increase in most time windows after both events (Figure 2.6). We noted clear differences in the β-value results between the 2004 Sumatra and 2005 Nias events. The β-value generally increased with time following the Sumatra event, but decreased following the Nias event. In addition, we performed a sliding-window β-value analysis in a much longer time window [*Meng and Peng*, 2014] (Figure 2.9). In both cases, we found a

moderate seismicity rate decrease following a significant seismicity rate increase for the Sumatra and Nias events.

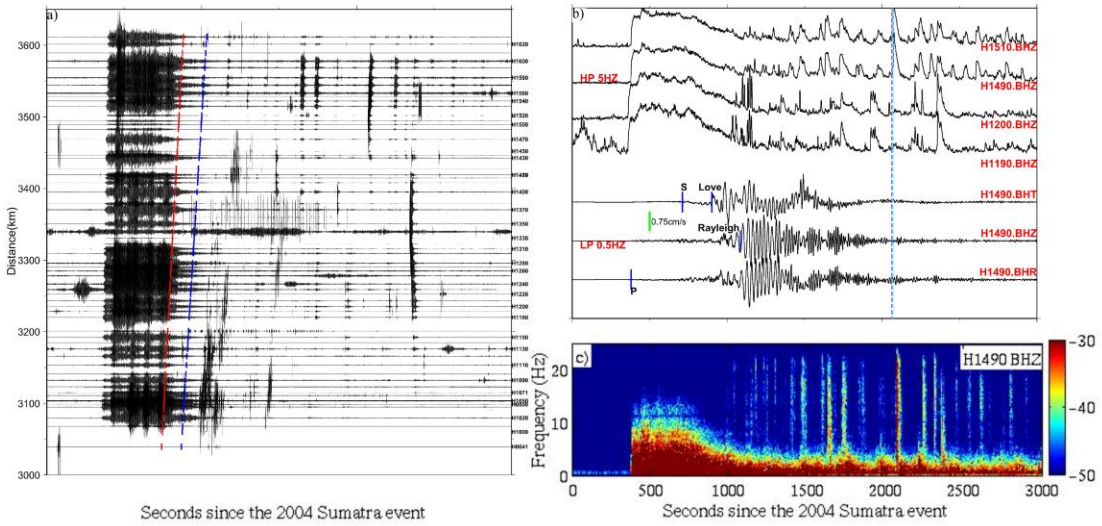

Figure 2.7 a) 5-Hz high-passed vertical-component waveforms aligned with epicentral distances during the 2004 M_w 9.1 Sumatra mainshock. The dashed red and blue lines mark the predicted Love and Rayleigh wave arrival (with a nominal phase velocity of 4.1 and 3.5 km/s). b) Log10 envelope function of 5-Hz high-passed seismograms at stations near Gaize (H1490 and H1510) and Zhongba (H1190 and H1200). The bottom three traces are broadband recordings rotating to transverse, vertical and radial components. *P*, *S*, Love and Rayleigh phases are marked. Blue vertical dashed lines are detected events and cyan lines are templates used for detection. c) Spectrogram of vertical component recorded at station H1490.

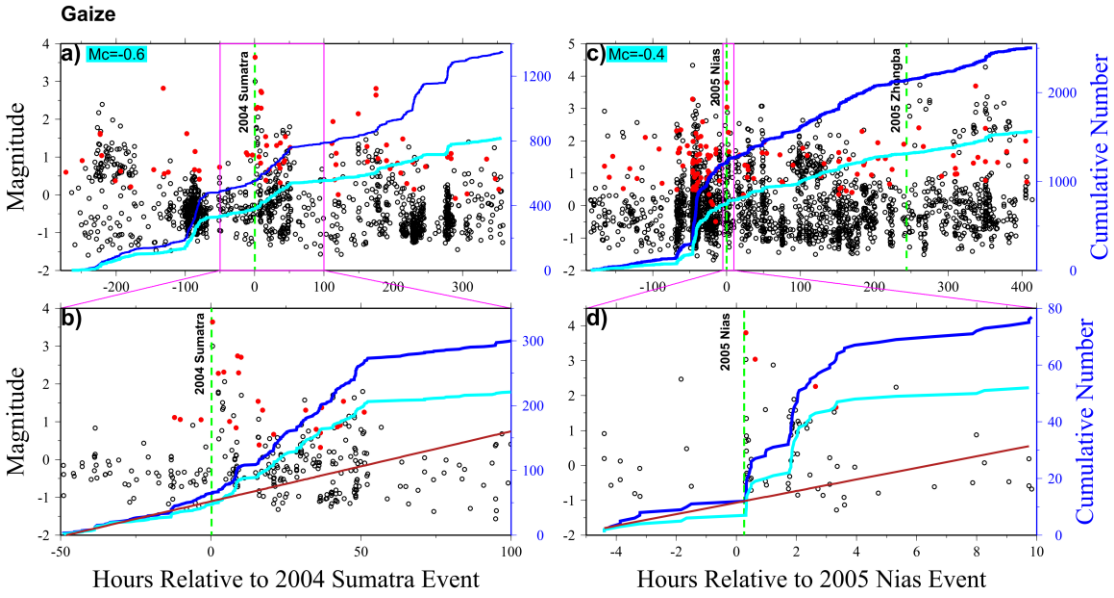

Figure 2.8 Detection results near Gaize. All symbols and notations are the same as in Figure 2.5.

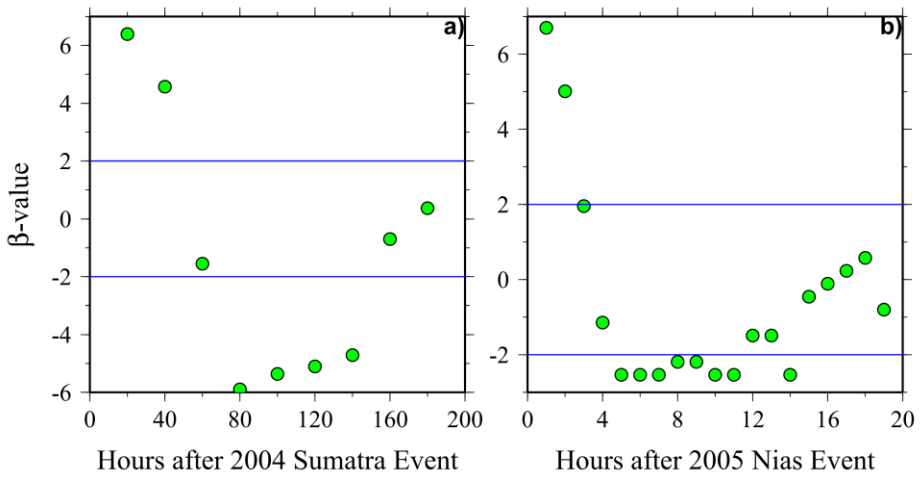

Figure 2.9 Sliding window β analysis after the 2004 Sumatra (a) and 2005 Nias events (b). A 40-hour window is used for Sumatra case and 2-hr window for Nias. The longest pre-mainshock time window is used for computing background seismicity rate (same with Figure 2.6). Two horizontal lines mark value of 2 and -2.

2.5 Discussion

In this study, we documented, to the best of our knowledge, the first observation of dynamically triggered seismicity within Tibet Plateau. Events triggered by the 2005 Nias earthquake mainly occurred near Gaize in the Qiangtang terrain. On the other hand, the 2004 Sumatra earthquake triggered earthquakes at other places outside of the Gaize region. In addition, the temporal increase of seismicity lasted for at least 2 days and a few hours for the Sumatra and Nias mainshocks, respectively. Both temporal increases of seismicity rate were followed by a moderate rate decrease (Figure 2.9). This type of rate reduction following a significant rate increase is similar to recent observations of triggered tremor in southern Taiwan following the 2011 M_w 9.1 Tohoku-Oki earthquake [*Sun et al.*, 2015], and a global quiescence of M>5.5 earthquake after a transient increase

following the 2012 M_w 8.6 Indian Ocean earthquake [*Pollitz et al.*, 2014]. In these cases, the reduction can be best explained as a 'dynamic shadow effect', where most fault patches close to failure are triggered by a large teleseismic earthquake, resulting in a period of seismic quiescence.

The seismicity triggered by the Sumatra mainshock did not follow the Omori-law type decay [e.g., *Brodsky*, 2006]. Instead it showed a steady rate increase for ~50 hours, and then a sharp rate reduction (Figure 2.8b). A similar pattern of triggered deep tremor was identified along the central San Andreas Fault and was explained as secondary triggering by aseismic fault slip [*Shelly et al.*, 2011]. On the other hand, the M~4 event triggered near Gaize by the Nias event was followed by an Omori-like aftershock sequence (Figure 2.8d). Another similar Omori-like sequence occurred ~2 hours after the Nias event, but no clear mainshock was identified. The different behaviors near Gaize following the Sumatra and Nias events could be attributed to the fact that most of triggered earthquakes during the Nias surface waves are clustered, while the Sumatra mainshock triggered events on different sites. The mean peak ground velocities (PGVs) across all stations are 0.93 ± 0.25 cm/s and 0.26 ± 0.04 cm/s during the Sumatra and Nias mainshocks, respectively. These PGVs correspond to a factor of 4 differences in dynamic stresses (93 and 25 kPa), assuming a nominal phase velocity of 3.5 km/s and crustal rigidity of 35 GPa [*Aiken and Peng*, 2014]. In comparison, the cumulative energy density [*Brodsky and Prejean*, 2005] for the Sumatra mainshock is about 15 times more than that for the Nias mainshock (Figure 2.10), likely due to its long rupture duration [*Lay et al.*, 2005]. Hence, we suggested that long-duration surface waves of the 2004

Sumatra mainshock, together with its high PGVs, help to excite more regions in South-Central Tibet and last longer than during the Nias mainshock.

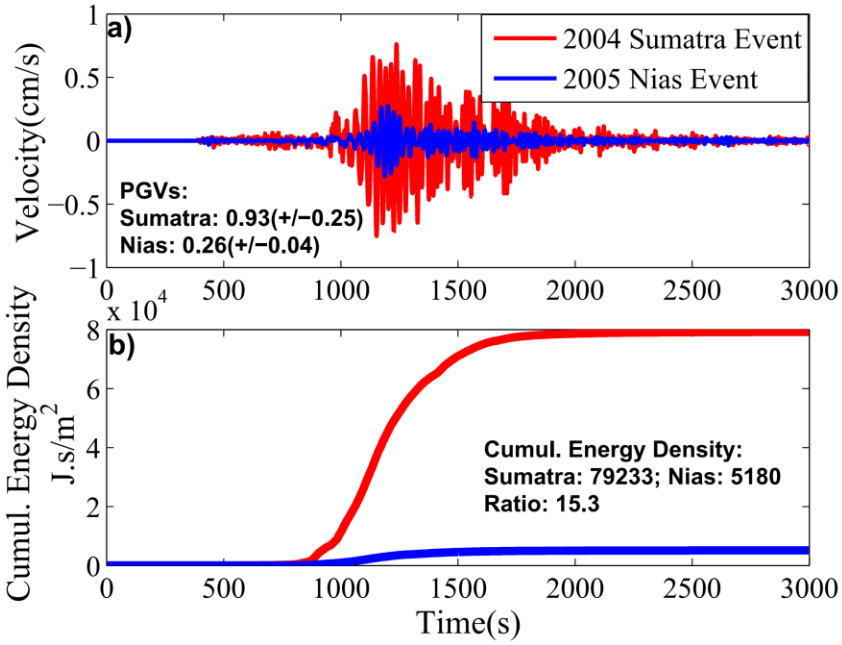

Figure 2.10 a) The velocity seismogram within 3000s after the 2004 Sumatra and 2005 Nias mainshocks recorded by station H1490. b) Average Cumulative Energy Density (ACED) within 3000s after the Sumatra and Nias mainshocks. The ACED of the Sumatra event is 15.3 times the Nias event in first 3000s and the source duration lasts for longer time around Sumatra event.

The *M*~6 Zhongba sequences are ~300 km away from the Gaize region. Unfortunately, neither the 2004 nor the 2008 event was recorded by the HiCLIMB network. The predicted dynamic stress from the 2005 event is ~75 kPa. However, we did not observe clear seismicity rate change near Gaize around the 2005 Zhongba event (Figure 2.8c). One possible reason could be due to the 'dynamic shadow effect' after the 2005 Nias mainshock. The critically stressed patches near Gaize ruptured when the surface waves of the 2005 Nias earthquake passed by and were not ready when the 2005 Zhongba event occurred. Alternatively, triggering in this region could be frequency

dependent [e.g., *Brodsky and Prejean*, 2005], such that only long-period surface waves from very large and distant earthquakes are capable of triggering seismicity.

As mentioned before, a M_w 6.3 local event occurred in Zhongba ~10 days after the 2005 M_w 8.6 Nias earthquake, suggesting a possible triggering relationship [*Ryder and Bürgmann*, 2011]. However, our detection results did not show any clear increase in seismicity rate following the Nias event that could support this hypothesis (Figure 2.5). We noticed that the M_c for the detected catalogs near Zhongba (1.1 to 1.7) is about one magnitude larger than near Gaize (–0.6 to –0.4), mainly due to the differences in epicentral distances. Hence, it is possible that smaller-magnitude events (e.g., < 1) may be triggered near Zhongba during the Nias earthquake, but were not detected by our NWMFT. Another possibility is that the Nias earthquake mainly triggered aseismic slip in the Zhongba region, which could not be detected by the seismic method. In any case, while we could not completely rule out a causal relationship between the M_w 8.6 Nias and M_w 6.3 Zhongba earthquakes, we did not find any clear change in local seismic activity that can be used to link these two events [e.g., *Anderson et al.*, 1994; *Papadopoulos*, 2002; *van der Elst et al.*, 2013].

The study region near Gaize is mainly characterized by northeastern trending left-lateral strike slip faults and northern-northwestern trending normal faults [*Kapp et al.*, 2005; *Ryder et al.*, 2010], which agrees with normal-faulting mechanisms of recent earthquakes (Figure 2.1) and is similar to the Zhongba region further south. This is consistent with current observations that dynamically triggered microearthquakes mostly occur in extensional or trans-extensional regions [*Hill and Prejean*, 2015]. However, it is still not clear why both mainshocks trigger near Gaize, but not near Zhongba, despite the

fact that the Zhongba region is slightly closer to the mainshocks and hence would receive higher dynamic stress perturbations. One major factor is that there was another M_w 6.2 (M_s 6.9) earthquake near Zhongba on 07/11/2004, while no major earthquakes occurred near Gaize in 2004-2005. Hence, it is possible that the 2004 Zhongba earthquake and its aftershocks released most of the accumulated tectonic stresses such that the region is no longer in a critical state [e.g., *Brodsky and van der Elst*, 2014]. However, this is inconsistent with the fact that another M_w 6.3 earthquake occurred in Zhongba 10 days after the Nias mainshock and previous observations that dynamic triggering preferentially occurs in aftershock regions of previous large earthquakes [*Hough et al.*, 2003; *Jiang et al.*, 2010].

We note that the Zhongba region has higher background seismicity rate than the Gaize region (i.e., larger *a* value in Figure 2.4), but most triggered activity was found in the Gaize region. This observation is also inconsistent with recent observations that regions with higher background rate (i.e., geothermal and/or aftershock regions of recent/historic large events) are more susceptible to dynamic triggering [*Hough et al.*, 2003; *Jiang et al.*, 2010; *Aiken and Peng*, 2014]. The heat flow map in this region shows a higher flux near Zhongba in the Lhasa Terrane (95-105 mW/m^2), as compared to 70-80 mW/m^2 near Gaize in the Qiangtang Terrane [*Tao and Shen*, 2008], which does not support the observation that geothermal/volcanic regions with high heat flows favor triggering of microearthquakes [*Hill and Prejean*, 2015; *Aiken and Peng*, 2014]. In addition, previous studies revealed that the Qiangtang Terrane has a thicker seismogenic zone than Lhasa Terrane [*Wei et al.*, 2010]. However, it is not clear how this would affect the triggering behavior. Further studies are needed to better understand the differences in

triggering behaviors in these regions. This will be a subject of future research. Nevertheless, our observations presented here, along with recent studies [e.g., *Hill and Prejean*, 2015], clearly demonstrate that large earthquakes are capable of dynamically triggering microearthquakes up to magnitude 4 in active continental-continental convergent regions.

CHAPTER 3. ISOLATED LOCATIONS OF DYNAMICALLY TRIGGERED EARTHQUAKES IN THE NORTH ISLAND OF NEW ZEALAND FOLLOWING THE 2016 M_W 7.8 KAIKOURA EARTHQUAKE

3.1 Introduction

The M_w 7.8 Kaikoura earthquake struck the South Island of New Zealand at 12:03 am local time on November 14th, 2016 (2016/11/13 11:02:56.35 UTC). The mainshock epicenter is located at a transition zone from the Hikurangi subduction zone to the Northeast to the transpressional Alpine fault to the Southwest (Figure 3.1). The earthquake ruptured multiple active faults with surface slip up to 10 m and terminated offshore near Cook Strait [*Hamling et al.*, 2017; *Kaiser et al.*, 2017]. The earthquake triggered several shallow slow slip events (SSE) in the North Island [*Wallace et al.*, 2017], and possible deep slip events [*Wallace et al.*, 2018]. The majority of slow slip occurred along the shallow portion of the Hikurangi subduction interface near Hawke's Bay (Figure 3.1). *Wallace et al*. [2017] suggested that the low-velocity sedimentary wedge likely acted as an amplifier, together with the rupture directivity, to promote dynamic triggering of shallow slow-slip events. *Peng et al*. [2018] reported triggered microearthquakes and tremor events in both islands following the Kaikoura event. Using earthquakes listed in the GeoNet catalog, they found several regions with clear evidence of dynamically triggered earthquakes in the North Island. However, they also mentioned that the observations could be incomplete due to potential bias from missing events following the mainshock. Our study is an extension of that work. Specifically, we obtain

a more complete catalog in the North Island around the mainshock using a waveform matched filter technique. We compare the seismicity rate change pattern with the dynamic stress change using two different kinematic source models [*Holden et al.*, 2017; *Wang et al.*, 2018], in order to better understand how different tectonic environments respond to the stress perturbation.

3.2 Study Region and Data

The oblique strike-slip Alpine fault connects the westward dipping Hikurangi subduction zone and eastward dipping Puysegeur subduction zone, forming the current tectonic framework around which convergence of the Australian and Pacific plates is accommodated in New Zealand (Figure 3.1). In the North Island, the Pacific plate subducts obliquely beneath the Australian plate along the Hikurangi margin with a slip rate of 39-48 mm/yr [*Beavan et al.*, 2016]. This convergence drives back-arc rifting and volcanism in the Taupo Volcanic Zone (TVZ), which has been active for the past two million years, including recent eruptions of Mt. Ruapehu [e.g., *Jolly et al.*, 2010] and the Tongariro volcano [e.g., *Hurst et al.*, 2014]. Earthquake swarms and volcanic tremor occur frequently in these regions, and are actively monitored by GeoNet seismic stations. Near the southern end of the North Island, westward plate convergence is partitioned into trench-normal motion on the subduction zone and trench-parallel motion in upper plate strike-slip faults [*Nicol and Beavan*, 2003], while the forearc rotates with increasing subduction rate farther to the north near the Havre Trough [*Wallace et al.*, 2004]. Hence, background seismicity in the North Island is typically associated with the Hikurangi subduction zone, magma movements along the TVZ, or tectonic movements in the upper crustal faults.

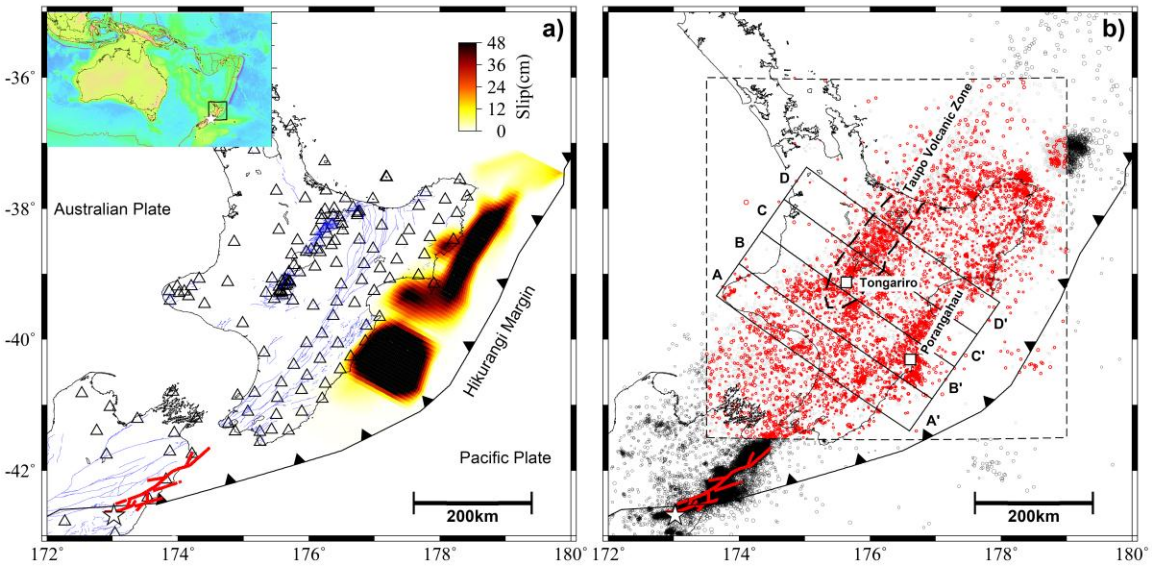

Figure 3.1 Map of the study region. a) Solid blue curves show mapped faults. Open triangles are seismic stations. Slip distribution during the triggered shallow SSE is adopted from *Wallace et al.* [2017]. Left top insert shows the study region in a bigger context. b) Events from GeoNet before and after the Kaikoura mainshock (white star) are shown with gray and red circles within dashed box (North Island), respectively. Black circles are catalog events outside dashed box since 2016. Cross-sections AA', BB', CC' and DD' are plotted in Figure 3.2. Regions highlighted include the Taupo Volcanic Zone (TVZ), Mt. Tongariro, as well as Porangahau coast.

3.3 Data and Method

We select earthquakes listed in the GeoNet catalog as possible template events (Figure 3.1b) and use a cross-correlation procedure to search for events with similar waveforms in archived continuous waveforms to obtain a more complete catalog in the North Island following the mainshock. Figure 3.2 shows four cross-sections of the interface geometry for the Hikurangi subduction zone [*Williams et al.*, 2013], together with seismicity listed in the GeoNet catalog from 03/30/2016 to 03/16/2017. Events after the Kaikoura mainshock are color-coded by the elapsed time since the mainshock, highlighting regions with potential seismicity rate increases following the mainshock [*Peng et al.*, 2018].

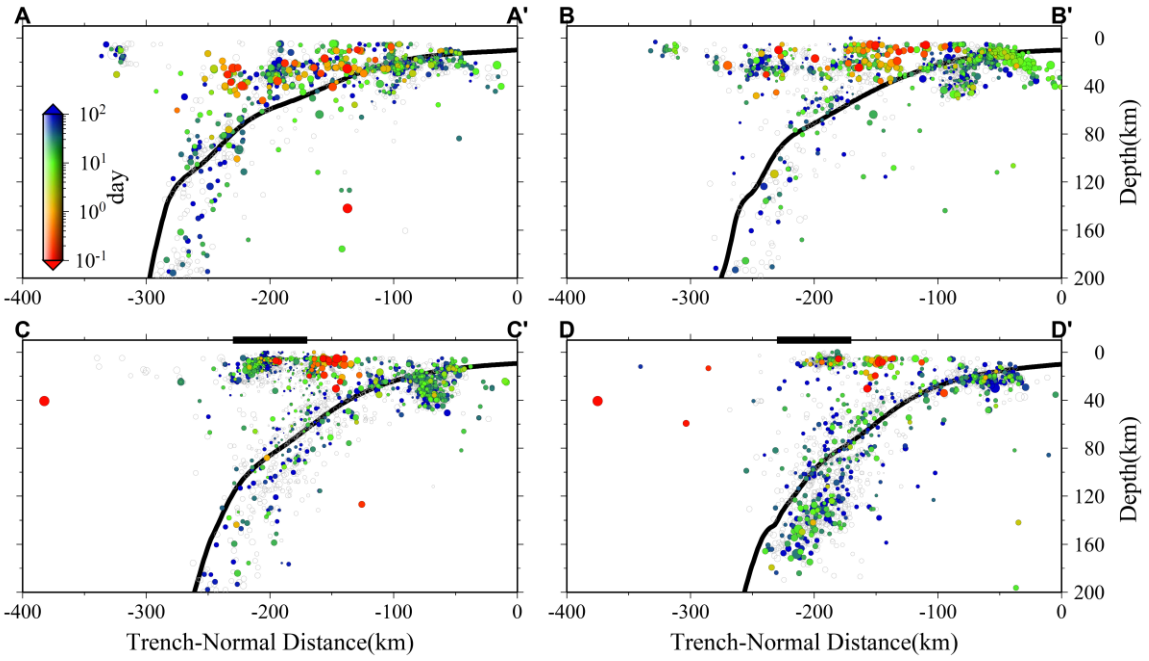

Figure 3.2 Depth profiles along the marked cross-sections in Figure 3.1. Events after the Kaikoura mainshock are color-coded with the elapsed time. Open gray circles are earthquakes before the mainshock. Bold black curves show the Pacific plate geometry from *Williams et al*. [2013]. The horizontal bars along section CC' and DD' outline the TVZ.

Continuous waveforms (both HH and EH components) are requested via the CWB client from GeoNet (https://www.geonet.org.nz/data/tools/CWB). We apply a 2-8 Hz band-pass filter on the continuous data to suppress possible contaminations from distant sources and increase the relative signal of local earthquakes. To reduce computational cost, we down-sample the original waveform (100Hz for HH and 100Hz or 200Hz for EH) to 20Hz. Waveforms of template events are cut from filtered and down-sampled continuous data, and phase picks provided by GeoNet are saved. To avoid noisy traces, we define a minimum acceptable signal to noise ratio (SNR) for each trace as a ratio between the cumulative energy of the signal window (the same window used for detection: a 20s window starting 1s before the P arrival) and noise window (a 20s window ending 1s before the P arrival). Only traces with SNR above 5 are used in subsequent analysis, and events with at least 12 saved traces are further used as templates.

To suppress contamination of long-period energy from the mainshock and aftershock zone, a filter containing higher frequencies would be better suited for separating locally triggered events and distant aftershocks (Figure 3.3). Hence, we conduct another detection on a relatively smaller dataset to capture those local events using only nearby stations. Specifically, we apply a 10-30 Hz band-pass filter to the continuous waveform, and choose stations with epicentral distance less than 150km relative to the selected events. We also narrow down the catalog window starting from 11/01/2016 to 11/30/2016, and manually examine the phase arrivals for ~1,950 selected template events to remove both mislocated events (Figure 3.4) and events without robust phase picks. Eventually only ~1,210 events containing at least 9 channels with SNR above 5 are used as templates. In addition, a shorter 15s window (1s before and 14s after the P arrival) is used for detection.

Next, we perform template-matching detection using two sets of template events. The first (primary) detection includes ~17,000 templates (from 03/30/2016 to 03/16/2017) cross-correlating with 30 days' continuous waveform (from 11/01/2016 to 11/30/2016). Each template contains an average number of ~60 traces. The cross-correlation window is 20s long, and the sampling rate is 20 sample/s. The second (refined) detection utilizes ~1,210 templates to scan through the same month's continuous data, with ~20 traces on average for each template. The cross-correlation window is 15s with a sampling rate of 100 sample/s. Due to the heavy computational requirement, we utilize the XSEDE GPU cluster resource [*Towns et al.*, 2014], which can achieve ten to hundred times faster computation when comparing to CPUs [*Meng et al.*, 2012].

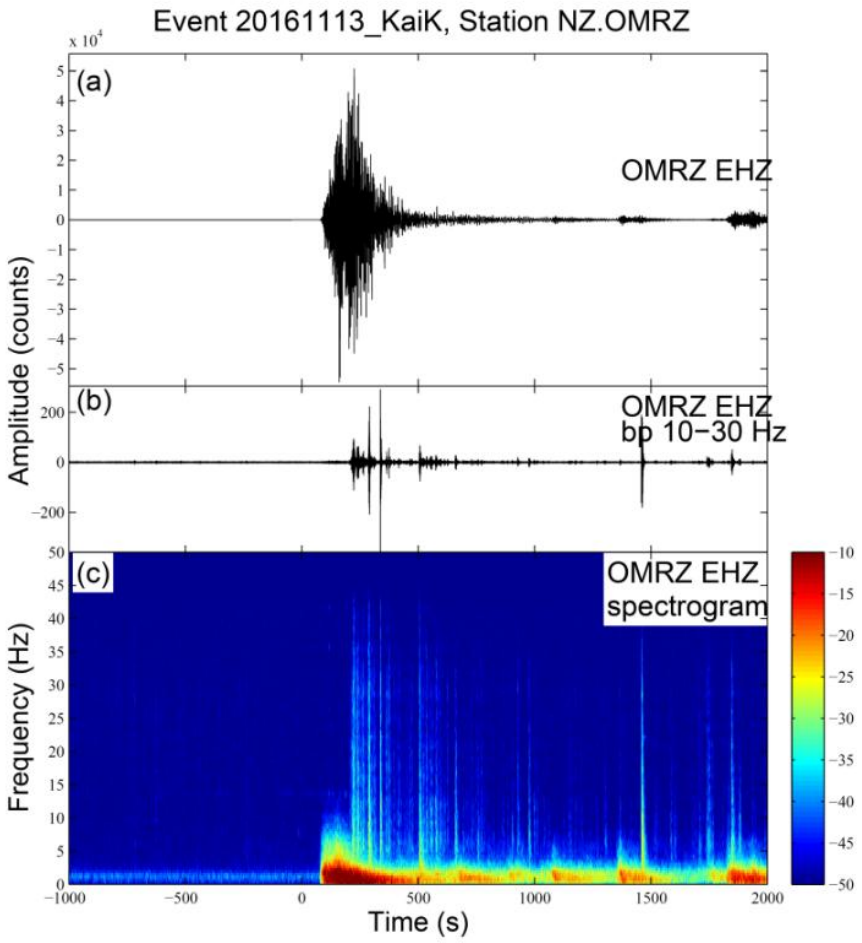

Figure 3.3 An example showing triggered earthquakes. a) Raw waveform recorded by station OMRZ.EHZ. b) Filtered waveform using a 10-30 Hz band-pass filter. c) Spectrogram.

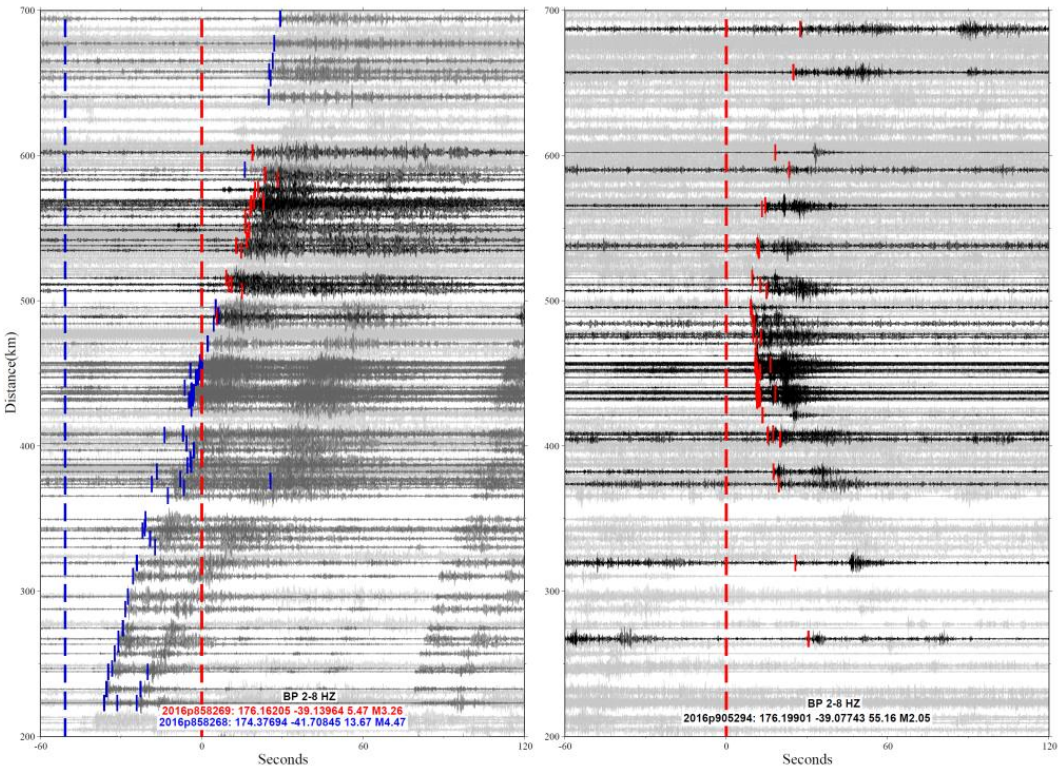

Figure 3.4 An example showing one wrongly located event (left) and its "nearby" reliable events (right). The wrongly located event utilized part of the phase picks (red vertical bars) of an event from aftershock region (with origin time and phase picks marked with blue vertical dashed line and blue vertical bars) and resolved a badly constrained locations.

For each template trace, we use the above defined signal window to run a sliding window cross-correlation (CC) with the corresponding continuous trace and obtain a single CC function. After shifting back to the template's origin time based on the arrival time, all CC functions of a common template are stacked together to generate a mean daily trace. We register a positive detection when the mean stacked CC value is above a pre-defined threshold. This is generally defined as the median CC of the stacked daily trace plus certain times of its Median Absolute Deviation (MAD) [*Shelly et al.*, 2007]. The magnitudes of newly detected events are computed based on the median peak amplitude ratios relative to best-matching templates [*Peng and Zhao*, 2009]. Since only nearby events can be matched with high CC values and we focus on the overall patterns

of seismicity rate changes, assigning the location of best-matching template to detected event meets the scope of our current study.

3.4 Results

3.4.1 *Event detection results*

The primary detection with ~17,400 events as templates and a 2-8 Hz filter resulted in ~19,000 additional events within the one-month study period above the 15 times MAD threshold, comparing to only 1,950 events in the catalog during the one-month period. The Gutenberg-Richter (GR) curves for the GeoNet and detected catalog is plotted in Figure 3.5, and the corresponding magnitudes of completeness (M_c) from best-combined method [*Wiemer*, 2001] are 2.7 and 2.3, respectively. We note that there's a "kink" in the GR curve at M3.0-5.0, where the observed number of earthquakes is larger than the predicted value. This turns out to be caused by the inclusion of mismatched relatively larger-magnitude events from the aftershock zone, which is explained further in section 3.5.2.

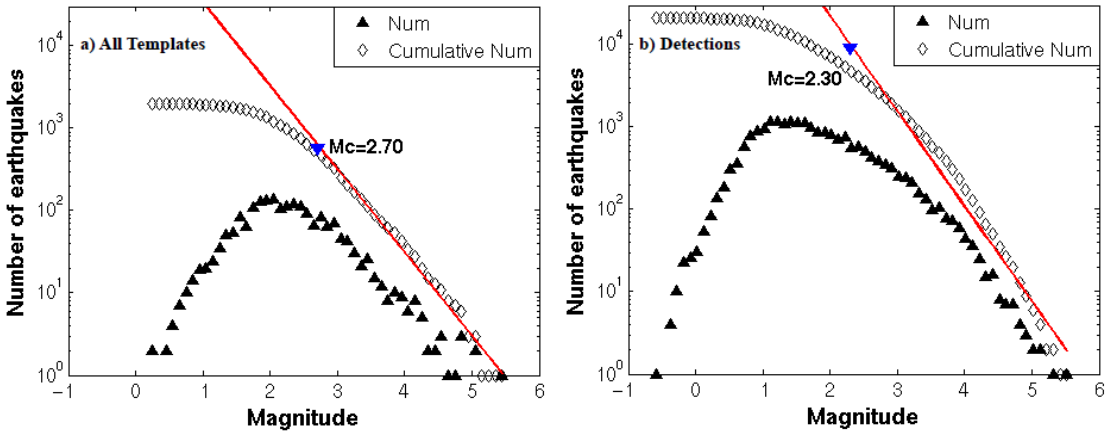

Figure 3.5 Gutenberg-Richter relationship for earthquakes from the whole catalog (~1,950 events from 011/01/2016-12/01/2016, M_c=2.70) and newly detected catalog (20,900 events using 15 MAD as the cutoff threshold, M_c=2.30).

In comparison, using ~1,210 manually picked selected catalog events within November 2016 (refined detection), ~9,300 additional events are found within the same continuous window using a threshold of 18 times MAD. Since we require a lower minimum number of traces (minimum 9 traces) and use a relatively shorter window, a slightly higher threshold is applied. The corresponding GR plots are shown in Figure 3.6. Although the M_c values are 2.3 for both template and detected catalogs, the cumulative number of events above the M_c values for both template and detected catalogs are 492 and ~2,100, respectively.

We highlight the primary detection results within regions surrounding the TVZ (Figure 3.7b, c & d), immediate to the south of Tongariro volcano (Figure 3.7e) and near the Porangahau coast (Figure 3.7f). These regions have experienced moderate to significant seismicity rate increases following the mainshock, as revealed by our recent analysis with the GeoNet catalog [*Peng et al.*, 2018]. To avoid potential bias of using a simple threshold, we plot events and cumulative numbers with both 12MAD and 15

MAD thresholds and catalog events. As shown in Figure 3.7, regions d and e show a clear increase of microseismicity immediately following the mainshock. In comparison, regions b and c further north only show a moderate co-seismic increase. The seismicity in region f near the Porangahau coast starts to increase only after one week following the mainshock.

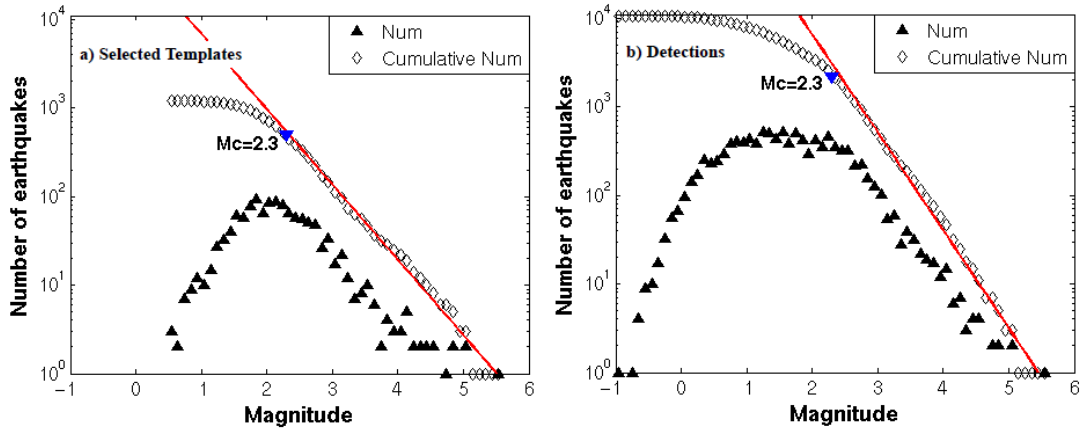

Figure 3.6 Gutenberg-Richter relationship for earthquakes from the selected catalog (1,210 events from 11/01/2016-12/01/2016, M_c=2.30) and associated detected catalog (10,500 events using 18 MAD as the cutoff threshold, M_c=2.30).

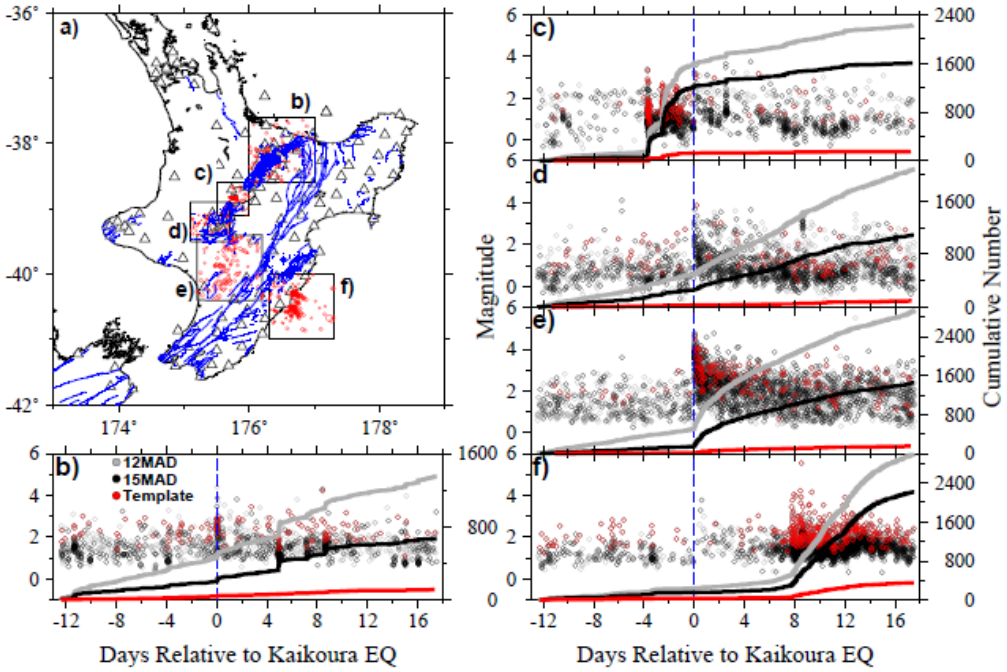

Figure 3.7 Primary detection result within highlighted regions: b), c) and d) are around the TVZ, e) south to the Mt. Tongariro, f) Porangahau coast. Solid blue curves show mapped faults. Detected events above 12MAD and 15MAD are shown with gray and black circles, while template events are marked with red circles. The corresponding cumulative number of earthquakes are plotted with solid line of same color.

Figure 3.8 shows the similar figure for the refined detection results. While the overall patterns are similar in certain regions to those shown in Figure 3.7, we identify several differences. First, the subtle co-seismic increase in regions b and c for the primary detection (Figure 3.7b&c) becomes more obvious for the refined detection (Figure 3.8b&c). In comparison, except a minor co-seismic increase in region d, the obvious increase in regions d and e during and following the mainshock almost completely disappear for the refine detection. The only region that does not show clear change is region f near the Porangahau coast, where a delayed slow-slip event has been triggered by the Kaikoura mainshock [*Wallace et al.*, 2017; *Peng et al.*, 2018].

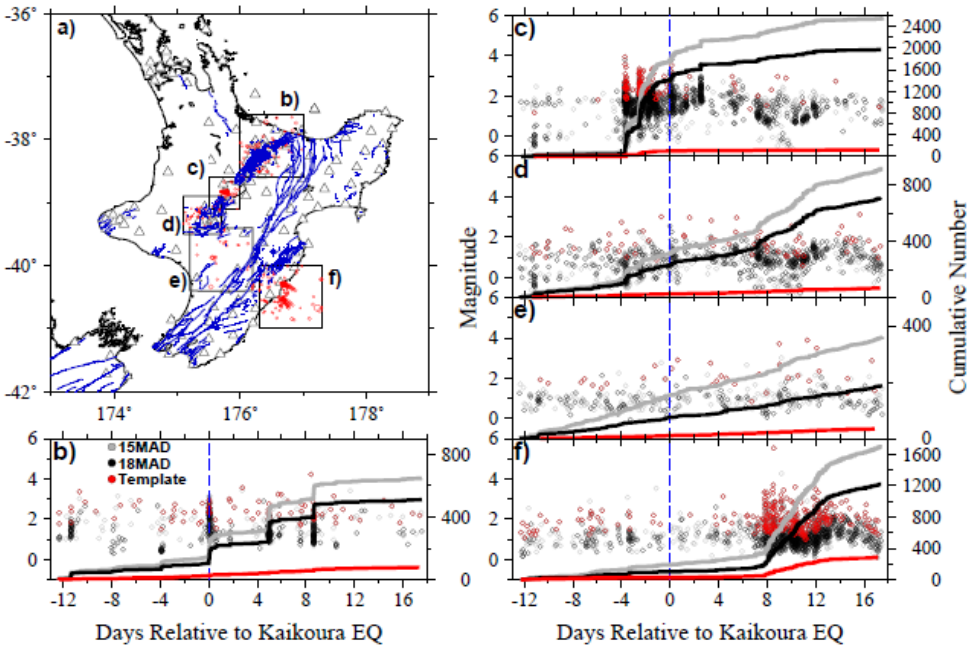

Figure 3.8 Refined detection result within highlighted regions; b), c) and d) are around the TVZ, e) south to the Tongariro volcano, f) Porangahau coast. Symbols and color scheme are the same as described in Figure 3.7.

3.4.2 *Seismicity rate change*

To further quantify seismicity rate change for both detected catalogs, we measure the β value map using different triggered windows in order to capture both instantaneous/short-term and delayed/long-term triggering effects: the first one is within 1 day following the mainshock, and the other one is to the end of detection window (17.5 days). The β map of the above two triggered windows for the primary detection is shown in Figure 3.9: a) and c) are results for GeoNet catalog events (with magnitude above M_c=2.70), while b) and d) are corresponding panels for the newly detected catalog (with M_c=2.30). Figure 3.10 shows similar plots for the refined template and detected catalogs (both with M_c=2.30). In both cases, the detected catalog shows more obvious change of seismicity within the TVZ in the short-term window, and around the Porangahau coast in the long-term window. When comparing with Figure 3.9 and Figure 3.10, the largest

change occurs to the east and southeast of TVZ. The clear increase of seismicity rate for the primary detection completely disappears for the refined detection. This is consistent with the observation in Figure 3.7 and Figure 3.8 for the region e. We will discuss this further in section 3.5.

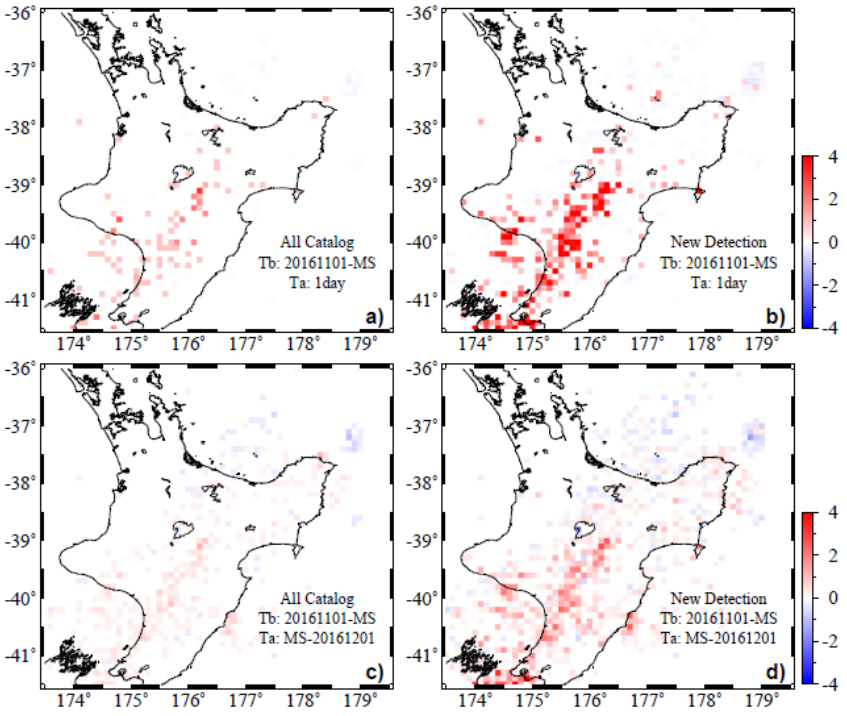

Figure 3.9 Beta map for the template and detected catalog of the primary detection. a) and b): short-term change using 1day after the mainshock as the "triggered window". c) and d): long-term change using mainshock to the end of Nov (~17.5 days) as the "triggered window".

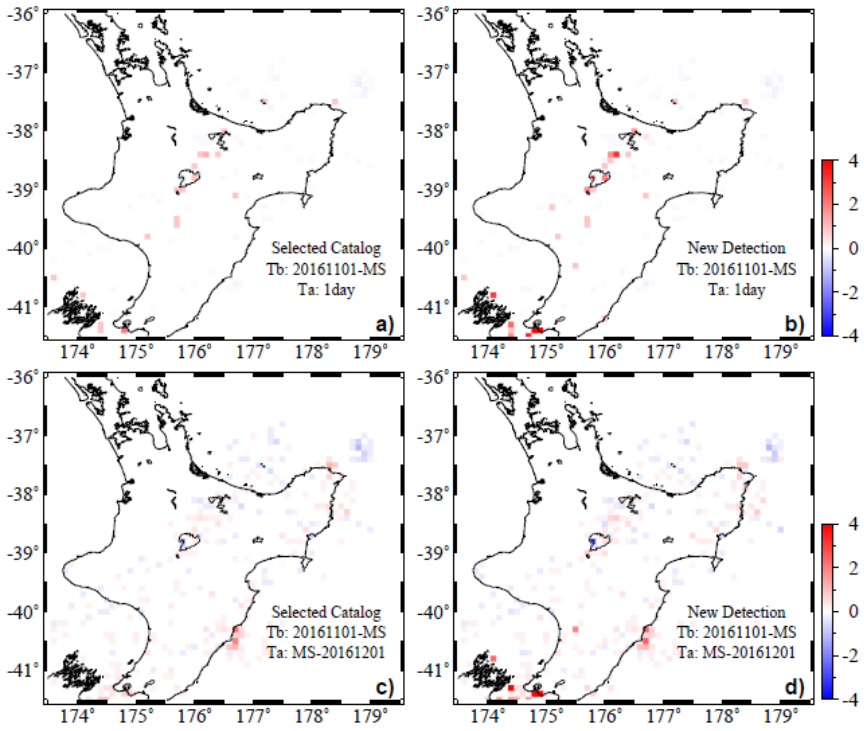

Figure 3.10 Beta map for the template and detected catalog of the refined detection. a) and b): short-term change using 1day after the mainshock as the "triggered window". c) and d): long-term change using mainshock to the end of Nov (~17.5 days) as the "triggered window".

3.4.3 *Comparisons with dynamic stress*

Next we compute daily seismicity rate during aforementioned two triggered windows at different depth ranges (Figure 3.11a & d). Considering large depth uncertainty, we use a depth range of 0-10 km for instantaneously triggered shallow events within TVZ, and 10-20 km for delayed triggered earthquake cluster for the subduction zone near the Porangahau coast (Figure 3.2). We then use the same method as described in *Wallace et al*. [2017] to compute dynamic stress changes in the period range of 3 and 100 seconds. Since it's still under debate whether the mainshock ruptured the megathrust offshore, we use both the updated kinematic source model in *Holden et al*. [2017] (*Holden's Model*, Model A that fits well both local strong-motion and geodetic data) and *Wang et al*. [2018] (*Wang's Model*, which includes ~45% of the total moment release

from the Hikurangi subduction interface). At each point in the crust, stress tensor time-series are computed and converted into the time-series of the square root of the second invariant of the deviatoric stress tensor, sqrt(J_2).

Following *Brenguier et al*. [2014], we define dynamic stress "susceptibility" as the ratio between the observed daily seismicity rate and the maximum amplitude of estimated dynamic stress changes, max(sqrt(J_2)). We report dynamic stress susceptibility at depth slices of 5 km and 15 km, representing seismicity around the shallow crust in the TVZ and Hikurangi subduction interface, respectively. The corresponding "susceptibility" maps using dynamic stress change based on Holden's Model for the primary detection with both short and long-term windows are shown in Figure 3.11c and Figure 3.11f (results based on Wang's Model can be found in Figure 3.12). As expected, for the short-term window, regions around and to the south and east of the TVZ are highlighted. For the long-term window, regions along the east coast, and isolated regions around the TVZ are highlighted. Figure 3.13 and Figure 3.14 show similar plots using above models for the refined detection. The primary difference is that for the short-term window, the primary highlighted region is within the TVZ. For the long-term window, the primary highlighted region is along the coast of North Island.

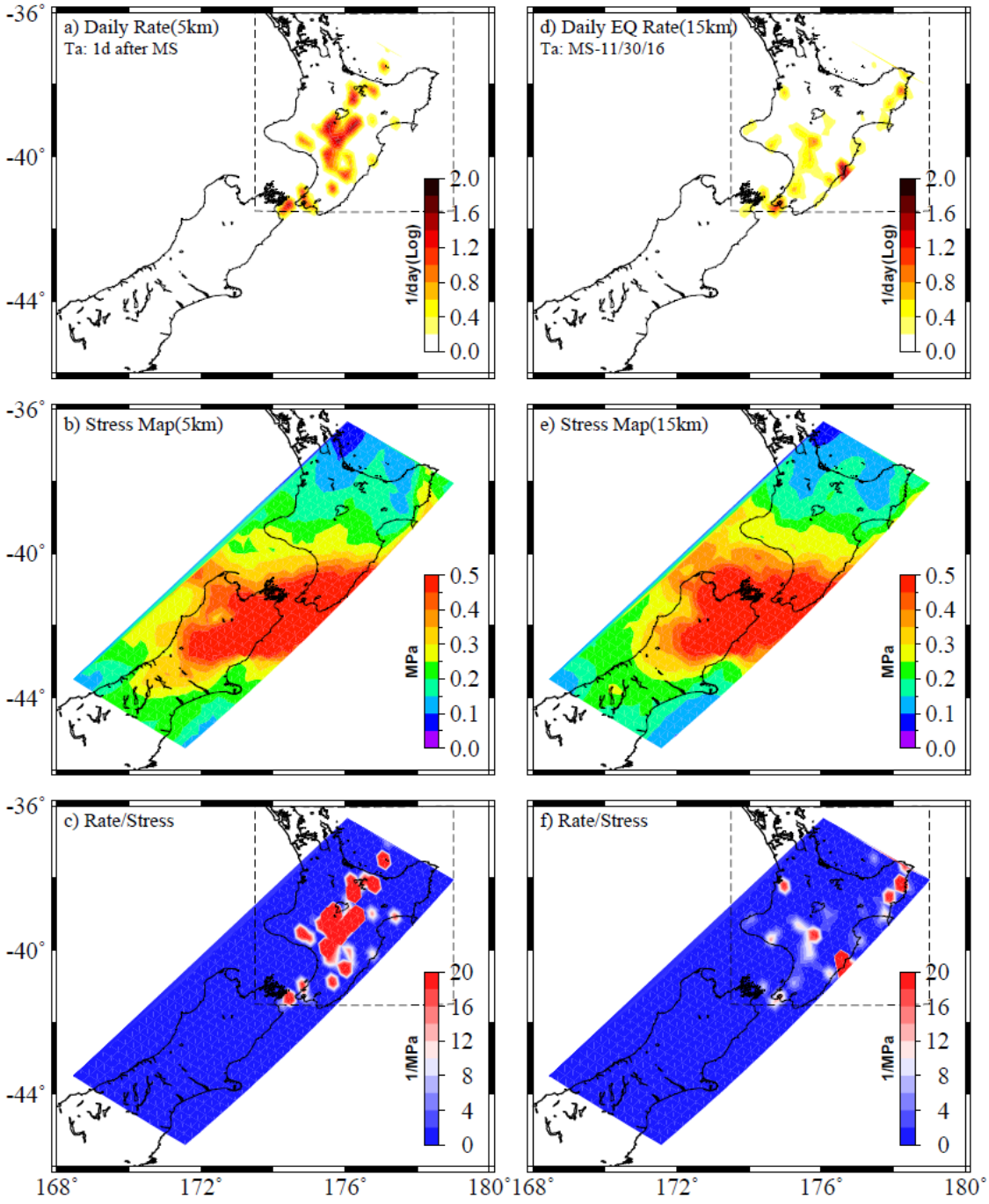

Figure 3.11 Comparison between the daily seismicity rate and calculated dynamic stress for the primary detection. a) and d) show the daily seismicity rate in short "triggered window" at shallow depth (0-10km) range, and long "triggered window" within depth range of 10-20km. b) and e) are estimated dynamic stress changes, max(sqrt(J_2)), at points in crust at similar depths. c) and f) indicate the defined dynamic stress "susceptibility".

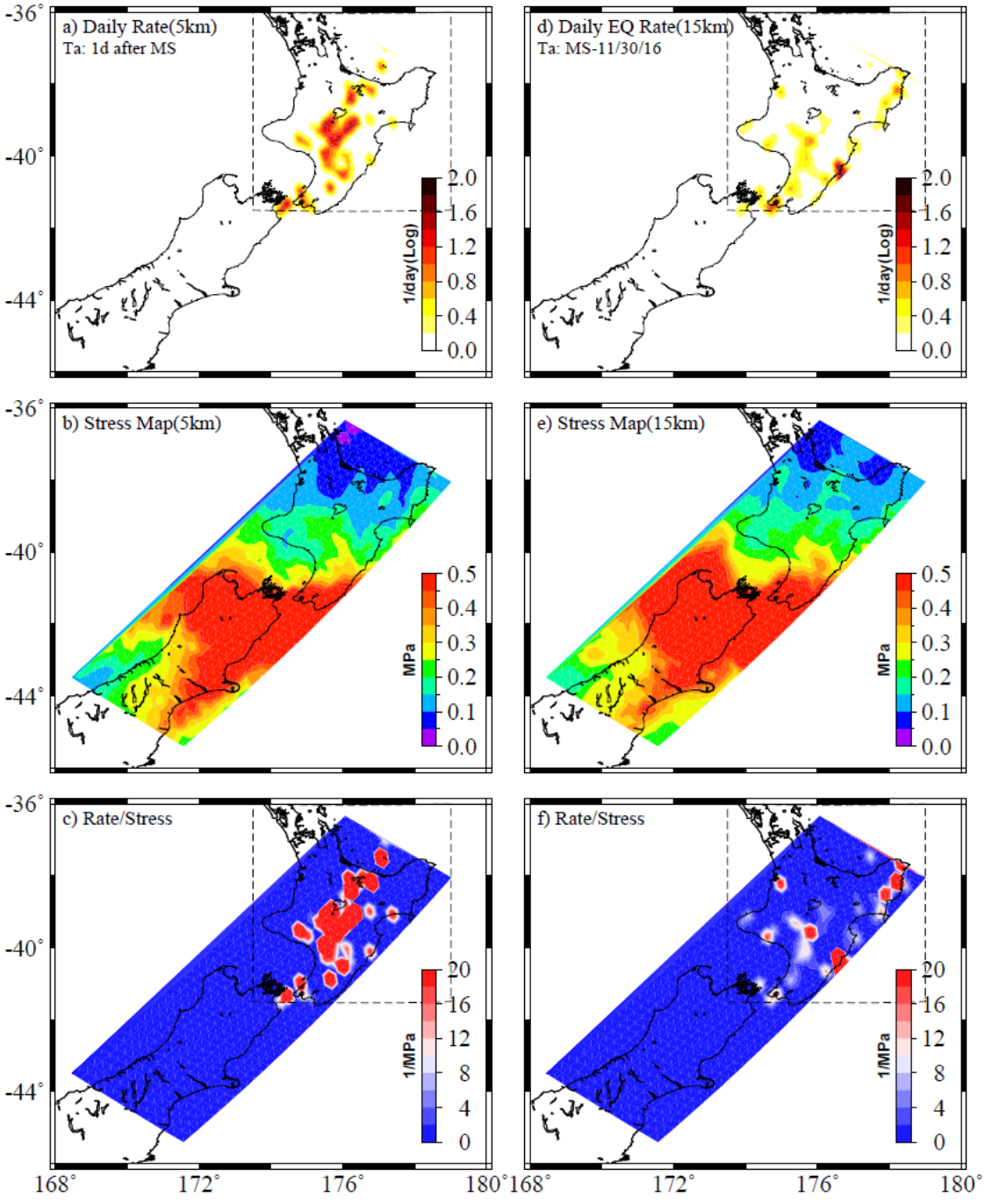

Figure 3.12 Comparison between the daily seismicity rate and calculated dynamic stress for the primary detection, similar to Figure 3.11. Dynamic stress changes and dynamic stress susceptibility using the Kaikoura earthquake source model of *Wang et al.* [2018], which includes large moment release (~45% of the total) from the Hikurangi subduction interface.

3.5 Discussion

In this study we have performed systematic event detections in North Island following the 2016 M_w 7.8 Kaikoura earthquake, and find clear evidence of triggered earthquakes within the North Island at multiple spatial-temporal windows. Because the waveform matching technique strongly depends on the reliability of the template catalog, the inclusions of mislocated template could introduce additional false detection, resulting in possible erroneous interpretation. In this section, we first examine the robustness of increasing seismicity within the TVZ and Porangahau coast, then discuss a possible biased observation to the immediate south of TVZ due to the "ghost" catalog events.

3.5.1 *Comparison between different filters*

First we examine the 10-30 Hz band-pass filtered waveform for stations within TVZ to demonstrate that our technique can help recover small events after the mainshock. As shown in Figure 3.15, many missing events in the first 1000s were detected by our method. In comparison, only 2 events were listed in the GeoNet catalog. However, there are still some obvious events not detected by the template matching method. It is possible that some earlier triggered events are tremors with longer duration and no clear phase arrivals [*Peng et al.*, 2018], and hence cannot be matched by earthquake templates. In addition, some missing earthquakes could occur on asperities that didn't ruptured long before or after the mainshock, so no template could match them.

Figure 3.16 shows the comparison between the detection results at regions within TVZ using 2-8 Hz and 10-30 Hz bandpass filters. As mentioned before, the higher frequency band helps to suppress most energy from the mainshock and its aftershocks and results in cleaner seismicity pattern (Figure 3.16b, d & f). On the other hand, more

templates and lower frequency band may obscure the pattern (Figure 3.16a, c & e), especially if some template events were mislocated (e.g., Figure 3.4). Similar result is also found around the Porangahau coast. Hence, while the above comparison demonstrates that observations of elevated seismicity within TVZ and Porangahau coast are robust, additional screening is needed to ensure that the template events are robust.

3.5.2 *Bias from "ghost" template events*

A suspicious region is immediate to the southeast of TVZ (Figure 3.7e): seismicity in the upper crust clearly increased after the mainshock (cross-section BB' and CC' in Figure 3.2). On the other hand, this region is away from any mapped active faults or volcanoes [*Peng et al.*, 2018]. We note that there are fewer close-by stations (Figure 3.1), which might result in poorly constrained event locations. By manually inspecting the waveforms, we find that many events along the extended band to the south of TVZ are either mislocated, or their phase arrivals are falsely picked. During the selection process with the second 10-30 Hz filter, most events within this region are dropped. The potential causes of those "ghost" templates include contaminated energy from the mainshock and aftershock zone at the lower frequency range (Figure 3.3), as well as badly constrained locations using only P phases or erroneously labeled phases. We note that phase picks of above dropped events are mostly P arrivals from an automatic Short-Term Average/Long-Term Average (STA/LTA) algorithm, while additional manually picked arrivals help resolve better locations for other kept catalog events.

We further demonstrate the above "ghost" event by showing waveforms for one mislocated event and its nearby reliable event (Figure 3.4). Event 2016p858269

(magnitude 3.26; origin time: 2016/11/13 13:26:15.765, ~8,600s after the Kaikoura mainshock) was assigned as an event to the south of Lake Taupo. We found that this event indeed shares part of the phase picks from event 2016p858268 (magnitude 4.47; origin time: 2016/11/13 13:25:24.948, ~50s earlier than 2016p858269), which is within the aftershock region. Clearly the location of event 2016p858268 is better constrained with more phase picks and better moveout (Figure 3.4), while only P arrival picks from several stations within TVZ resolve a likely erroneous location for event 2016p858269. Another indirect supporting evidence for the contamination from the aftershock zone is the "kink" observed in the GR curve of the detected catalog (Figure 3.5). Among 1,633 events with magnitude above 3.0, ~1,150 events (~70%) are associated with dropped events. We suggest that an "over-estimation" of *M*3-5 events is caused by erroneous association of some large events from the aftershock zone as local events. Moreover, the long-term monthly seismicity rate around this suspicious region shows a nearly consistent value (Figure 3.17), while the abnormally high rate following the mainshock is caused by the above "ghost" catalog events.

The inclusions of those "ghost" templates could result in a biased increase of local seismicity within the region to the south of TVZ, which was already evident in the GeoNet data alone [*Peng et al.*, 2018], and elevated further after template matching (Figure 3.7). By filtering out lower frequency energies and adjusting their phase picks and locations manually, we could remove the biased observation to some degree. However, these mislocated events can only be resolved by carefully examining the phase picks and relocating using updated velocity models, which requires additional analysts' efforts.

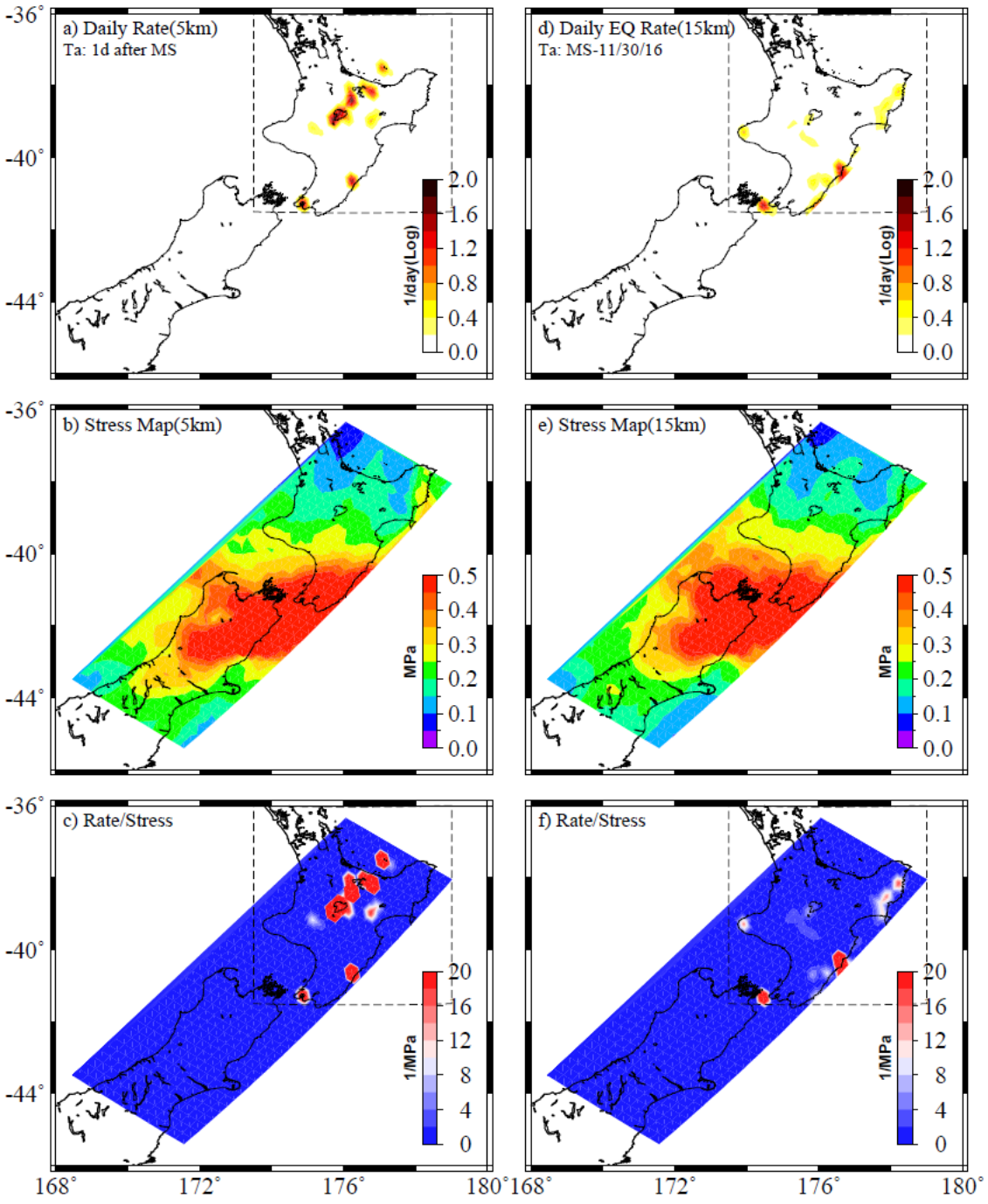

Figure 3.13 Comparison between the daily seismicity rate and calculated dynamic stress for the refined detection. a) and d) show the daily seismicity rate in short "triggered window" at shallow depth (0-10km) range, and long "triggered window" within depth range of 10-20km. b) and e) are estimated dynamic stress changes, max(sqrt(J_2)), at points in crust at similar depths. c) and f) indicate the defined dynamic stress "susceptibility".

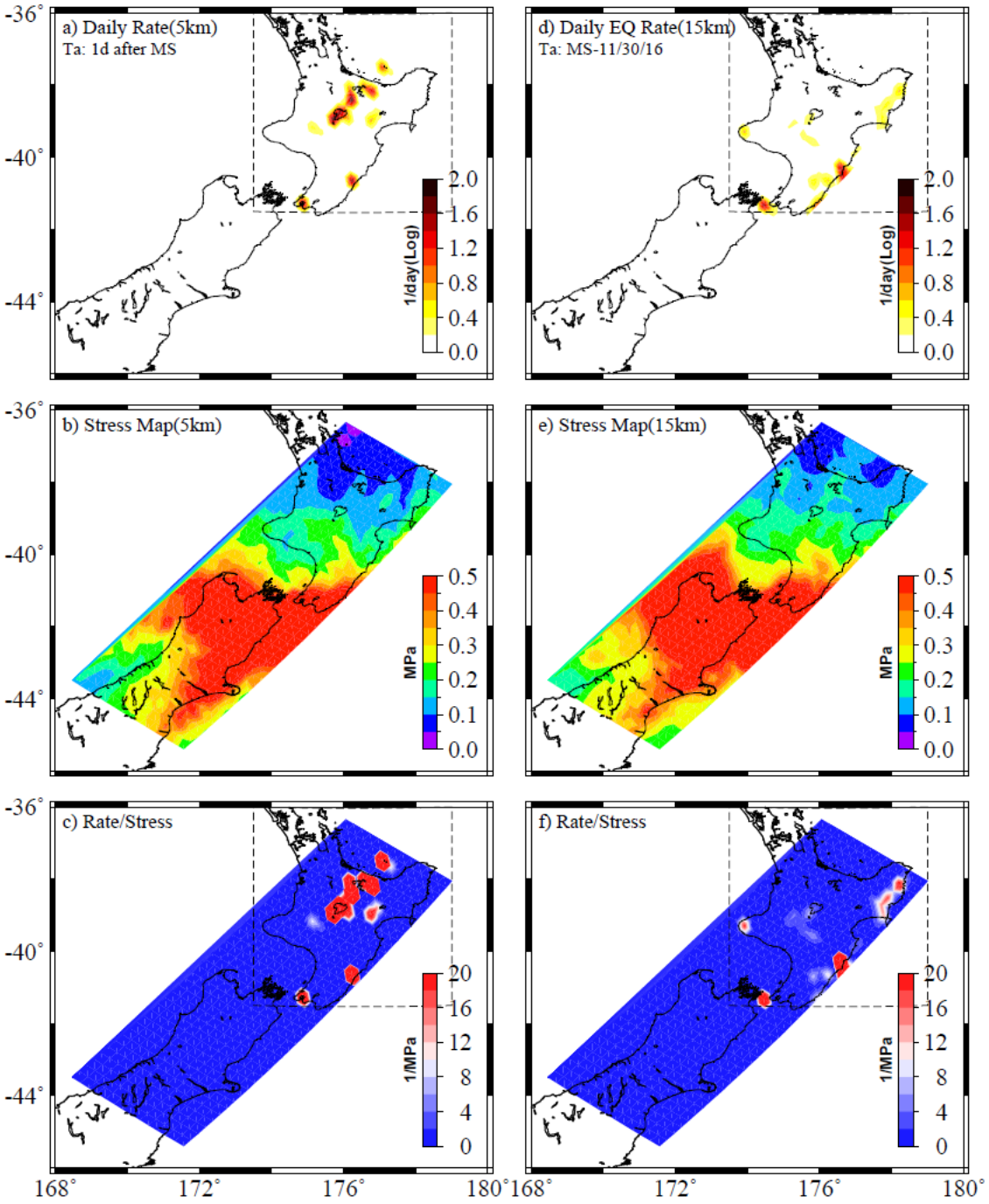

Figure 3.14 Comparison between the daily seismicity rate and calculated dynamic stress for the refined detection. Source model of *Wang et al*. [2018] is applied, similar to **Figure 3.12.**

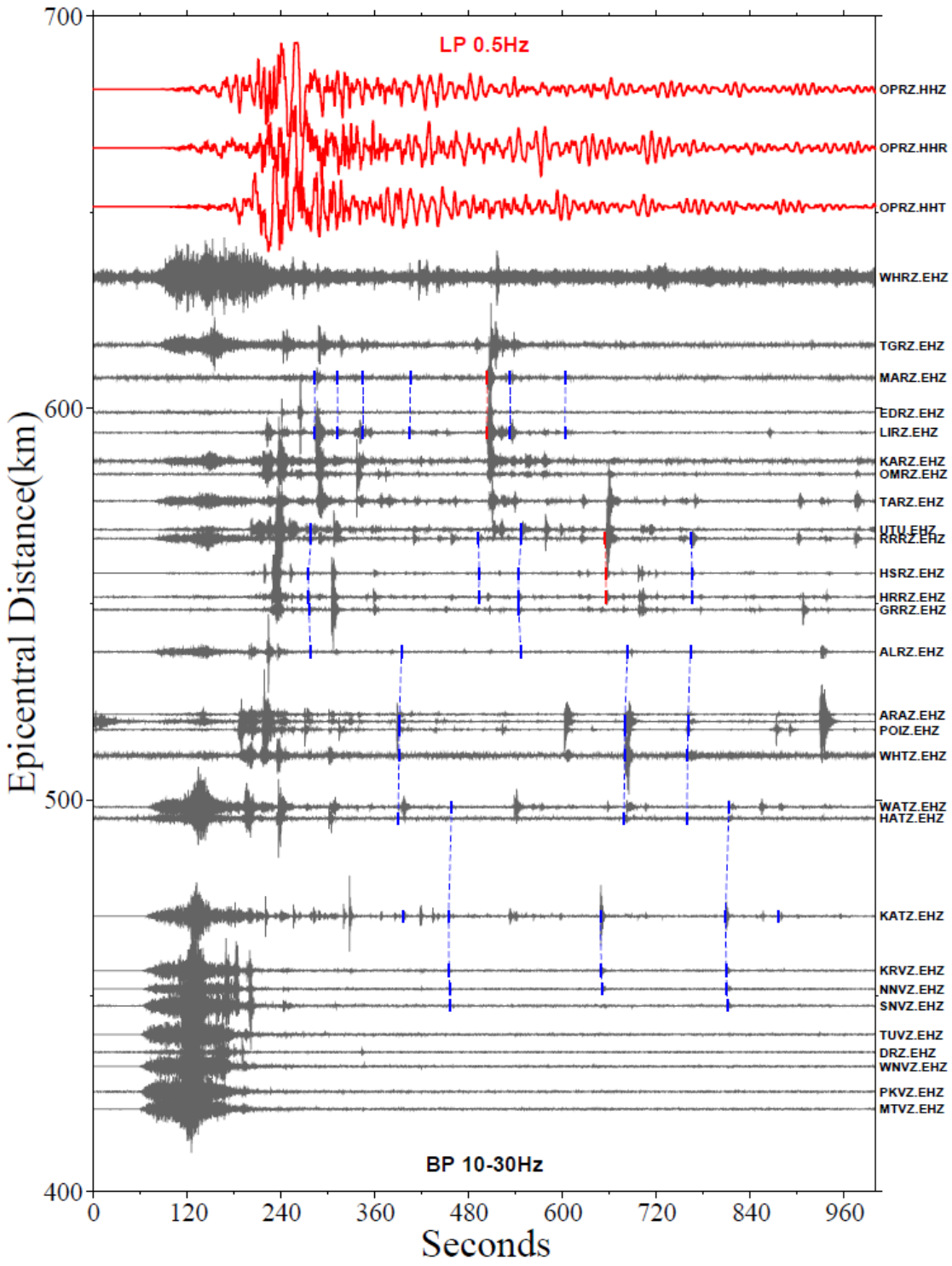

Figure 3.15 Detection result within the first 1000s for the refined detection. Grey waveforms are bandpass filtered using a 10-30 Hz filter and aligned with epicentral distances. Top red waveforms are lowpass filtered to show the surface wave. Red dashed lines show linked phase picks for catalog events, while blues are for newly detected events. STATION.CHANNEL are labeled to the right.

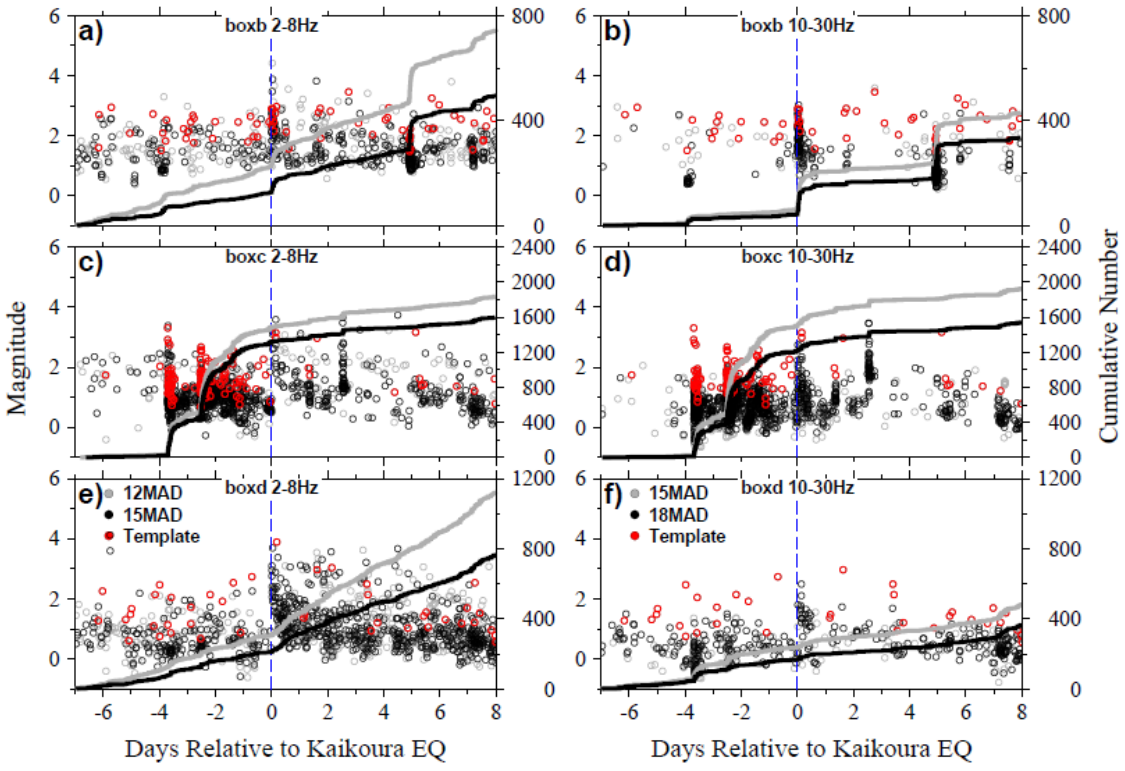

Figure 3.16 Comparison of the detection result using different filters. a) and b) are for box b, c) and d) for box c and e) and f) are for box. Symbols and color scheme are similar to Figure 3.7.

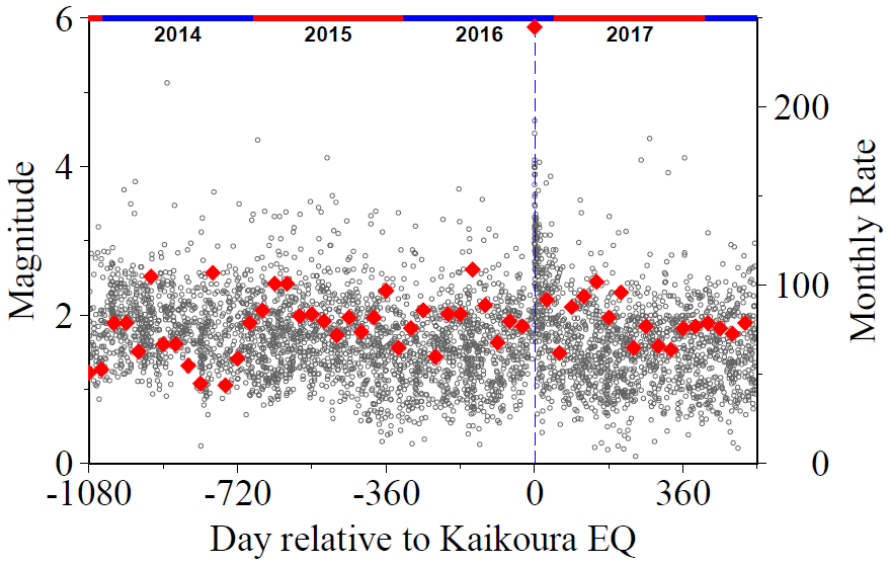

Figure 3.17 Long-term seismicity within Box e (Figure 3.7e). Gray circles are catalog events listed in GeoNet, while red diamonds show the monthly seismicity rate.

CHAPTER 4. DETAILED SPATIO-TEMPORAL EVOLUTION OF MICROSEISMICITY AND REPEATING EARTHQUAKES FOLLOWING THE 2012 M_W 7.6 NICOYA EARTHQUAKE

4.1 Introduction

In this study, we analyzed available seismic data around the 5 September 2012 M_w 7.6 Nicoya earthquake in Costa Rica. The existence of the Nicoya Peninsula enables very near-field seismic and geodetic observations of megathrust seismogenesis, as it brings the coastline within 50 km of the trench, allowing land-based geophysical studies directly over the main locking and slip environment, while the seismogenic zones exist entirely offshore in most environments. As anticipated, the Nicoya earthquake ruptured a seismic gap beneath the Nicoya Peninsula that locked up following a *M* 7.7 event in 1950, and exhibiting an apparent 50-60 year recurrence of M_w 7.0+ earthquakes along the megathrust [*Protti et al.*, 2001]. After nucleating immediately offshore [*Yue et al.*, 2013], the Nicoya earthquake ruptured primarily under the peninsula with up to 4 m of trenchward thrust in an area that was previously mapped as locked [*Feng et al.*, 2012*; Protti et al.*, 2014*; Kyriakopoulos and Newman*, 2016]. Local foreshocks were observed 35 minutes prior to the mainshock within 15 km of its hypocenter, which occurred within the same 30 km diameter zone as those remotely triggered by the 27 August 2012 M_w 7.3 El Salvador event about 450 km to the northwest [*Walter et al.*, 2015]. *Kyriakopoulos et al*. [2015] derived a new structural model for the subduction zone interface along the Middle America Trench. This plate geometry model was further used to reevaluate the interseismic locking and coseismic slip [*Kyriakopoulos and Newman*, 2016], and image

afterslip both updip of the dominant coseismic slip area, and downdip to deep slow slip events previously identified [*Hobbs et al.,* 2017].

As an extension of the growing body of work in the area, we explored the detailed spatio-temporal evolution of aftershocks along the Nicoya megathrust using the NWMFT to better understand physical mechanisms of aftershock triggering and how megathrust faults recover in the postseismic period. In addition, we searched for potential repeating earthquakes with virtually identical waveforms [e.g., *Nadeau et al.,* 1995; *Peng and Ben-Zion,* 2006] and used them to better understand postseismic deformation [*Schaff et al.,* 1998*; Peng et al.,* 2005*; Kato and Igarashi*, 2012].

4.2 Study Region and Seismic Data

With land directly on top of the seismically active subduction interface, the Nicoya Peninsula is an ideal place to study megathrust slip processes. Besides regular earthquakes, both shallow and deep SSEs [*Jiang et al.,* 2012; *Dixon et al.,* 2014], as well as tectonic tremors/LFEs have been identified in this region [*Brown et al.,* 2009; *Walter et al.,* 2011, 2013], demonstrating a broad spectrum of fault slip phenomena [*Peng and Gomberg*, 2010]. The smoother and colder Cocos plate originating from the East Pacific Rise (EPR) subducts beneath the Peninsula to the north, while the rougher (with many seamounts) and warmer seafloor created at Cocos-Nazca Spreading center (CNS) converges with the Caribbean plate to the south with an average rate of 82 mm/yr in the N20°E direction (Figure 4.1a) [*DeMets et al.,* 2010]. This is consistent with the along-strike variation in the updip limit of the seismogenic zone and strong variations in the megathrust interface structure [*Newman et al.,* 2002; *Kyriakopoulos et al.,* 2015], as well

as an along-strike variation in the temperature profile of the incoming oceanic plate [*Harris and Wang*, 2002; *Hutnak et al.*, 2007].

During the past two decades, numerous seismic and geodetic instruments were deployed in this region [*Dixon et al.*, 2013]. Geodetic instruments are composed of campaign and continuous GPS sites initiated in the early 1990s [*Lundgren et al.*, 1999]. These data were instrumental in imaging interseismic coupling with strong along-strike variability along the subducting interface [*Feng et al.*, 2012], which were used to estimate the potential location and maximum moment release for the impending 2012 Nicoya earthquake [*Protti et al.*, 2014].

Starting with a 1.5-year deployment by the University of California, Santa Cruz (UCSC) of 20 short-period and broadband sensors beginning in late 1999, the Nicoya Peninsula has been well-instrumented with seismometers to date. The current network YZ, has remained relatively unchanged since 2008 (Figure 4.1a), and consists of a 17-station seismic network operated by UCSC, Georgia Tech and the Costa Rica Volcanological Observatory at the National University (OVSICORI-UNA) providing continuous recordings before, during and after the 2012 Nicoya mainshock [*Dixon et al.*, 2013]. The network consists of 14 broadband and 3 short-period sensors recording initially at between 40 and 50, and currently at 100 samples per second. As shown in Figure 4.2, about 10 stations were working continuously immediately following the mainshock.

In this study, we analyzed data between July and December 2012, about 2 months before and 4 months following the M_w7.6 mainshock. The cataloged events were first

identified within the *Antelope* seismic database system (http://www.brtt.com) using an automatic detection algorithm followed by analyst-revision of phase picks [*Walter et al.*, 2015]. Events were then relocated with SimulPS [*Evans et al.*, 1994] by incorporating available phase arrivals with a regionally developed tomographic 3D velocity model [*DeShon et al.*, 2006] (Figure 4.1a). Finally, we selected 7,890 earthquakes with at least 6 known phase arrivals for further analysis, hereafter we refer to these as the 'original catalog'. *Walter et al*. [2015] used a NWMFT on this initial catalog to identify dynamic triggering by the 2012 El Salvador earthquake near the nucleation region of the Nicoya earthquake and look for foreshock activities. This study is distinguished from the earlier one in that it focuses on the aftershock (post-mainshock) seismicity.

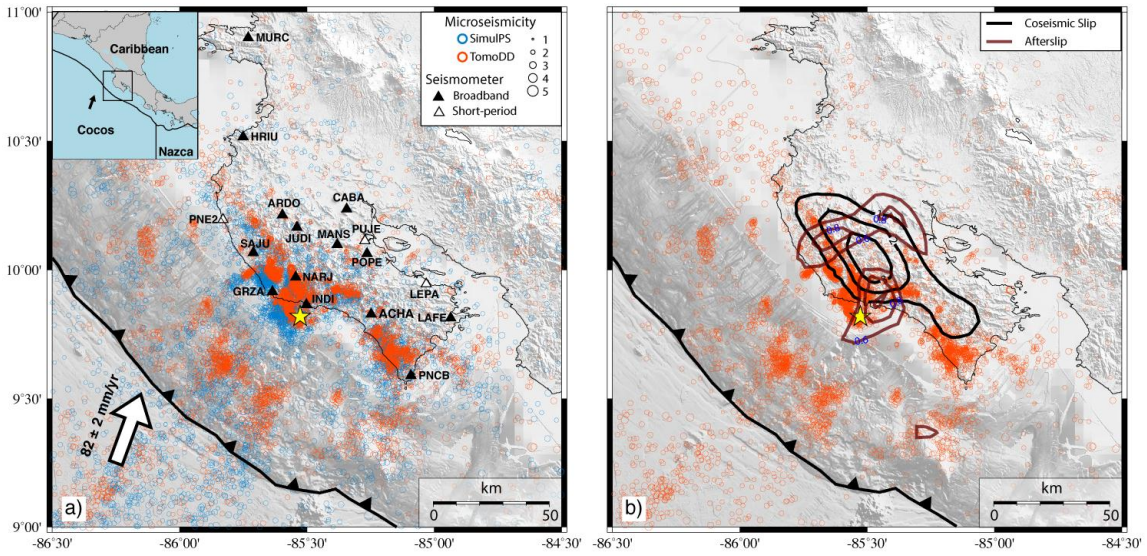

Figure 4.1 Map of the Nicoya Peninsula, Costa Rica (study region). a) Seismic network (triangles) and earthquake catalog using SimulPS (blue circles) [*Walter et al.*, 2015], and TomoDD (red circles), following the methodology and model described in *Kyriakopoulos et al.* [2015]. Inset shows the regional tectonic environment including Cocos plate subduction beneath the Caribbean plate at about 82±2 mm/yr near Nicoya [*Demets et al.*, 2010]. b) The TomoDD seismicity is shown with the geodetically inferred coseismic slip (1m thick black contours) [*Kyriakopoulos and Newman*, 2016], and postseismic deformation modeled as afterslip through the end of 2012 (0.25 m maroon contours starting at 0.5 m) [*Hobbs et al.*, 2017]. The yellow star marks the mainshock epicenter. The geodetic slip models both use the seismically defined 3D slab structure of *Kyriakopoulos et al.* [2015].

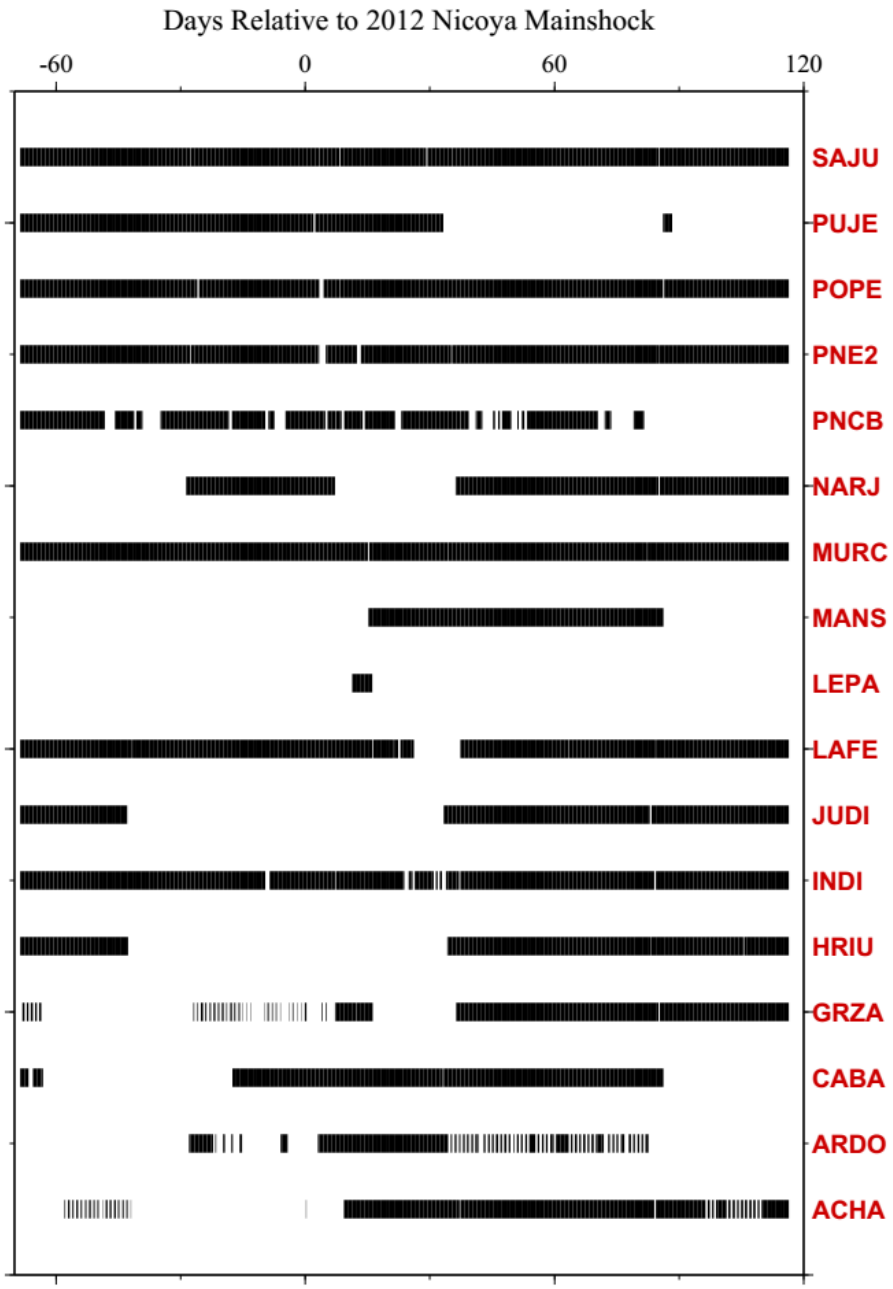

Figure 4.2 Temporal availability for different stations around the 2012 Nicoya mainshock. Station names are marked to the right.

4.3 Analysis Procedure

4.3.1 *Phase detection and catalog relocation*

Beginning with raw waveforms from the original catalog, we filtered them between 2-15 Hz to suppress noise from regional and teleseismic events as well as background noise with dominantly low-frequency energy. Additional phases were then identified using an automatic phase picker that repeatedly predicts arrivals with an initial velocity model, searches for phases using detector functions, and inverts the new velocity model [*Li and Peng*, 2016], with additional manual phase picking and adjustment (Figure 4.3). We then applied the new phase information to relocate events within T*omoDD* [*Zhang and Thurber*, 2003]. Both the absolute and differential times were used to better constrain their relative locations.

In detail, we first used the *ph2dt* program [*Waldhauser and Ellsworth*, 2000] to obtain differential travel times by searching catalog *P* and *S* phases for event pairs at common stations. We optimized the connectivity between events by selecting well-linked pairs and removing outliers when their delay times were larger than the maximum expected value of 5s. The parameters were optimized for the network geometry and seismicity distribution, where 10 km was chosen as the maximum hypocentral separation between event pairs and a minimum of 8 links required for clustering. The new travel-times were utilized in TomoDD, including the most updated 3D velocity model in this region [*Moore-Driskell et al.*, 2013], to obtain the best-constrained locations.

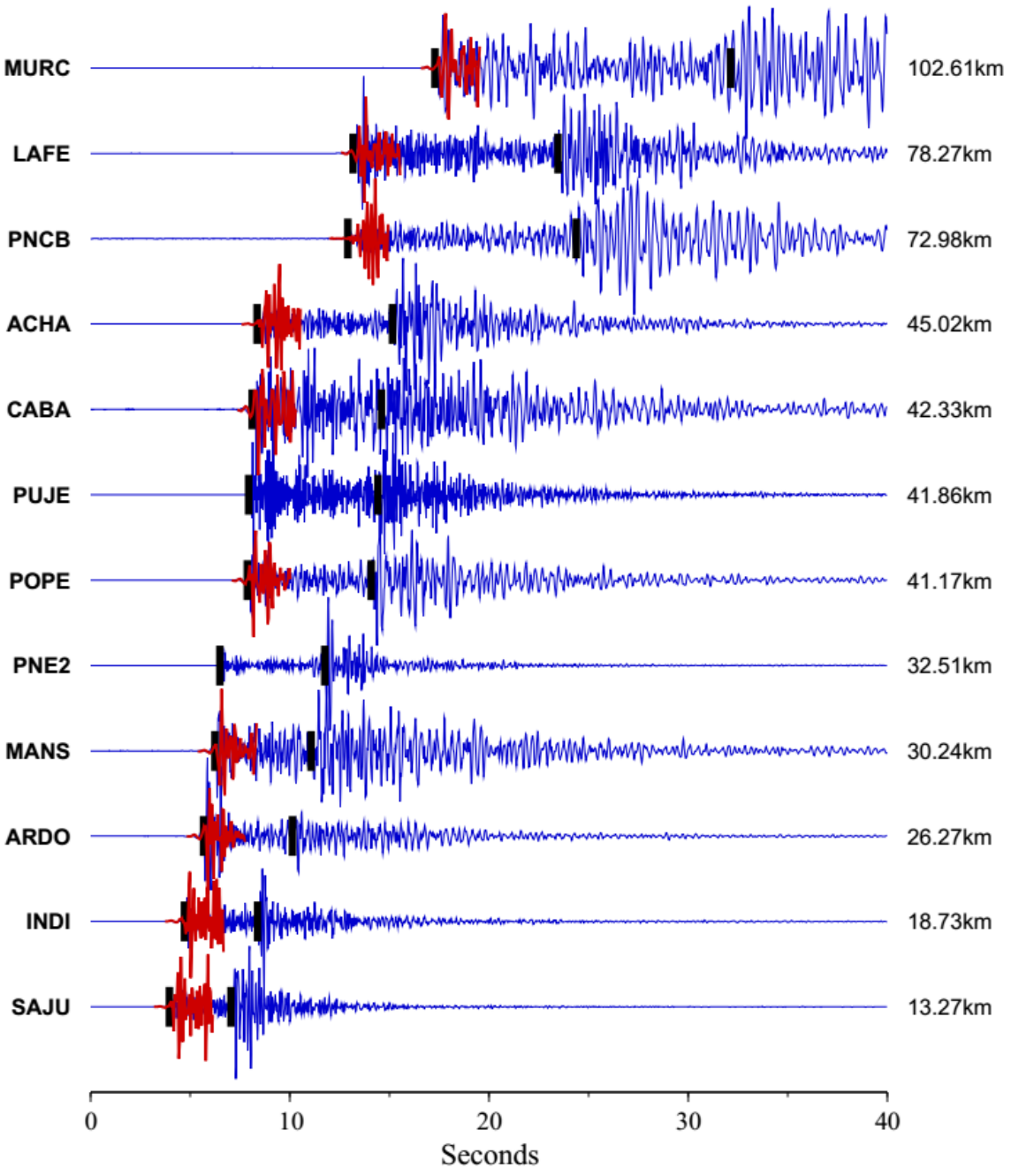

Figure 4.3 An example showing the updated phase library. Original phases are marked with red waveforms, while the dark bars indicate the resulting available phases. Station name and epicentral distances are marked to the left and right sides, respectively.

4.3.2 *Matched-filter detection*

The relocated events were then used as templates to perform the matched-filter detection. The procedure follows those in *Meng et al.* [2013] and is briefly described here. Since epicentral distances are generally within 150 km, we used a 6s window (1s before and 5s after) around the *P* and *S* waves for vertical and horizontal channels separately and used them to compute cross-correlation (CC) functions with continuous data. To avoid noisy traces and suppress artificial detections, we computed the SNR for all traces by taking 1s before and 5s after the P or S arrival time as the signal window and the same length window ending 1s before the P arrival as the noise window. Only template events having more than 9 traces with SNRs greater than 5 were used. Next, we shifted each CC function for individual components back to the origin time of the templates, and stacked all shifted functions to suppress uncorrelated background noise and enhance earthquake signals. We distinguished an event as a new earthquake detection if the stacked CC function exceeds a threshold of 12 times median absolute deviation (MAD) of daily mean CC functions, a threshold similar to previous studies [*e.g., Meng et al.*, 2013; *Meng and Peng*, 2014, 2015; *Yao et al.*, 2015; *Li et al.*, 2017]. We then combined all detections and removed duplicates by keeping only the highest CC event per 3-s window [*Peng and Zhao*, 2009; *Meng et al.*, 2013]. Finally, the locations of the detected events were assigned the same location as the best-matching template. The local magnitudes (M_L) of the detected events were computed by the median peak amplitude ratio between the template and detected events [*Peng and Zhao*, 2009].

4.3.3 *Repeating earthquakes*

We then searched for repeating event pairs, defined as those with mean CC values higher than 0.9, excluding self-detections [*e.g., Kato et al.*, 2012]. If an event is detected

by multiple templates with CC>0.9, all the templates and corresponding CC values are kept. Next, we grouped the event pairs into clusters using an equivalency class (EC) algorithm [*Press et al.*, 1986; *Peng and Ben-Zion*, 2005], which allows an inclusion of a new event into a cluster if the new event has a mean CC value > 0.9 with any existing members in that cluster. As mentioned above, we relocated all 7890 catalog events using only catalog phases in TomoDD with a refined 3D velocity model, which could help to constrain both the absolute and relative locations. We didn't combine with waveform cross-correlation differential time mainly because the catalog includes events across a wide region, and it would cause more computation cost when compared to the potential improvements on relative relocations. On the other hand, to confirm whether events have overlapping rupture patches within each cluster, we further relocated them in HypoDD [*Waldhauser and Ellsworth*, 2000] with a simple 1D velocity model by applying waveform cross-correlation differential time with sub-sample accuracy to reduce relative location errors [*Schaff et al.*, 2002]. To estimate the patch size, we assumed an average strain drop of 10^{-4} [*Kasahara*, 1981], a circular crack model [*Kanamori and Anderson*, 1975; *Ben-Zion*, 2003], and an empirical potency-magnitude relationship for earthquakes with magnitudes M<3.5 (Eq. 2) [*Ben-Zion and Zhu*, 2002].

$$r^3 = \left(7/16\right)\left(P_0/\Delta\varepsilon\right)$$
$$\log P_0 = 1.00M - 4.72 \qquad \text{(Eq. 2)}$$

where r is the circular radius (in meters), P_0 is the scalar potency (in km^2*cm) and $\Delta\varepsilon$ is the static strain drop. Any events that were clearly outside the rupture patches of others were either dropped, or separated into different sub-clusters. Finally, we estimated the

amount of cumulative seismic slip for each cluster. Specifically, seismic slip for every event was calculated with aforementioned scalar potency and rupture area (Eq. 3, assuming circular crack):

$$d = P_0 \Big/ \left(\pi r^2\right) \quad \text{(Eq. 3)}$$

where d is the averaging seismic slip. Finally, we summed the clustered events to obtain the cumulative slip within each cluster.

4.4 Results

4.4.1 *TomoDD relocation results*

We were able to relocate approximately 7,750 events from 06/19/2012 to 12/30/2012 (Figure 4.1), while the rest 140 events were dropped by the TomoDD program. The relocated events formed two broad groups approximately 50-60 km in diameter beneath the western coast of the Nicoya Peninsula (Figure 4.1b). The first one is located along the terminus of the major coseismic slip patch, which partially overlaps shallow afterslip through the end of 2012 [*Hobbs et al.*, 2017]. The second group of seismicity is near the southern edge of the peninsula, where little resolvable afterslip was observed.

To explore the depth distribution of relocated events, we plot the seismicity along several trench-normal (N45°E) cross-sections (Figure 4.4). The seismicity to the northwest of and around the mainshock epicenter (e.g., profiles b, d, e, and f) clearly outlines a linear feature that dips between 14-20° to the northeast. However, seismicity

further south (e.g., profiles g, h and i) appears more diffuse and does not seem to be on any linear interface.

We also observed along-strike variation of seismicity when plotting the depth distribution along the trench parallel (N45°W) direction (Figure 4.5). The updip limit of the seismicity changed from ~20 km at depth in the northwest to shallower portion (~10km depth) in the southeast, consistent with observations from the Costa Rica Seismogenic Zone Experiment (CRSEIZE) [*Newman et al.*, 2002].

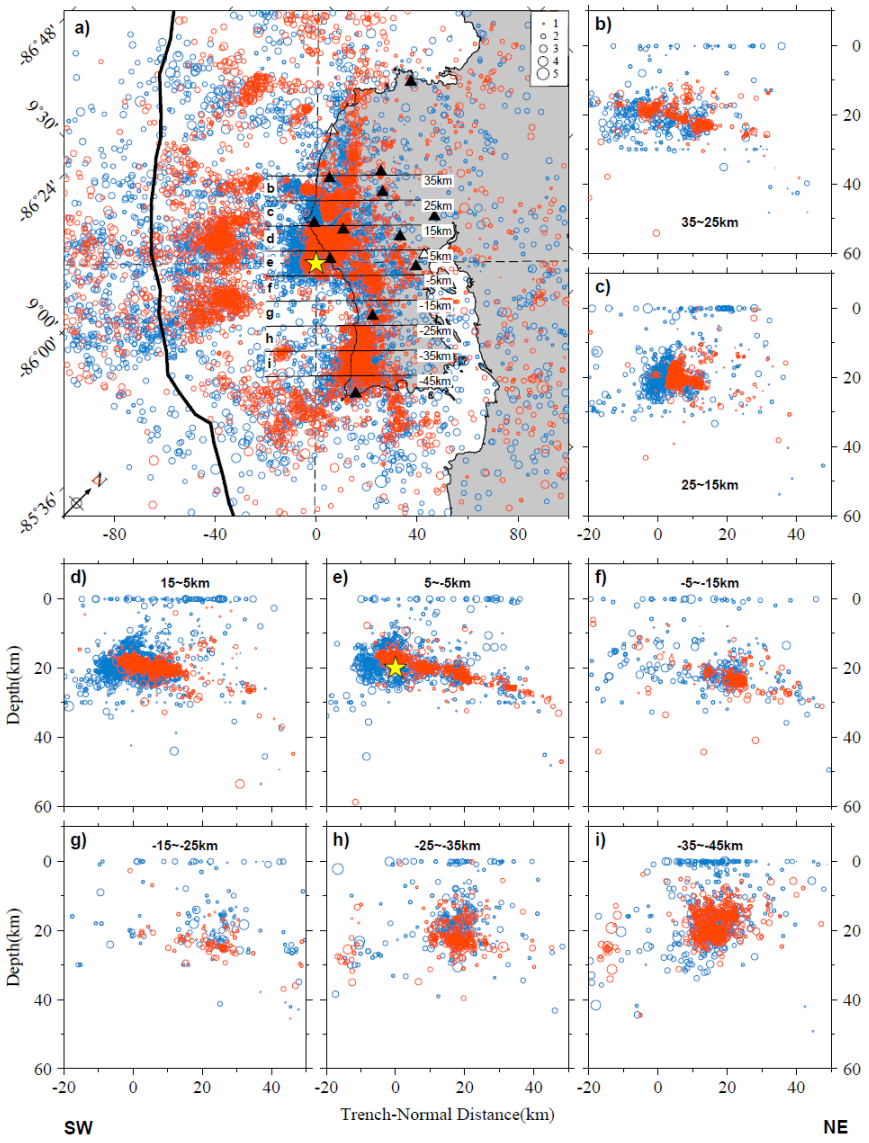

Figure 4.4 Details of relocated earthquake distribution. a) All events projected along N45°E, the approximate trend of the Middle America Trench offshore Nicoya, with the x-axis describing the position (in km) relative to the mainshock epicenter (yellow star at -85.527°, 9.819°). Seismicity located using SimulPS (blue circles; *Walter et al.* [2015]) are shown with TomoDD relocations (red circles) found using a local three-dimensional velocity model [*Moore-Driskell et al.*, 2013]. Trench-normal lines representing the bounds on profile bins (marked corresponding to their panel) are labeled with their trench-parallel distances from the mainshock epicenter. b-i) the depth profile within each bin. Bin (e) includes the focus of the mainshock (depth = 20 km).

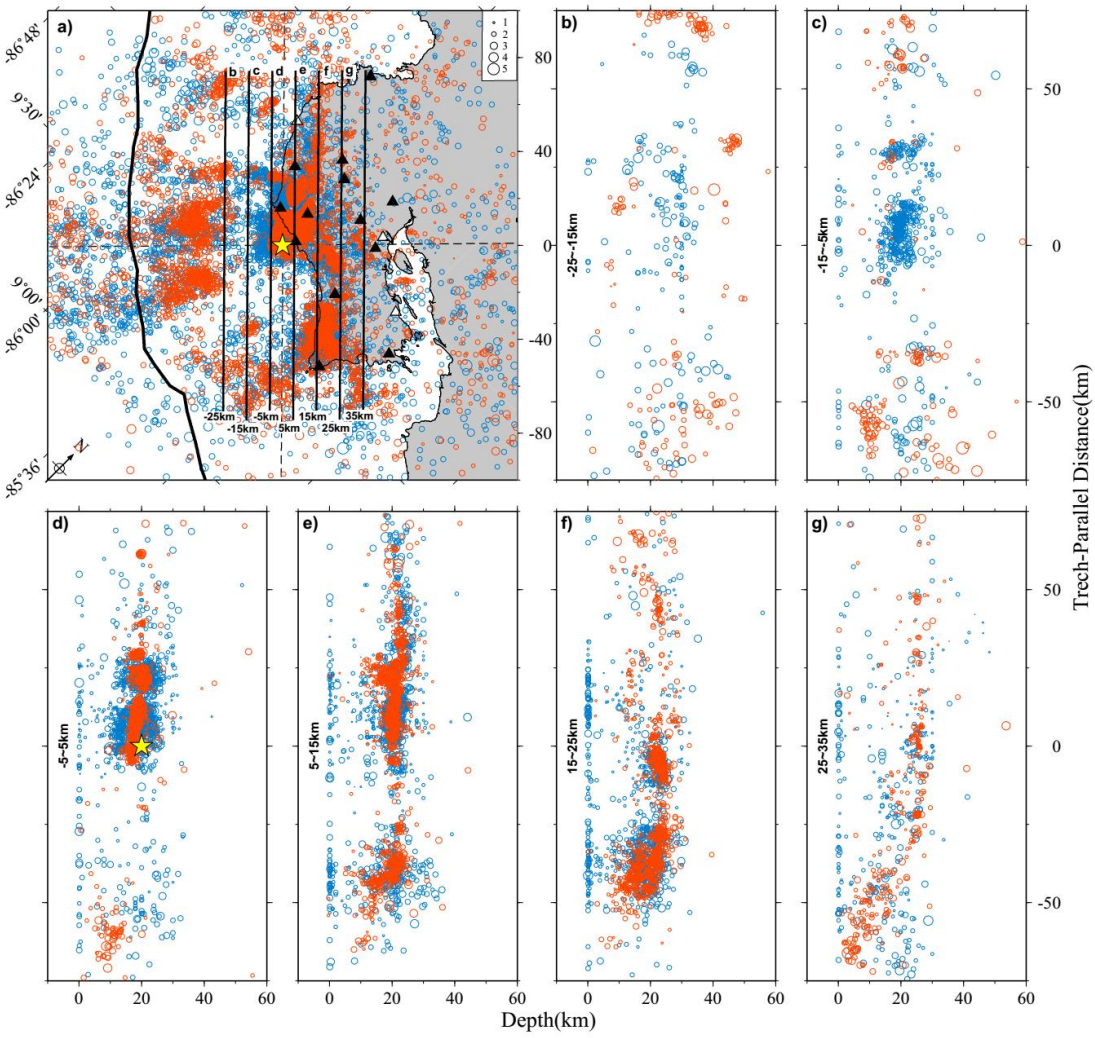

Figure 4.5 Seismicity depth distribution along the trench parallel direction. a) All events are projected along N45E and use the mainshock epicenter (longitude: -85.5271, latitude: 9.8193, depth: 20 km; yellow star) as the projection center. Seismic activities before (blue circles) and after (red circle) relocations are plotted. The trench-normal distances relative to the mainshock epicenter and bin ids are labeled to the bottom and top, respectively. b-g) the depth profile within each bin.

4.4.2 *Earthquake detection results*

We cross-correlated the waveforms of 7,750 relocated events with continuous recordings from 29 June 2012 through 30 December 2012. After the analysis, ~132,900 new events were detected (Figure 4.6). This includes ~129,800 events with robust

magnitude determinations, and ~3,100 events with unreliable magnitudes. The unreliable event magnitudes are the results of templates without valid magnitudes from Antelope, which occurs when the SNR is lower than 3 for an individual phase. These are typically events with low magnitudes, and we arbitrarily assign them a magnitude of 0 in Figure 4.6, but did not use those events in subsequent analysis. The magnitude of completeness (M_c) drops from 2.0 for original catalog to 1.3 after including all detected events (Figure 4.7). A clear increase of seismicity was observed immediately following the mainshock as well as after its largest aftershock (Figure 4.6a). In addition, we also observed an increase of local seismicity following the 2012 M_w 7.3 El Salvador event, which was interpreted as remotely triggered seismicity in the epicentral region of the Costa Rica mainshock [*Walter et al.*, 2015]. Figure 4.6b shows a clear reduction of the magnitude of the smallest event with logarithmic times since the mainshock. It is worth noting that while the overall M_c value is 1.3, this value is much higher immediately after the mainshock. This is commonly observed right after moderate to large earthquakes [e.g., *Peng and Zhao*, 2009; *Tang et al.*, 2014], and is most likely caused by missing small earthquakes immediately following the mainshock when the seismicity rate is high [*Hainzl*, 2016], even after matched filter detection.

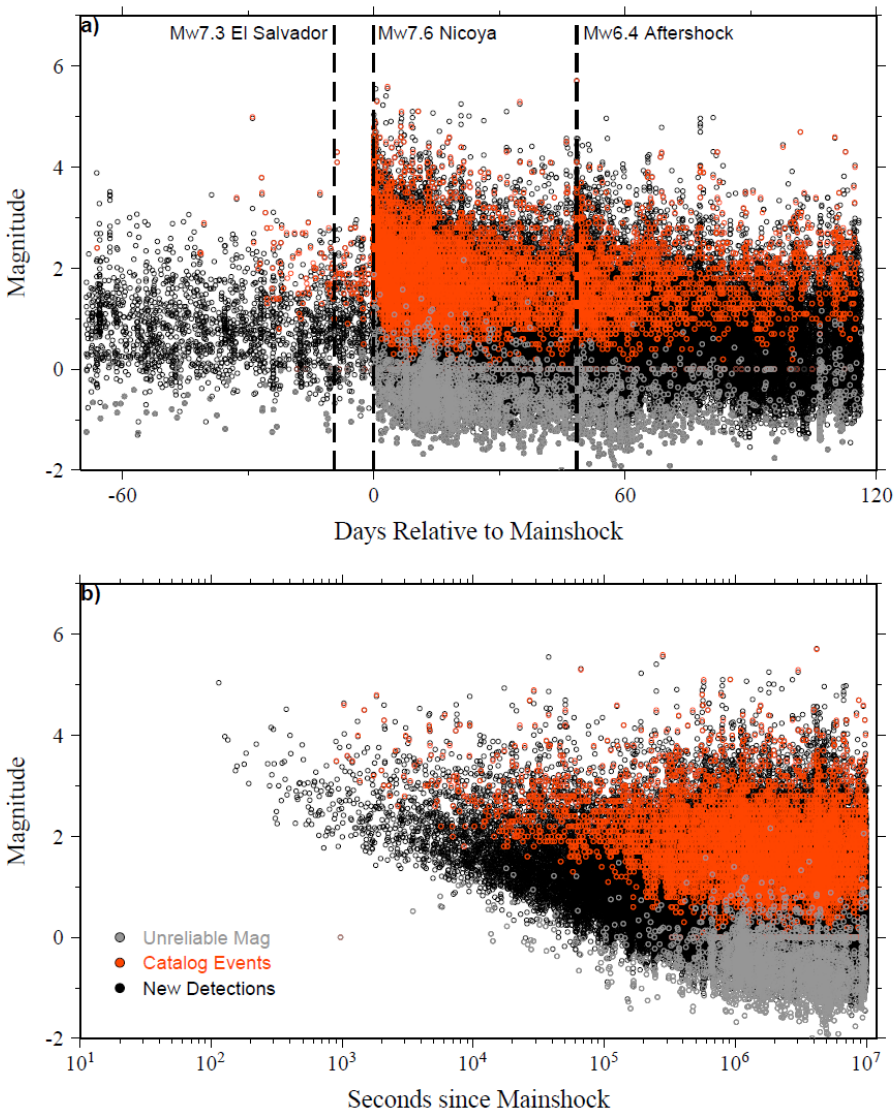

Figure 4.6 Time series of the waveform matching catalog. a) Magnitude distribution with linear time scale for all detections from 06/29/2012 to 12/30/2012. b) Aftershock magnitude distribution with logarithmic time since the mainshock. Red and dark circles represent catalog template events and newly detected events, while gray circles mark catalog events without reliable magnitude and the associated detected events.

We projected all events to both trench-parallel and trench-normal directions, in the same way as Figure 4.4 and Figure 4.5, to further examine the spatio-temporal evolution of seismicity following the mainshock in three adjacent time windows: 0-0.1h, 0.1h-0.5h and 0.5h-5h (Figure 4.8). We found that the earliest aftershocks (i.e. in the first half hour) occurred right around the mainshock slip patch along the interface at the depth

range of about 15-30 km (Figure 4.8a & b). Such a pattern is barely visible in the original catalog with only a few events in the first half hour after the mainshock (Figure 4.8d). In comparison, the majority of aftershocks occurring further to the southeast near the tip of the Peninsula activates slightly later.

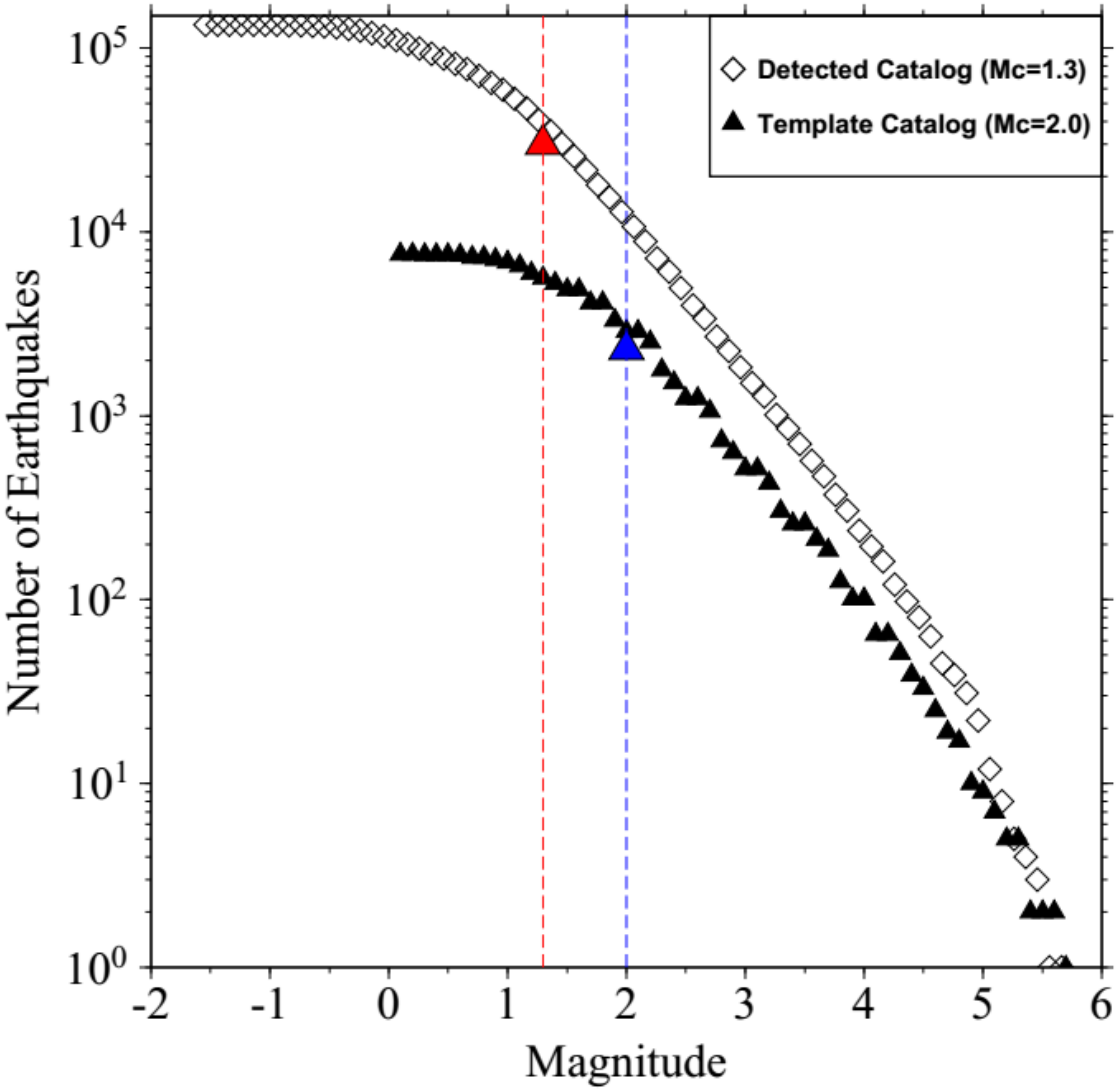

Figure 4.7 Gutenberg-Richter (G-R) law. Diamonds show the cumulative number of earthquakes, while black triangles are number of events for different magnitude bins. a) Original catalog, b) Detected catalog. Red bold curves are maximum-likelihood G-R fitting. The *Mc* and b value are labeled in each panel.

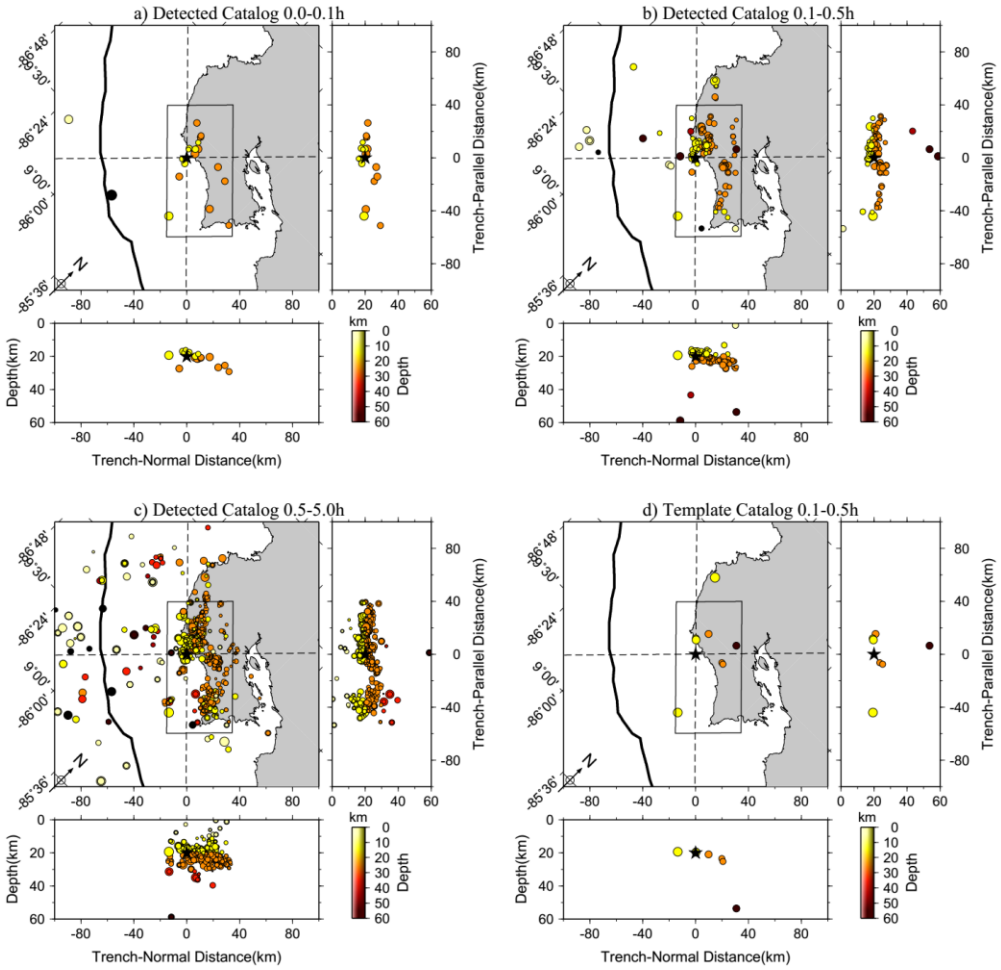

Figure 4.8 Spatio-temporal evolution of early aftershocks. Each panel shows a different time window following the mainshock, where the top-left is a map view of seismicity after a 45 °clockwise rotation, and the trench-normal and trench-parallel distributions within the shown box are plotted at the bottom and to the right, respectively. Events are color-coded with depth. Following the mainshock the individual panels show; a) 0-0.1h for the detected catalog; b) 0.1-0.5h for the detected catalog; c) 0.5-5h for the detected catalog; d) 0.1-0.5h for the template catalog.

To better define the aftershock expansion pattern, we followed recent work by *Kato and Obara* [2014] and defined the activation of aftershocks at the time when the cumulative numbers of aftershocks within a 5-km wide zone (either along or perpendicular to the trench) exceed a certain number *N*. We slid the window per 1 km in order to achieve a better spatial resolution. As shown in Figure 4.9 (*N*=30), both groups showed moderate expansion in trench-parallel and normal distances with logarithmic

times since the mainshock. We also set *N=10,* 20, 30, 40, 50 to examine how the choice of such parameter affected the results, and they showed similar patterns. In addition, there was a gap between the seismicity beneath the Peninsula and offshore seismicity (with depths between 10-15 km, Figure 4.4d and Figure 4.4e) as well as a clear cutoff edge for seismicity to the northwest (Figure 4.1b). While the main zones of aftershock seismicity were active seconds to minutes after the mainshock, the seismicity close to the trench (depth < 10km) became activated a few days after the mainshock.

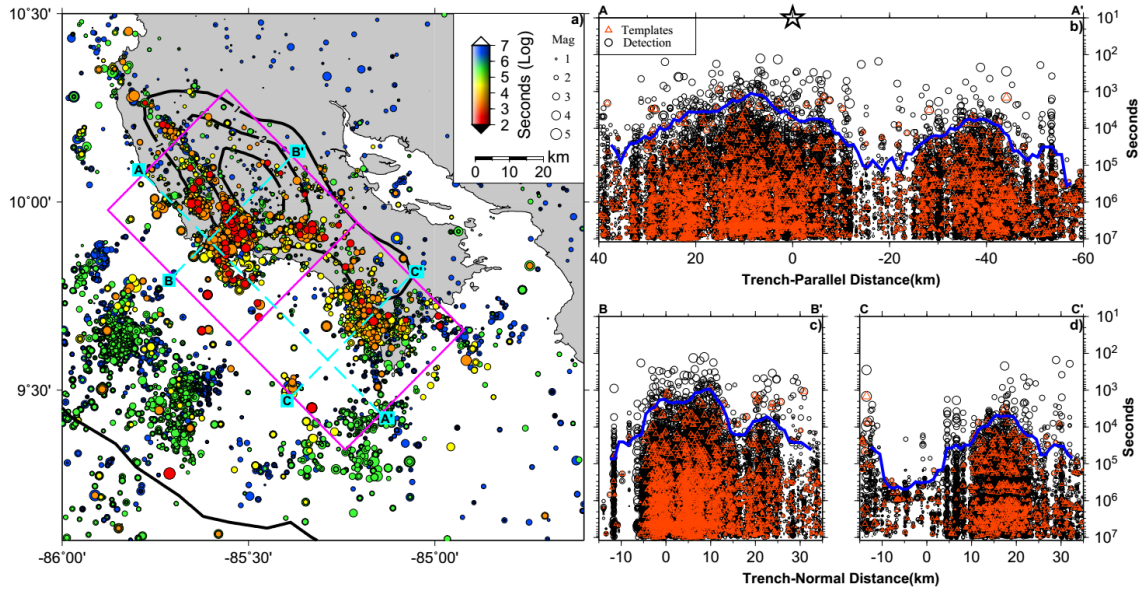

Figure 4.9 Migration of the 2012 Nicoya aftershocks. a) Map view of all the detected events color-coded by the logarithmic time after the mainshock (white star). The thick black contours denote the 1m coseismic slip [*Kyriakopoulos and Newman*, 2016]. b) The occurrence times of aftershocks since 2012 Nicoya mainshock (open black thick star) versus trench-parallel distances (AA'). The black circles and red triangles mark the events listed in the template catalog and detected by the match filter technique, respectively. Blue thick line indicates the activation of aftershock, following *Kato and Obara* [2014]. c) The occurrence times of aftershocks within the earthquake group to the northwest since the mainshock versus trench-normal distances (BB'). d) The same as c) for the earthquake group to the southeast (CC').

4.4.3 *Repeating pairs and clusters*

We initially identified repeating clusters as detection pairs with mean CC values above 0.9. About 1170 repeating pairs were identified, which were further grouped into 53 clusters with ~370 earthquakes, each of them containing at least four events. Figure 4.10 shows an example cluster of earthquakes occurring immediately offshore and near station SAJU. The waveforms recorded by the vertical component are highly similar (Figure 4.10a). Likewise, after relocation the source patches for events within the cluster nearly overlap (Figure 4.10d), based on the model assumptions described in section 4.3.3, indicating that they are indeed repeating earthquakes occurring at the same source region. Similar to previous observations [*Schaff et al.,* 1998; *Peng et al.,* 2005], their recurrence times increase systematically with time since the mainshock, with an apparent Omori-law decay constant, p=0.77 (Figure 4.10c).

Figure 4.11a shows the locations of all repeating earthquake clusters and afterslip through the end of 2012, while the spatio-temporal distribution of regular and repeating aftershocks along the trench-parallel direction can be found in Figure 4.12a. We found that most repeating clusters occurred in areas that are near the edge of, or areas that are largely devoid of modeled afterslip patches (Figure 4.11a). Most repeating clusters occurred on or near a linear dipping feature likely defining the seismogenic plate interface (Figure 4.11b-f). Lastly, we found some repeating clusters became activated again following the largest M_w 6.4 aftershock (Figure 4.12a). A set of repeating earthquakes were also recorded after one of the largest aftershocks (M_w 5.4) with on June 23rd, 2013 [*Protti et al.*, 2013].

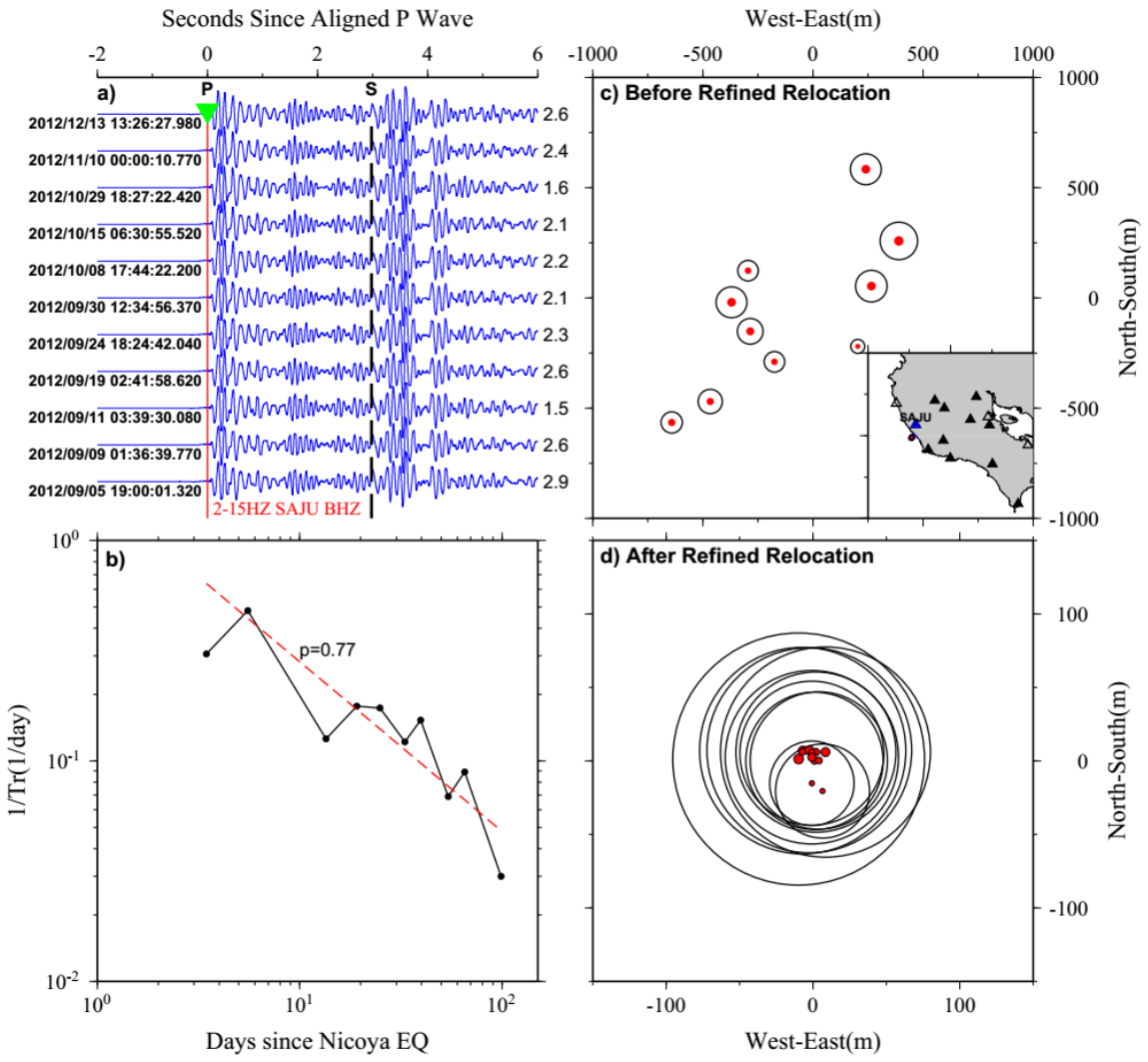

Figure 4.10 An example of a repeating cluster. a) Vertical component waveforms recorded by station SAJU. Event origin time and magnitude are marked to the left and right, respectively. P and S phases are labeled as thin red and thicker dashed black lines. b) With time from the mainshock, the inverse of the repeating cluster recurrence interval (Tr) is showed to roughly follow an Omori-type power-law with p = 0.77. c) and d) locations of all events before and after HypoDD refined relocations.

We find a general pattern of repeating clusters occurring very near the mainshock rupture patches immediately following the mainshock, which consequently tend to have larger cumulative slip (maximum of ~60 mm; Figure 4.12b). In contrast, clusters further

from the mainshock rupture exhibited some delay, are less frequent, and tend to have lower cumulative slip.

4.5 Discussion

High precision aftershock relocation using a well-constrained velocity model beneath the Nicoya Peninsula, together with waveform matching detection, resulting in an unprecedented spatial-temporal profile of the aftershock evolution following the 2012 Nicoya mainshock. Comparing these results to the most up-to-date images of the geodetically constrained coseismic and afterslip yield further insights into postseismic fault behaviour.

In this study, we observed anti-correlation between dominant coseismic slip (>3m) and aftershock density following the 2012 Nicoya mainshock (Figure 4.1b). In particular, aftershocks mostly occurred within the updip patch of the coseismic slip area (15-20 km depth). The overall pattern of aftershocks in this study was similar to those found elsewhere [*e.g., Schaff et al.*, 2002; *Thurber et al.*, 2006; *Hsu et al.*, 2006]. For example, following the 2005 M_w 8.6 Nias-Simeulue Sumatra earthquake, most aftershocks were found to be updip of the coseismic slip zone and along the plate interface [*Hsu et al.*, 2006].

The spatial distribution between aftershocks and afterslip, together with their temporal decay patterns [*Perfettini and Avouac*, 2007] and spatial migration [*Peng and Zhao*, 2009], led to the conclusion that most aftershocks around the mainshock rupture are triggered by stressing from a combination of coseismic and afterslip, with the latter more dominant in the weeks to months following the main event [*Perfettini and Avouac*,

2004]. In this study, we found that aftershocks occurred not only in regions partially overlapping the major afterslip, but also among patches practically devoid of afterslip (Figure 4.1b). This is consistent with recent observations that both tremor and microseismicity are outside of the main slip regions during slow-slip events along the Hikurangi subduction zone in New Zealand [*Bartlow et al.*, 2014], due to static stress changes outside the slow-slip region. However, alternative models, such as pore fluid diffusion, cannot be ruled out without further detailed analysis or modeling [*Bosl and Nur*, 2002; *Hainzl et al.*, 2016].

Between the large mainshock slip patches shown in, the aftershocks tend to follow a linear dipping structure (visible in Figure 4.4e), which is below the interface slab model obtained before using background seimicity prior to the Nicoya mainshock [*Kyriakopoulos et al.*, 2015]. While the result here is intriguing, additional relocations of both seismicity long before and after the mainshock, along with high-resolution seismic tomography are needed to obtain the interface properties beneath the Peninsula, which is the subject of ongoing work [*Newman et al.*, 2016]. Given minor differences found between slip models derived from the 3D slab geometry [*Kyriakopoulos et al.*, 2015], and simpler, but regionally appropriate 2D models [*Feng et al.*, 2012; *Protti et al.*, 2014], we do not expect any new interface derived from these aftershock data will alter our results reported here.

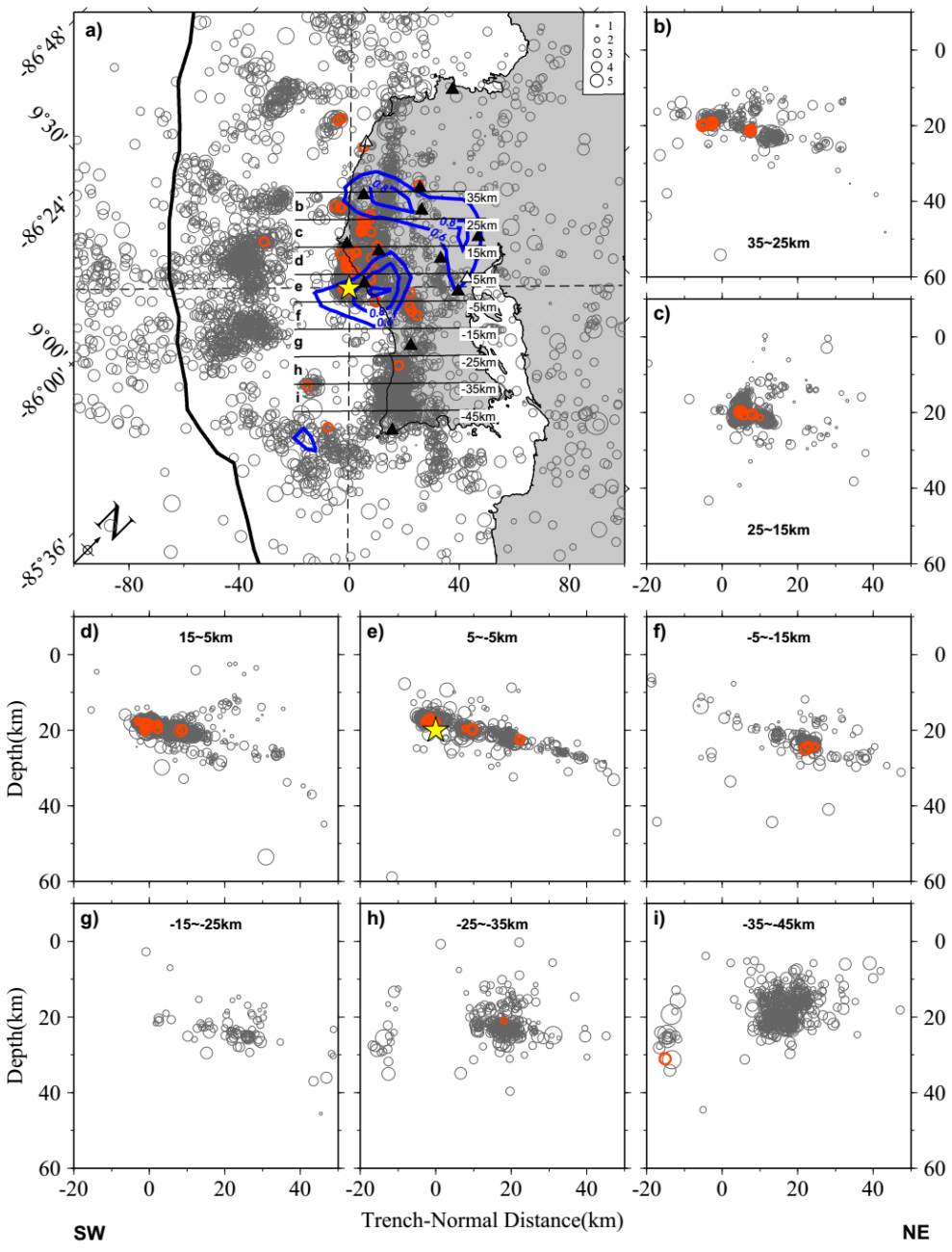

Figure 4.11 Spatial distribution of all repeating aftershock clusters. a) Map showing the locations of all repeating clusters (red open circles), with TomoDD aftershocks plotted as gray circles. Postseismic deformation modeled as afterslip through the end of 2012 (0.25m contours starting at 0.5m) marked with thick blue lines [*Hobbs et al.*, 2017]. Depth profiles (b-i), and their labeling follow Figure 4.4.

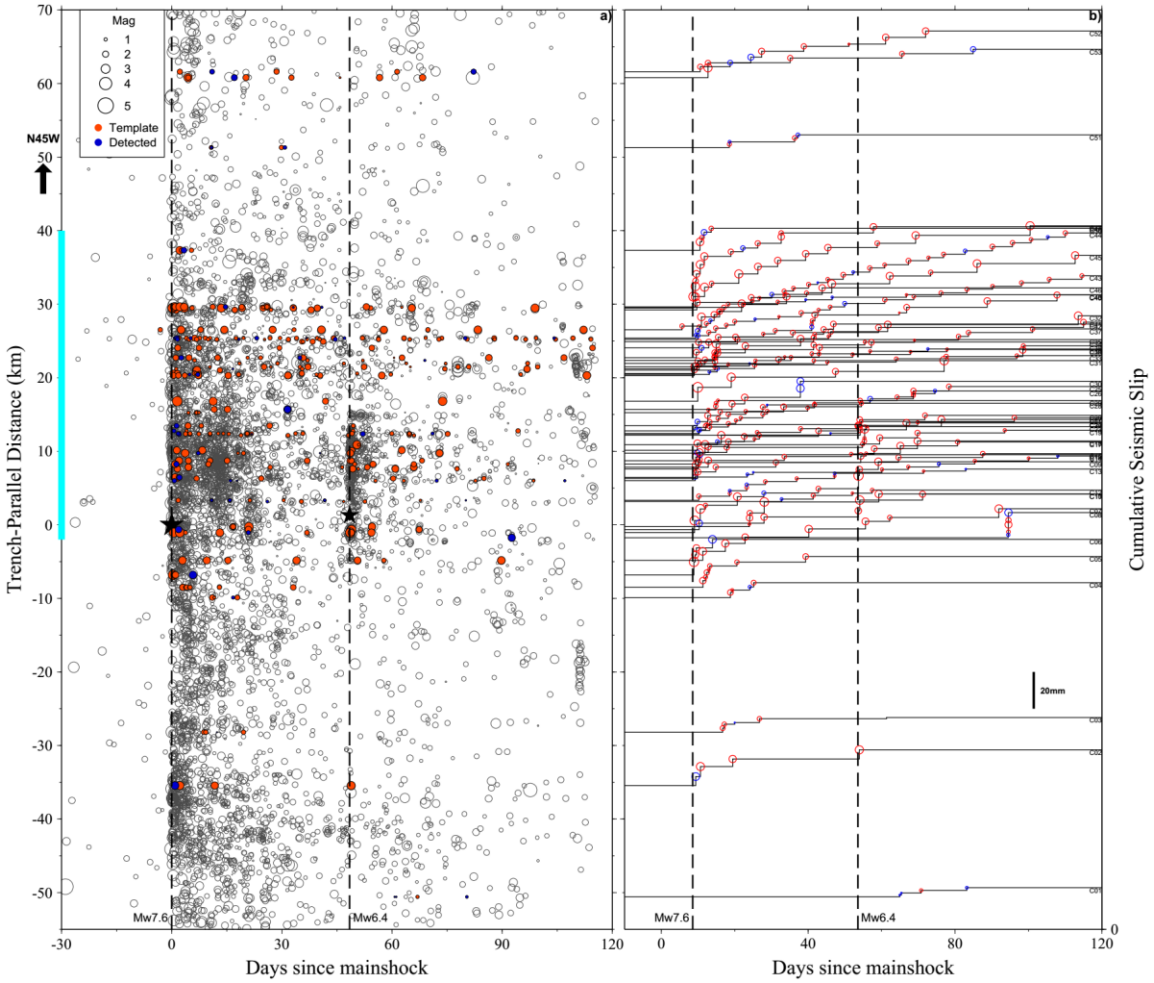

Figure 4.12 a) Spatial-temporal distribution of relocated template catalog events (gray open circles) and repeating events for each cluster (red/blue filled circles). All events were projected along N45W centered on the mainshock epicenter. Two vertical dashed lines marks the 2012 M_w 7.6 Nicoya mainshock and its largest M_w 6.4 aftershock (black stars). Cyan bar indicates the rupture dimension from coseismic slip distribution [*Protti et al.*, 2014]. b) Cumulative seismic slips with times since the mainshock for different clusters.

Similar to other moderate to large mainshocks with migrating aftershocks [*Peng and Zhao*, 2009; *Kato and Obara*, 2014; *Tang et al.*, 2014], we also observed a complex expansion of aftershocks with time (Figure 4.9). The complexity in activation of aftershocks could be due to the fact that we simply assign the template location to the best-detected event and a better way to examine the spatio-temporal evolution may be to perform relocations for all the newly detected events. This would require additional

measurements of differential travel times between tens of thousands of template and newly detected events [*e.g., Shelly et al.,* 2013; *Zhang and Wen,* 2015]. Alternatively, this could be a function of the relative roughness of the plate boundary. If the Nicoya margin is controlled by medium-sized velocity-weakening asperities with along-strike heterogeneity, then it is plausible that the aftershocks simply could not expand into regions of the plate interface that are velocity-strengthening, occasionally hosting slow slip events [e.g. *Walter et al.*, 2011; *Walter et al.*, 2013; *Dixon et al.*, 2014].

Further supporting evidence for afterslip driving aftershocks around the epicenter is the identification of repeating aftershock clusters (Figure 4.11). As mentioned before, repeating earthquakes represent velocity-weakening asperities repeatedly ruptured with the recurrence interval determined by the tectonic loading rate, while the surrounding velocity-strengthening region slips aseismically [*Beeler et al.*, 2001; *Matsuzawa et al.*, 2004]. After the mainshock, significant afterslip would change the loading patterns of those asperities and generate repeating aftershocks with rapid reduction of recurrence intervals [*Schaff et al.*, 1998; *Peng et al.*, 2005; *Peng and Ben-Zion*, 2006], which was identified right after the 2012 Nicoya mainshock (Figure 4.12). Most repeating clusters were within the group around the updip edge of the major coseismic patch (Figure 4.11), and occurred much more frequently following the M_w 7.6 mainshock and the M_w 6.4 largest aftershock that occurred one month later (Figure 4.12). We also found the most repeaters occurred along the plate interface (Figure 4.11), consistent with them being driven by afterslip of the same fault plane following the mainshock rupture [*Igarashi et al.*, 2003].

On the other hand, very few repeating clusters occurred within the second group 50 km to the southeast, where the seismicity rate recorded by CRSEIZE project [*Newman et al.*, 2002; *Schwartz and DeShon*, 2007; *Ghosh et al.*, 2008] was characterized as high, though during a time period long before the mainshock. Although fewer stations were in operation near this group (Figure 4.1), at least 5 sites were continuously recording (PNCB, LAFE, ACHA, INDI and POPE) within 50 km of the diffuse seismicity, thus it is likely that these events may be diffuse and not along the slab interface. This group became activated immediately following the mainshock, and showed expansion both along-strike and along dip, similar to the group near the mainshock rupture patch (Figure 4.9). However, no significant afterslip was observed in this region [*Hobbs et al.*, 2017], indicating alternatively mechanisms, such as Coulomb static stress change from the mainshock [*Chaves et al.*, 2017], contribute to the activation and evolution of the SE cluster.

During the afterslip period, the cumulative seismic slip for repeating clusters in the along-trench parallel direction, assuming a constant stress drop of 3MPa, is generally an order of magnitude smaller than observed from geodetic inversion using continuous GPS recordings [*Hobbs et al.*, 2017]. One possibility is that we significantly underestimated the regional stress drop of aftershocks. The used value is equal to what has been found as an average along global subduction zone environments [*Allmann and Shearer*, 2009]. The image is even more complicated when considering a detailed study of earlier microseismicity from *Stankova-Pursley et al*. [2011], which reported apparent stresses (median values ranging from 0.7 to 3.2 MPa in regions below the southern and northern segments of the peninsula) rather than stress drop, and are harder to directly interpret.

While it is generally considered that apparent stress is less than half of the stress drop [e.g. *Savage and Wood*, 1971], its actual relationship is dictated by the seismic efficiency, a parameter that relates radiated to frictional energy released during an earthquake, and is difficult to measure [*Brodsky and Kanamori*, 2004]. Alternatively, for Nicoya, if we used the moment-slip relationship for repeating earthquakes at Parkfield [*Nadeau and Johnson*, 1998], then cumulative slip from repeating earthquakes through the end of 2012 would be in a range similar to afterslip. However, this assumption would result in abnormally high stress drops for small repeating earthquakes (up to 1000 MPa), which is not in general agreement with recent estimates from prior microseismicity [*Stankova-Pursley et al.*, 2011], or from the repeating aftershocks in Nicoya Peninsula [*Bilek et al.*, 2015]. Recent studies suggest that the velocity-weakening asperities responsible for generating repeating earthquakes could also slip aseismically between adjacent events in each repeating cluster [*Beeler et al.*, 2001; *Chen and Lapusta*, 2009], accounting for a large portion of cumulative slip on the asperity [*Chen and Lapusta*, 2009]. If so, this could explain the differences between cumulative seismic slip and geodetically-inferred afterslip. Further analysis of trench-parallel stress drop variations for repeating clusters and the relationship with postseismic slip can better illuminate the relationship.

CHAPTER 5. MICROSEISMICTY BEFORE THE 2008 M_W 7.9 WENCHUAN EARTHQUAKE AND ITS RELATIONSHIP WITH THE ZIPINGPU WATER RESERVOIR

5.1 Introduction

Human activities, such as oil production, reservoir impoundment, are known to induce earthquakes [*Simpson*, 1976; *McGarr et al.*, 2002]. So far the largest magnitudes of confirmed reservoir-induced earthquakes include the 1963 M6.3 Koyna earthquake in Western India [*Gupta*, 2002], and the 1962 M6.1 Xinfengjiang earthquake in South China [*Wei et al.*, 1992]. These events occur in relatively aseismic regions within plate boundaries, and hence the correlation between seismicity rate changes and reservoir impoundment is relatively easy to confirm. On the other hand, it is difficult to confirm reservoir-induced earthquakes in seismically active regions. This is because the background rate is relatively high, and hence the chance of having earthquakes driven by tectonic process rather than reservoir impoundment is also higher than in other aseismic regions.

The May 12th, 2008 Mw7.9 Wenchuan earthquake occurred along the Longmenshan fault (LMSF) that bounds the Tibetan Plateau and the Sichuan Basin. The Zipingpu reservoir was built along the Minjiang river in October 2005, within 10 km of the Wenchuan epicenter. The role of the Zipingpu reservoir in affecting the occurrence of the 2008 Wenchuan mainshock is still under debate [e.g., *Ge et al.*, 2009; *Deng et al.*, 2010; *Lei*, 2011; *Tao et al.*, 2015]. Various studies evaluated the resulting Coulomb stress

changes by considering fluid diffusion process and poroelastic effects. For instance, *Tao et al.* [2015] concluded an increase of ~9.3-69.1 km for Coulomb failure stress at depths above 8 km on the LMSF, while little to no change at depths greater than 12 km. Based on the above calculation, the hypocentral depth of mainshock nucleation is crucial for identifying the potential relationship between the reservoir and Wenchuan mainshock.

Most studies utilizing phase arrivals recorded at stations in regional and teleseismic distances found that the mainshock initiated at a depth of 13 to 19 km [*Hu et al.*, 2008; *Chen et al.*, 2009; *Cui et al., 2011*; *Yang et al.*, 2012, etc.]. In comparison, *Ma et al.* [2011] and *Su and Chen* [2012] utilized seismic data recorded by the local Zipingpu reservoir network that were deployed one year before the reservoir impoundment, and found that the mainshock occurred at a shallower depth of 6-10 km. In addition, while several studies have found that microseismicity in the southwest of Zipingpu reservoir increased clearly following the reservoir impoundment [*Lu et al.*, 2010], it is still not clear whether there is a clear relationship between the microseismicity, the mainshock initiation and the high-angle thrust fault that ruptured during the Wenchuan mainshock.

In this study, we aim to obtain a complete catalog with constrained relative locations, to examine the evolution of background seismicity and its potential relationship with the reservoir impoundment and subsequent water level change, and the Wenchuan mainshock initiation. A semi-automatic waveform-based matched filter technique is applied to detect possible missing events. Moreover, waveform cross-correlation differential travel times with higher accuracy is extracted to help improve relative locations [*Shelly et al.*, 2013, 2016].

5.2 Study Region and Seismic Data

The LMSF straddles between the Tibetan Plateau to the west and Sichuan basin to the East. Prior to the Wenchuan mainshock, most studies suggest relatively low seismic risk in this region, mainly due to the low shortening rate (<3mm/year) across the fault zone [*Chen et al.*, 2000]. Such a low shortening rate is in stark contrast with its most rapid elevation change around the world (i.e., from ~500 m Sichuan basin to ~5000 m Tibetan Plateau within 50-100 km) [*Royden et al.*, 2008]. As reported by China Seismograph Network Center (CSNC), the 2008 M_s 8.0 Wenchuan earthquake (31.0°N, 103.4°E, focal depth: 15 km) struck the Yingxiu town of Wenchuan country within Sichuan Province of China at 14:28 pm local time (Beijing Time) on May 12nd, 2008 (2008-05-12 06:28:01 UTC). Many studies with different types of observations concluded that the mainshock started at the southern part of the Beichuan fault and ruptured ~300 km in the northeast direction [*Hao et al.*, 2009; *Xu et al.*, 2009; *Tong et al.*, 2010], followed by numerous aftershocks [*Huang et al.*, 2008; *Zheng et al.*, 2009] and triggered landslides [*Yin et al.*, 2009; *Li et al.*, 2014]. In addition, the frontal Pengguan fault ruptured co-seismically for ~80 km [*Xu et al.*, 2009].

The Zipingpu reservoir was built in the late 2004, within ~10 km relative to the mainshock epicenter. As required, a temporary seismic network was deployed around the reservoir one year before to monitor the earthquake activities. This network contains 7 short-period stations (Figure 5.1) recording continuously at 100Hz sampling rate from September 2003. Together with one nearby broadband permanent station (YZP), we process continuous seismic data of above 8 stations from October 2004 to December 2007 (Figure 5.2).

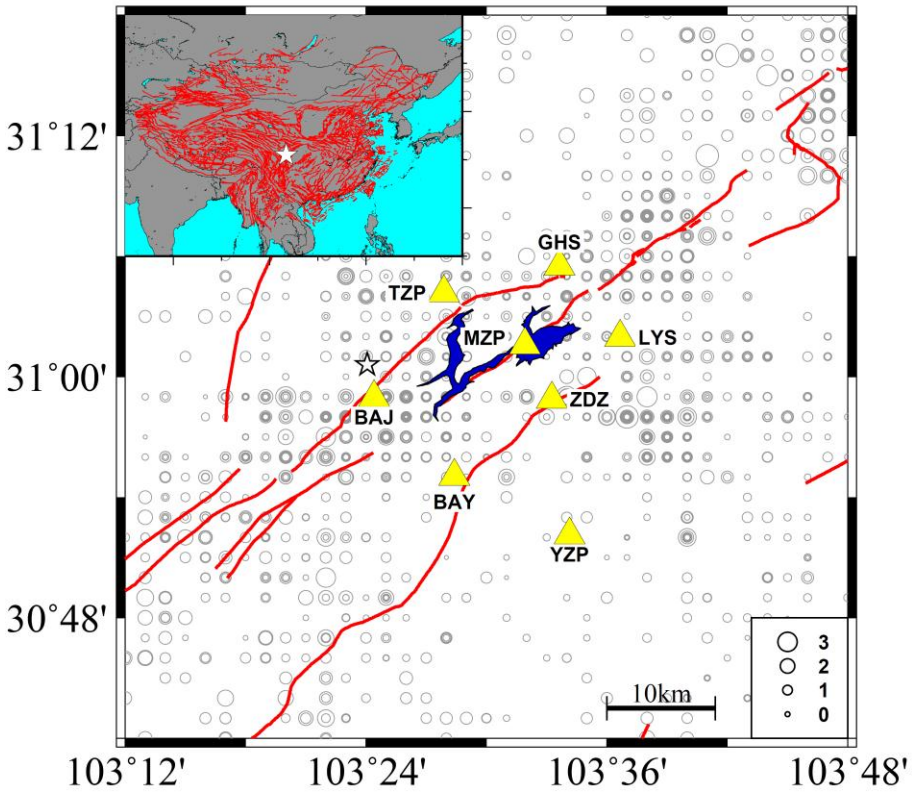

Figure 5.1 Map of the study region. Yellow triangles and open gray circles show seismic stations and initial catalog events (mainshock as the white star) used in this study. Red solid lines mark active faults. The blue shaded area indicates the water reservoir. Insert shows the Wenchuan mainshock in bigger tectonic context.

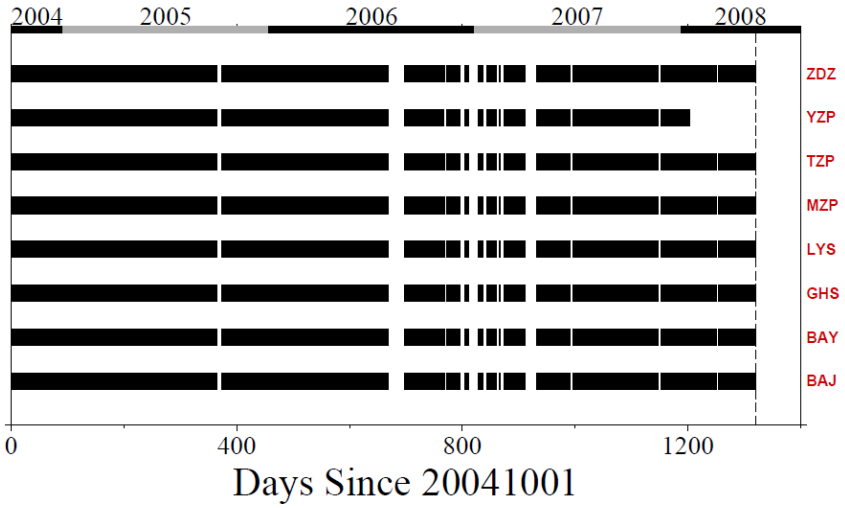

Figure 5.2 Data availability for all used stations since October 2004.

5.3 Analysis

5.3.1 *Absolute locations from Hypoinverse*

The Sichuan Earthquake Administration (SEA) routinely picked phase arrivals and built a local earthquake catalog with ~2,630 events from 09/01/2004 to 05/12/2008 using this reservoir network and nearby permanent stations. We cut the event-based waveform based on this catalog, and manually repick P and S arrivals to avoid possible wrong/missing phases. Figure 5.3 shows the waveform and newly picked phase arrivals for a M_L 1.4 event.

Since this initial catalog roughly assigned a constant value of 3.0 km for the hypocentral depths, our first step is to obtain the absolute locations with better depth information for these catalog events. We input the manually adjusted phase picks into the Hypoinverse program [*Klein*, 2002], and locate events with a local 1D velocity model [*Lu et al.*, 2010]. In order locate an earthquake with relatively smaller errors, we require phase arrivals from a minimum number of 4 stations.

5.3.2 *Matched filter detection*

The event detection generally follows our previous analysis procedure [*Meng et al.*, 2013] and is briefly summarized here. We use a 10s long window starting from 1s before P wave on all components as the signal window to run sliding-window cross-correlations with corresponding continuous traces. The resulting cross-correlation functions (CCFs) at all station-channels are shifted back to the template's origin time. To avoid noisy template traces, only those with signal-to-noise ratios (SNRs) above 5.0 are

kept. The SNR is defined as the ratio between the energy within the 10s signal window and the noise window, which is a 10s long widow ending 1s before P wave. We select a catalog event as a template with at least 9 kept traces (i.e., equivalent to 3 components at 3 stations). To save computation time, we also down-sample the initial waveform from 100 Hz sampling rate to 20 Hz and utilize a GPU card to run the sliding window cross-correlation [*Meng et al.*, 2012].

After obtaining all CCFs, a mean CC trace is obtained by stacking them directly. A positive detection is registered once the mean CC value above a pre-defined cutoff value, which is the median value of the daily stacked trace plus 15 times its median absolute deviation (MAD). The magnitude of the newly detected event is based on the median peak amplitude ratio relative to its best-matched templates across all channels.

5.3.3 *Earthquake relative location*

To obtain the waveform cross-correlated differential travel time with higher accuracy, we recut the raw waveform at 100 Hz sampling rate for all events in the detected catalog. A 1-15 Hz bandpass filter is applied to the recut waveform. For every newly detect event, we first assign the location of its best-matched template as its starting location. The initial phase arrivals for the detected events are directly taken from those for the templates.

Next we compute differential travel times at each station for all possible event pairs (including both template and newly detected events). Similar to the *ph2dt* program in HypoDD, we pre-select event pairs with spatial offset less than 20 km, given the potential large starting location uncertainty. The *P* or *S* wave cross-correlation differential time

dtime for selected pairs is computed using a 1.5 s window starting 0.50 s before the *P* and *S* phase picks, and saved only when the cross-correlation coefficient (CCC) is above 0.6 for *P* wave or 0.5 for S wave. After obtaining the *dtimes* across all stations, we further select event pairs with at least 6 saved observations. The final output is then used as input in the HypoDD program [*Waldhauser and Ellsworth*, 2000] to provide better constraints on relative locations.

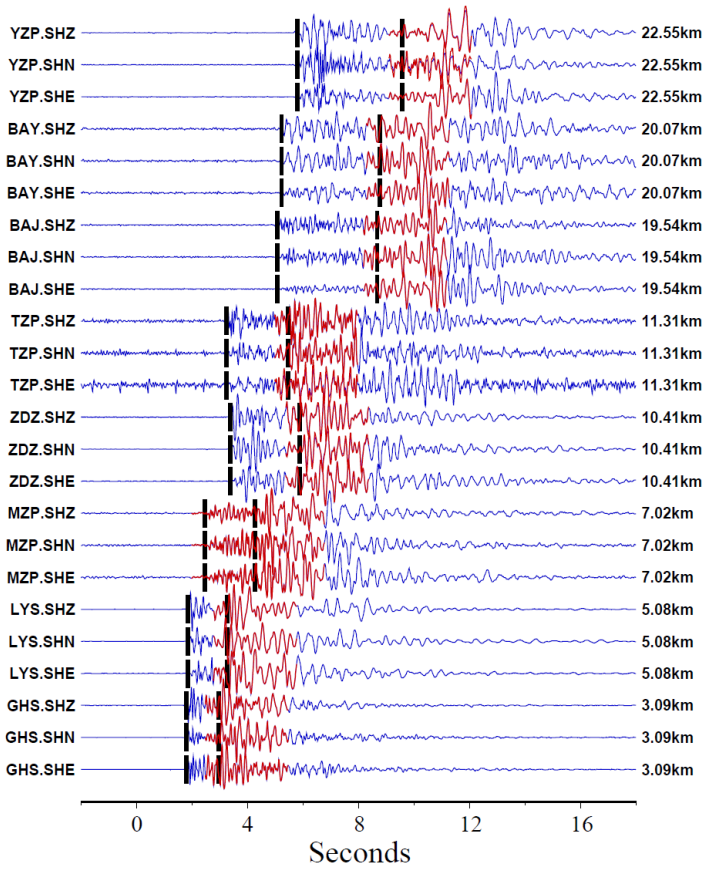

Figure 5.3 Example waveform for a M_L 1.4 event (origin time: 2004/10/15 16:35:14.62). STA.CHAN and epicentral distance are labeled on both sides. Vertical black bars show the reexamined phases, while catalog phases are shown with red.

5.4 Results

5.4.1 *Absolute locations*

Using the manually re-examined phase picks for ~2,630 catalog events, the Hypoinverse program returns the locations of ~2,410 events (Figure 5.4a). We find three major earthquake clusters around the Zipingpu reservoir: one to the southwest of the reservoir near Wenchuan epicenter (Box A in Figure 5.4a), one to the northeast along the LMSF (Box B), as well as another one near the Dujiangyan ancient irrigation system (Box C, [*Ruan et al.*, 2017]). To evaluate the resulting depth profile, we also examine the cross-sections along both strike-parallel and strike-normal directions (Figure 5.4b, c, & d). The majority of the catalog events occurred in the shallow depth above 10km. Events within Box A (Figure 5.4c) outline a high-angle dipping plane across the LMSF. On the other hand, two major isolated clusters are found within the northeast cluster (Figure 5.4b), likely associated with mining sites in this region [*Ruan et al.*, 2017]. We also find that the swarm sequence (with a M_L 3.7 mainshock) occurred near Dujiangyan starting from 2008/02/14 21:34pm generally outlines a nearly horizontal plane (Figure 5.4d), which is consistent with the finding in *Ruan et al.* [2017].

5.4.2 *Event detection and relocation result*

Using ~1,675 selected templates with at least 9 SNR>5 traces, we end up detecting ~7,700 new events above 15MAD (Figure 5.5). To visualize the seismicity evolution with time, we plot the monthly seismicity rate and water level changes in Figure 5.6 for major earthquake clusters in section 5.4.1 (Figure 5.4). A similar plot for magnitude vs. time for each box is shown in Figure 5.7.

Combing with the catalog events, we compute the waveform cross-correlation *dtimes* for all ~10,320 (7689 + 2632) events. After selecting event pairs with at least 6

observations (an example selected event pair is shown in Figure 5.8), we obtain a total number of ~504,100 P and ~52,7200 S cross-correlation *dtimes* for a total number of 7,409 events. The final catalog after many iterations contains 7,101 events with stable improved relative locations. Same with Figure 5.4, all relocated events are shown in Figure 5.9, with sub-panels separating seismicity before and after the first impoundment in October 2005.

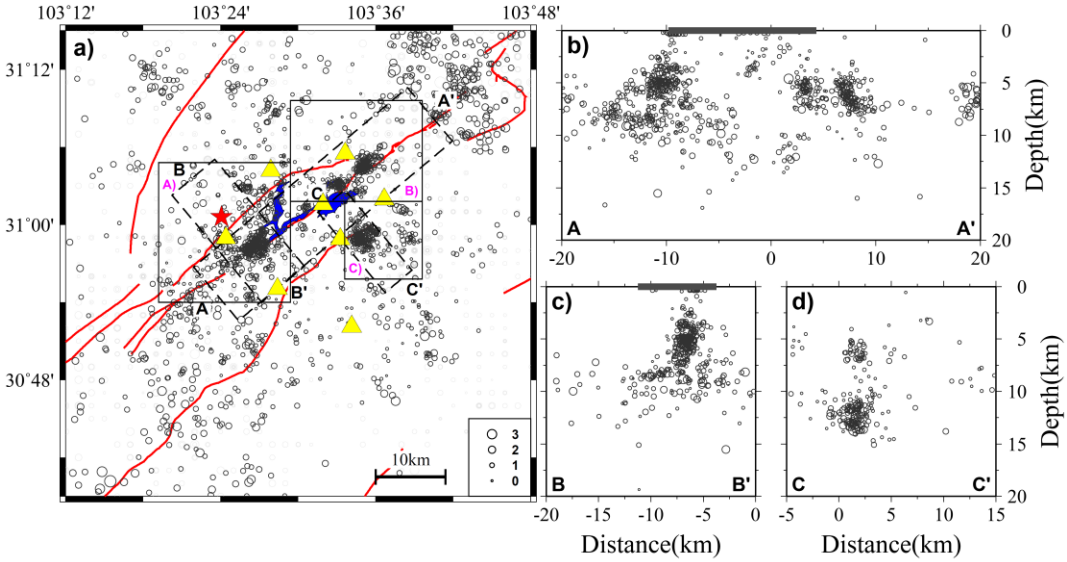

Figure 5.4 Location result using the Hypoinverse software. a) Map view of the catalog events. Yellow triangles, red solid curves, and blue shaded area mark used stations, active faults and water reservoir. Cross-sections, including strike-parallel direction along AA', strike-normal direction along BB' containing the southwest cluster, CC' containing the cluster near Dujiangyan. b), c), d) depth profiles for three cross-sections. Black rectangles mark three clusters shown in Figure 5.6.

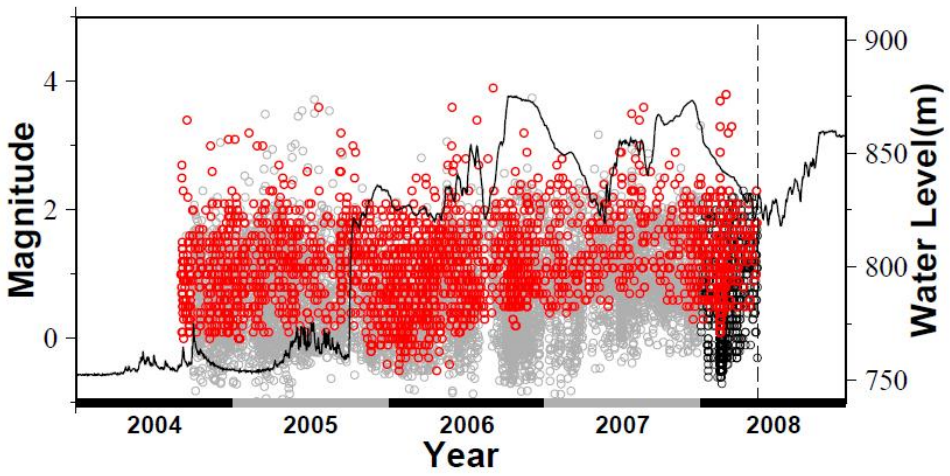

Figure 5.5 Magnitude vs. time for events in detected catalog, together with the water level. Gray circles are newly detected events above 15MAD, while red circles show catalog events. Black circles are detected events from *Ruan et al.* [2017].

5.5 Discussion and Future Work

5.5.1 *Depth of the initiation event*

We manually examine the waveforms in the first 100s of the Wenchuan mainshock recorded by the reservoir network and nearby permanent stations. Even all of them show clipped waveforms seconds after the first arrivals, the P arrivals of the initiation event can be accurately picked (Figure 5.10). The constrained new hypocentral depth using these manually picked arrivals from NLLOC (http://alomax.free.fr/nlloc/) is ~7.5km, similar to previous studies [*Ma et al.*, 2011; *Zhang et al.*, 2013, etc.]. An increase of ~10 kPa for Coulomb failure stress is expected [*Tao et al.*, 2015], indicating a potential link between the water impoundment and mainshock nucleation.

To further verify the relationship between the reservoir impoundment, active faulting and mainshock nucleation, we plan to accurately identify the first motion direction (up or down) for the initiation event recorded by all available stations within

150km and obtain its fault plane solution using the FPFIT package [*Reasenberg and Oppenheimer*, 1985]. This could help us to evaluate the focal mechanism of the initiation event. Moreover, by comparing its phase moveout with nearby smaller earthquakes, we could further constrain the depth of the initiation event.

5.5.2 *Water level change and seismicity rate*

The monthly seismicity rate shows an obvious increase within the cluster to the southwest of the reservoir after the first water impoundment (Figure 5.6 and Figure 5.7b & c), and the seismicity shows high-angle dipping features. These might correspond to active faults, similar to those outlines in *Lei and Zhao* [2009] with more refined structures. The cluster to the northeast was active before the initial impoundment (Figure 5.6), while the cluster near Dujiangyan experienced an earthquake sequence in Feb 2008 (Figure 5.6). Because of their timings, both of them are unlikely directly linked to the water reservoir.

To further quantify the relationship between water level change and seismicity rate, we plan to compute the β-value map around the first water impoundment to show the significance of either seismicity rate increase or decrease. Moreover, we would obtain a time-varying *b* value map in this region to see the temporal evolution, and its link to the water level change. In addition, we want to further monitor the seismicity evolution in the early aftershock period, by conducting a similar event detection and relocation analysis, to obtain the full picture on how the critically stressed complex faulting system releases the strain, and its exact relationship to the reservoir loading/discharge and the fault ruptured during the mainshock.

5.5.3 *Dependence on the velocity model*

When comparing with location results from *Lu et al.* [2010] or *Ruan et al.* [2017], we note that the whole cluster near Dujiangyan (Box C in Figure 5.4) is shifted to the west. One potential cause is we utilized a single 1D velocity model to locate this cluster, which locates within the Sichuan basin with relatively lower seismic velocity, while most stations are located to the faster side. Alternatively, we can use different velocity models across the LMSF, or simply incorporate refined 3D velocity models.

5.6 Summary

We obtain a new catalog between October 2004 and December 2007 around the 2008 Mw 7.9 Wenchuan mainshock, by detecting and relocating event with the matched filter technique. The new catalog outlines three major earthquake clusters: the cluster to the southwest of the reservoir occurred along the dipping faults, and experienced an obvious increase of seismicity after the initial impoundment of the reservoir in October 2005, while another two clusters to the northeast of the reservoir and Dujiangyan seem to be irrelevant to the reservoir. Moreover, the preliminary results resolving the depth of the initiation event for the mainshock shows that the mainshock may start at a depth shallower than 10km, which may favour the hypothesis that the water reservoir indeed advances the occurrence of the Wenchuan mainshock. Additional analysis, including refine relocation using more accurate velocity models, careful determination of the initiation event depth and its focal mechanism, would be done further to understand the relationship between the reservoir and mainshock.

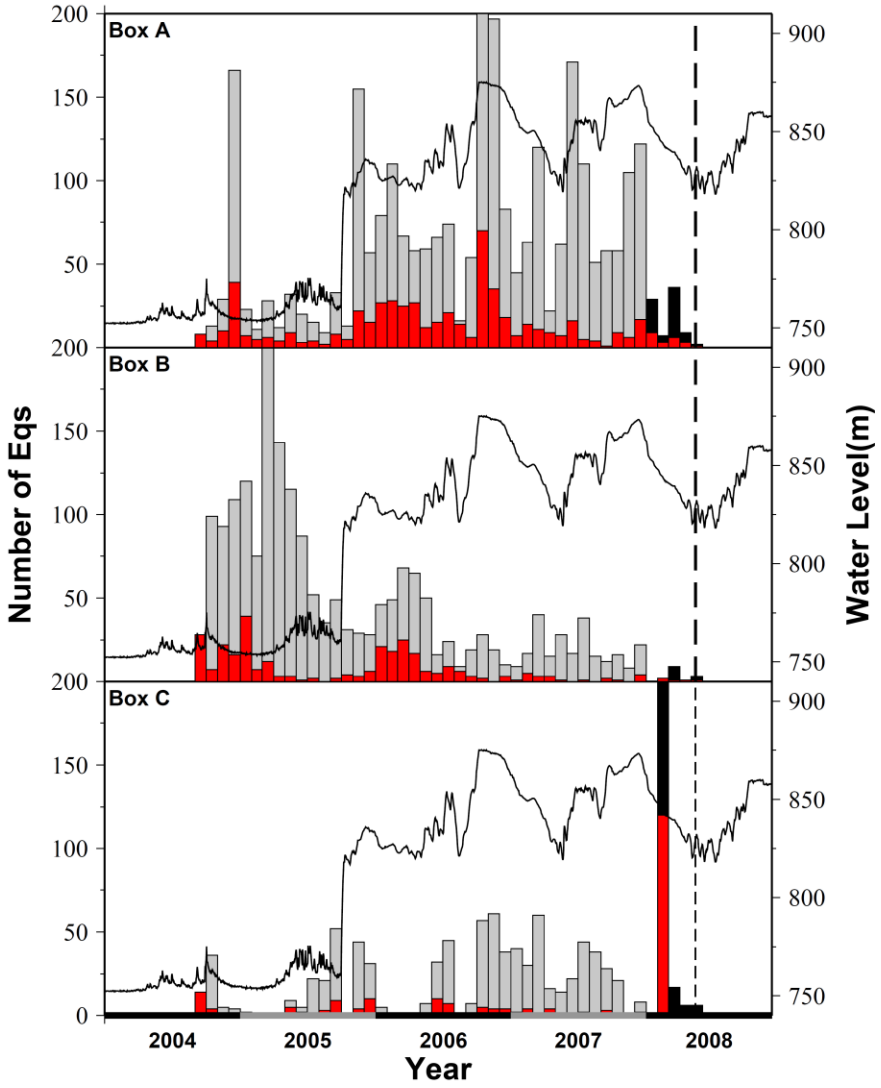

Figure 5.6 Monthly seismicity rate (vertical bars) vs. time for three earthquake clusters (Box A, Box B, Box C in Figure 5.4). Symbols are same to those described in Figure 5.5.

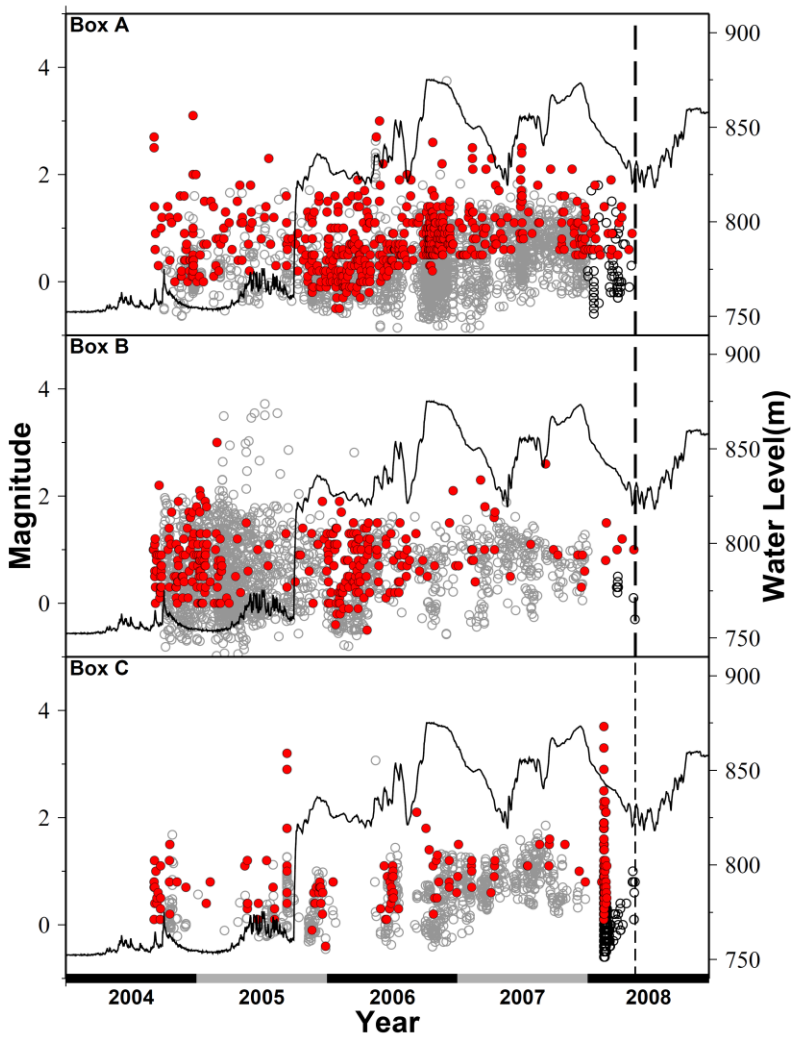

Figure 5.7 Magnitude vs. time for three earthquake clusters (Box A, Box B, Box C in Figure 5.4). Symbols are the same with those described in Figure 5.6.

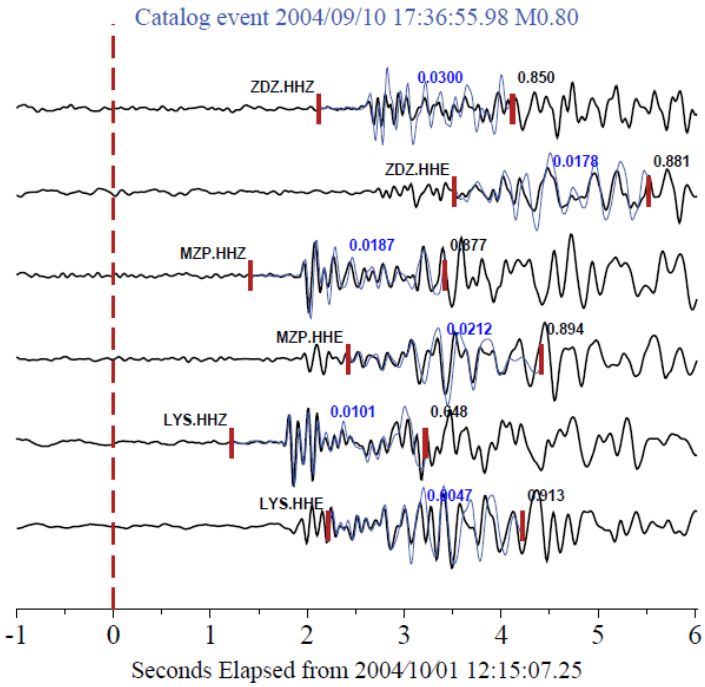

Figure 5.8 An example demonstrating computing the cross-correlation differential travel times for a selected event pair (6 observations).

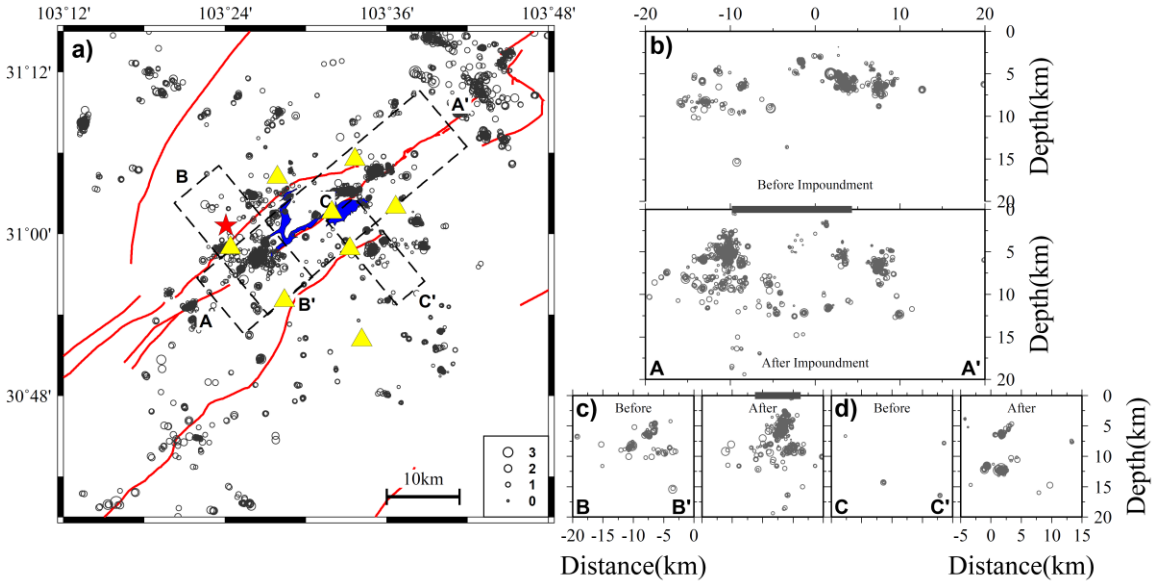

Figure 5.9 Relocated locations for detected catalog. a) Map view for all events. b) depth distribution for events along the strike-parallel AA' direction. Events before and after the first impoundment are shown in top and bottom sub-panels. c) and d) show two strike-normal cross sections along BB' and CC', with left and right sub-panels showing distribution before and after the first impoundment.

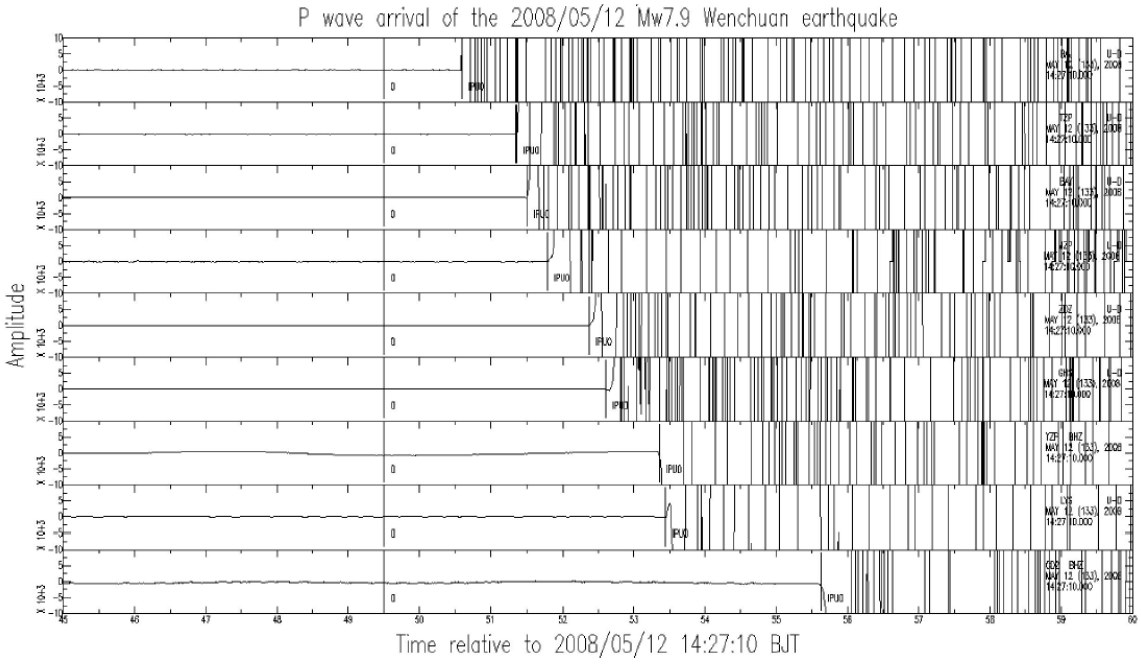

Figure 5.10 Manually picked P arrivals for nearby stations

CHAPTER 6. DETECTING AND RELOCATING THE FORESHOCK SEQUENCE PRECEDING THE 2010 M_W 7.2 EL MAYOR-CUCAPAH EARTHQUAKE

6.1 Introduction

Earthquakes do not occur individually. Instead they cluster in space and time, forming different types of earthquake sequences [e.g., *Mogi*, 1962]. Large shallow earthquakes are generally followed by numerous aftershocks, obeying the Omori's decay law [e.g., *Omori*, 1894; *Utsu et al.*, 1995]. On the other hand, some large earthquakes are preceded by increased seismic activity called 'foreshocks' [*Jones and Molnar*, 1979; *Abercrombie and Mori*, 1996; *Dodge et al.*, 1996; *McGuire et al.*, 2005; *Kato et al.*, 2012].

The exact relationship between foreshocks and mainshock nucleation is still under debate [e.g., *Mignan*, 2014]. In the so-called 'nucleation model' or 'loading model', foreshocks are driven by aseismic slip as part of a nucleation process that ultimately initiated the mainshock rupture [*Dodge et al.*, 1996; *McGuire et al.*, 2005; *Bouchon et al.*, 2011; *Kato et al.*, 2012; *Kato and Nakagawa*, 2014; *Tape et al.*, 2018], which has been long observed/predicted by laboratory and numerical modeling studies [e.g., *Dieterich*, 1979; *Ohnaka*, 1992]. An alternative 'cascading model' or 'triggering model' states that earthquakes always trigger each other, and the mainshock could be considered as triggered by the foreshocks that happened to have a larger size [*Helmstetter et al.*, 2003;

Felzer et al., 2004; *Ellsworth and Bulut*, 2018]. In this case, we would not expect to observe any fundamental difference between a foreshock and aftershock sequence.

One major difficulty to differentiate between these models is that the magnitude of completeness (M_c) for most foreshock sequences is relatively high (>3.0) for global catalogs. Hence, the underlying spatio-temporal evolutions are not well identified when the local microseismicity is not adequately detected.

In this study, I conduct a systematic analysis of foreshocks associated with the 2010 M_w 7.2 El Mayor-Cucapah earthquake in Baja California, Mexico to better understand the physical mechanisms of foreshock generation. This sequence was chosen for the following reasons: a foreshock sequence preceding the mainshock and locating within 2-3 km relative to the mainshock was reported [*Hauksson et al.*, 2011]. This sequence was located only using stations from Southern California Seismic Network (SCSN), which are relatively far away from (>40km) the foreshock sequence. Some stations from the Red Sísmica del Noroeste de México (RESNOM) network are much closer, but they were recorded in the triggered mode (i.e., only those above certain amplitude threshold are recorded). In this case, we suspect that many small foreshocks would be missing from the reported catalog [*Hauksson et al.*, 2011]. Similar to *Wu et al.* [2014], applying the template matching to seismic data recorded in triggered mode could result in more events than listed in the SCSN catalog.

6.2 Study Region

The 2010 M_w 7.2 El Mayor-Cucapah earthquake ruptured the Mexican Pacific margin in northern Baja California, which straddles the plate boundary between North

American and Pacific plates with high seismicity rate. Many foreshocks within a few kilometers of the mainshock epicenter were recorded by stations primarily in Southern California, starting about 19 days before the mainshock [*Hauksson et al.*, 2011]. The magnitudes of the foreshocks range from 1.3 to 4.3, and the sequence contains several clusters, with two major episodes on March 21-22 and on April 3-4, 2 days preceding the mainshock.

6.3 Analysis Procedures

We performed a systematic detection and relocation of foreshocks starting 21 days before and up to the mainshock. Specially, we downloaded continuous waveforms from all SCSN stations within 150 km of the mainshock epicenter (Figure 6.1b). Next, we applied a 2-16 Hz band-pass filter to the data, and cut waveforms for 76 foreshocks (Figure 6.1c, within 10km from the mainshock epicenter, and from 03/15/2010 up to the mainshock) that were listed in either the relocated SCSN catalog [*Hauksson et al.*, 2012] or RESNOM catalog. To reduce the computational cost, we also down-sample the data from 100/s to 50/s. Then, we utilized a 6 s template window (1 s before and 5 s after the P or S arrival on vertical/horizontal component, respectively), and computed the waveform cross-correlation (CC) functions for all possible station-component pairs. We further shifted the resulting CC functions back to the origin time of template events, and stacked together to enhance true signals. As was done before [*Meng and Peng*, 2014], only time points with corresponding mean CC values greater than the median CC value of the daily trace plus 12 times its median absolute deviation (MAD) were considered as positive detections. We finally combined detection from different template event together, and kept those detections with highest CC value every 3 s [*Peng and Zhao*, 2009]. We also

estimated the magnitude of the newly detected events based on the median amplitude ration between the detected event and its best-matched template event [*Peng and Zhao,* 2009].

Next we searched in the RESNOM waveform database, and extracted waveforms from trigger-mode stations (Figure 6.1b; Figure 6.2). We combined those two networks by merging existing waveforms: waveforms were re-cut for SCSN stations, and put together with event-based waveforms for RESNOM stations if exists. Next, we manually picked the P/S arrivals for the aforementioned 76 catalog events, and assign the phase picks/locations to their associated detections. We then obtain cross-correlated differential time by cross-correlating all possible event pairs (2.5s window for P and 4.0s for S waves, starting 0.25s before the phase arrivals). Finally, we utilized HypoDD [*Waldhauser and Ellsworth,* 2000] to relocate them using cross-correlation differential times.

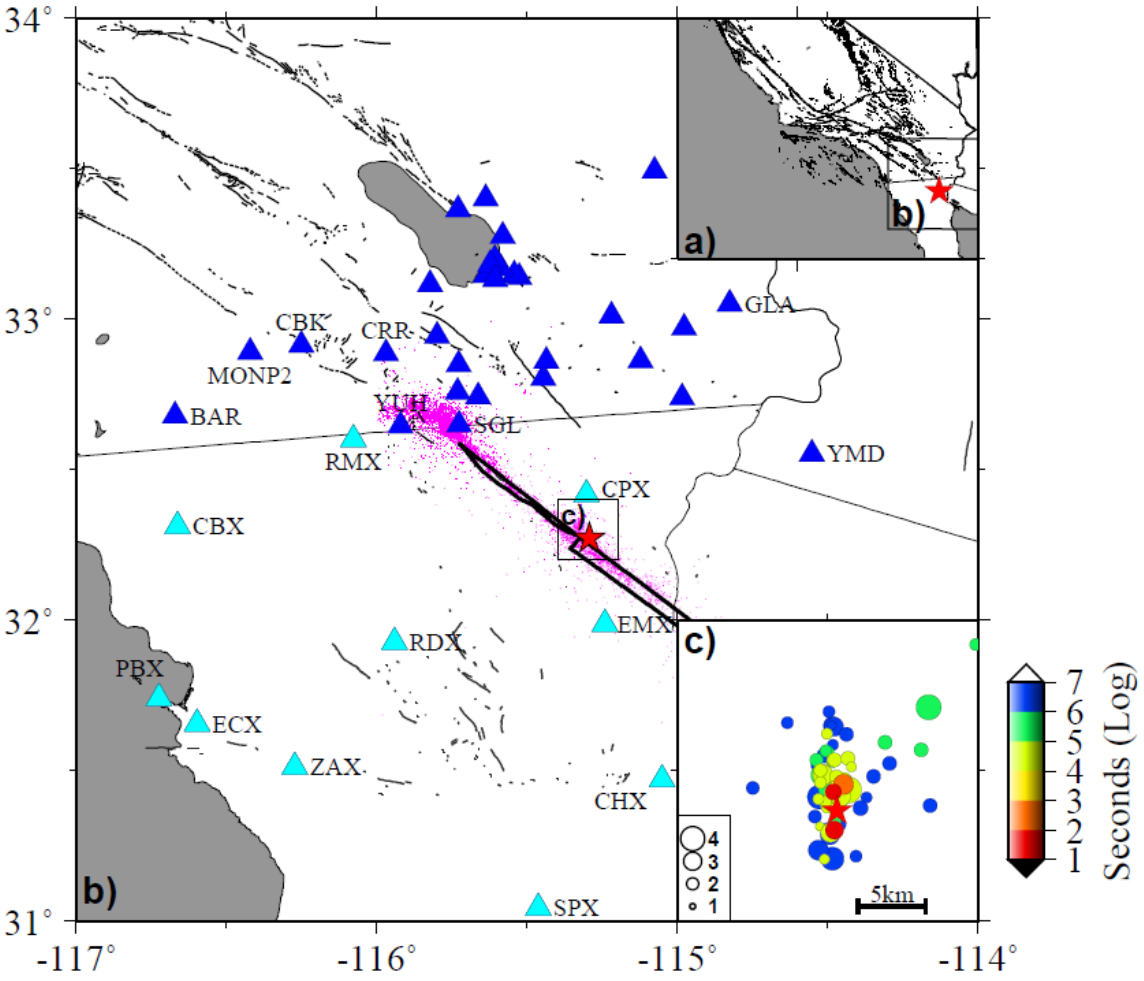

Figure 6.1 Map of the study region. a) Insert shows the bigger tectonic context, with the 2010 El Mayor-Cucapah mainshock as the red star. b) Map shows used stations. Stations in SCSN are shown with blue triangles, while cyan triangles mark RESNOM stations. Solid red line indicates the surface rupture of the mainshock [*Wei et al.*, 2011], with aftershocks shown with pink dots [*Hauksson et al.*, 2012]. c) A small region around the mainshock epicenter. Foreshocks prior to the mainshock are color-coded with time relative to the mainshock.

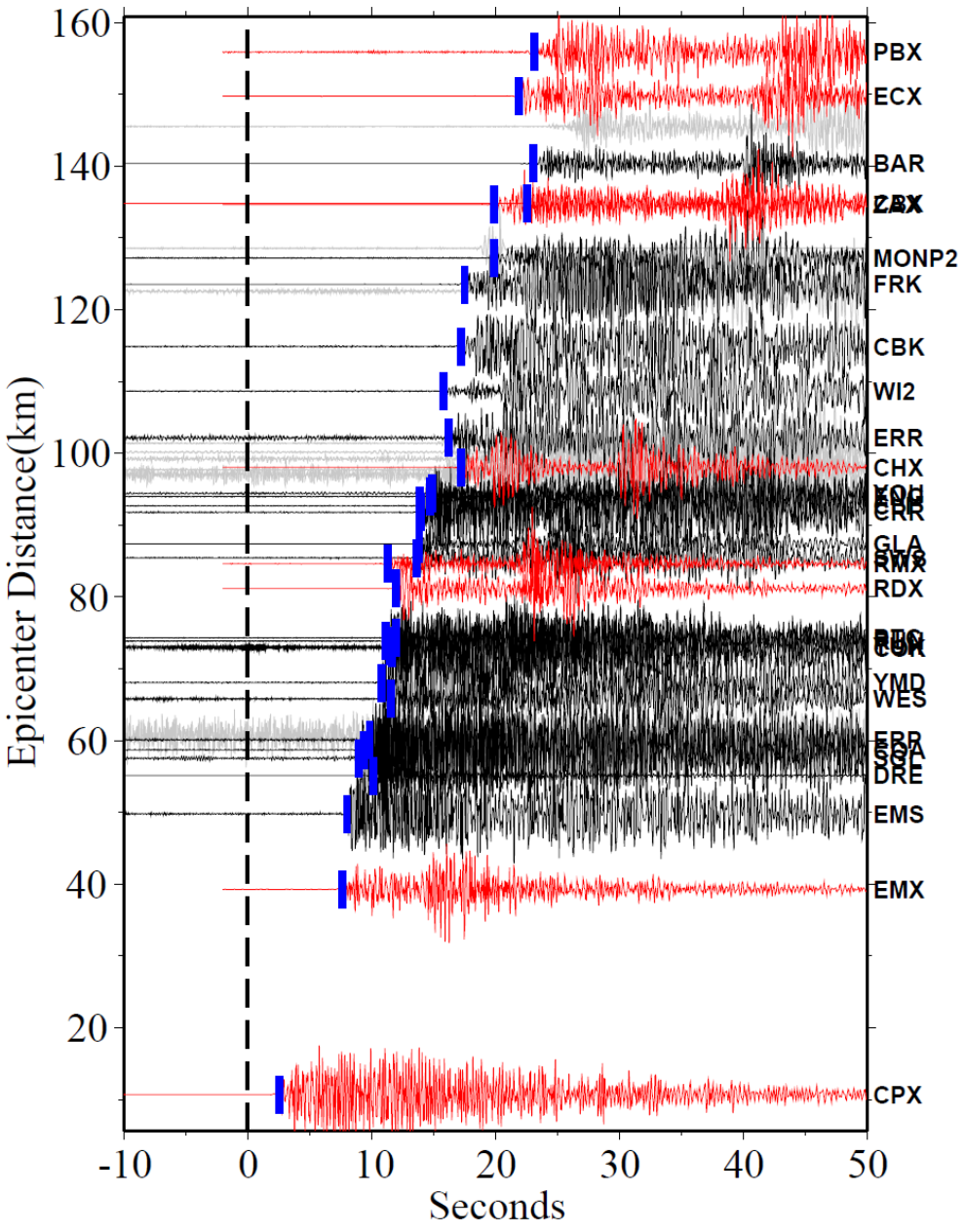

Figure 6.2 Combined phase picks from both SCSN (black) and RESNOM (red) stations. Blue vertical bars show manually picked phases (used for relocation).

6.4 Results

6.4.1 *Earthquake detection and relocation result*

Figure 6.3a shows the magnitude versus time for all 541 events in the detected catalog. We separate the foreshocks into two major sequences: one sequence starting 21 days to 2 days before the mainshock, and another within the last 2 days prior to the mainshock (Figure 6.3b). After selecting event pairs with at least 4 waveform cross-correlated differential times *dtimes*, we obtain ~48,00 P and ~49,00 S dtimes, including 323 events, and ~300 of them have with well-constrained relative locations. Events within the above two sequences after the relocation show more diffusive pattern in the first sequence (Figure 6.4a&c), while the one immediately preceding the mainshock occurs within a relatively more refined region (Figure 6.4b&d). The seismicity generally outlines a North-South striking plane, which is consistent with the focal mechanisms of large foreshocks [*Hauksson et al.*, 2011].

To illustrate the potential migration pattern of foreshocks, we measure the distances relative to the mainshock epicenter and plot out distance vs. time for detected foreshocks as well as early aftershocks. As shown in Figure 6.5b, foreshocks occur within a banded area (with a width of about 10km) and collapse to the mainshock within last 2 days prior to the mainshock.

6.4.2 *Earthquake statistics and ETAS fitting*

We apply the best-combined method [*Wiemer*, 2000] to compute the magnitude of completeness (M_c) of the foreshock sequence (Figure 6.6). The resulting M_c=0.9 is then used to select events within the foreshock sequence. To investigate the statistical behavior of the sequence, we fit the first sequence (starting from 16 days to 2 days before the mainshock) using the ETAS model [*Ogata*, 1988, 2006], and predict the second

sequence (within last 2 days before the mainshock) using the best-fitted parameters (Figure 6.7).

6.5 Discussion and Future Work

Using the matched filter technique, we detect 465 more foreshocks, which is about 6 times more than listed in the standard catalog. Among all events in the detected catalog, we obtain ~300 events with constrained relative locations. This more complete catalogue enables us to monitor the spatio-temporal evolution of foreshocks and provides us new insights in mainshock nucleation.

Chen and Shearer [2013] concluded that the foreshock sequence within last 2 days preceding the El Mayor-Cucapah mainshock exhibits a swarm-like behaviour and have lower average stress drops. Similarly, our ETAS fitting result underestimates the sequence (Figure 6.7b and Figure 6.7d) using best-fitted parameters of the more likely mainshock-aftershock sequence earlier, which also supports the conclusion that this sequence behaves more likely a continuous swarm. Rather than showing migration along preferred directions [*Kato et al.*, 2012], the swarm seems to collapse into the mainshock epicentre, with later events closer to mainshock (Figure 6.4d and Figure 6.5b).

Since only ~10 foreshock events were analysed in *Chen and Shearer* [2013], we plan to conduct additional analysis to estimate stress drops for the newly detected catalog. This could potentially offer a more complete picture of the stress drop evolution within our study window. Moreover, the ETAS fitting result strongly depends on the pre-defined parameters. To avoid potential bias of using improper parameters, we could also fit the early aftershock sequence and utilize those corresponding parameters.

So far we run the event detection only using continuous data recorded by SCSN stations, with epicentral distances ranging from 40 to 150 km. One additional work is to utilize the available segmented data recorded by the local triggered-mode stations, which are geographically closer and have better azimuthal coverage (Figure 6.1). This could help to further detect more missing smaller events. In addition, due to the large velocity contrast between the shallow sediments across the Gulf of California and crustal rocks, using velocity models with shallow sedimentary layers could improve the robustness of locations.

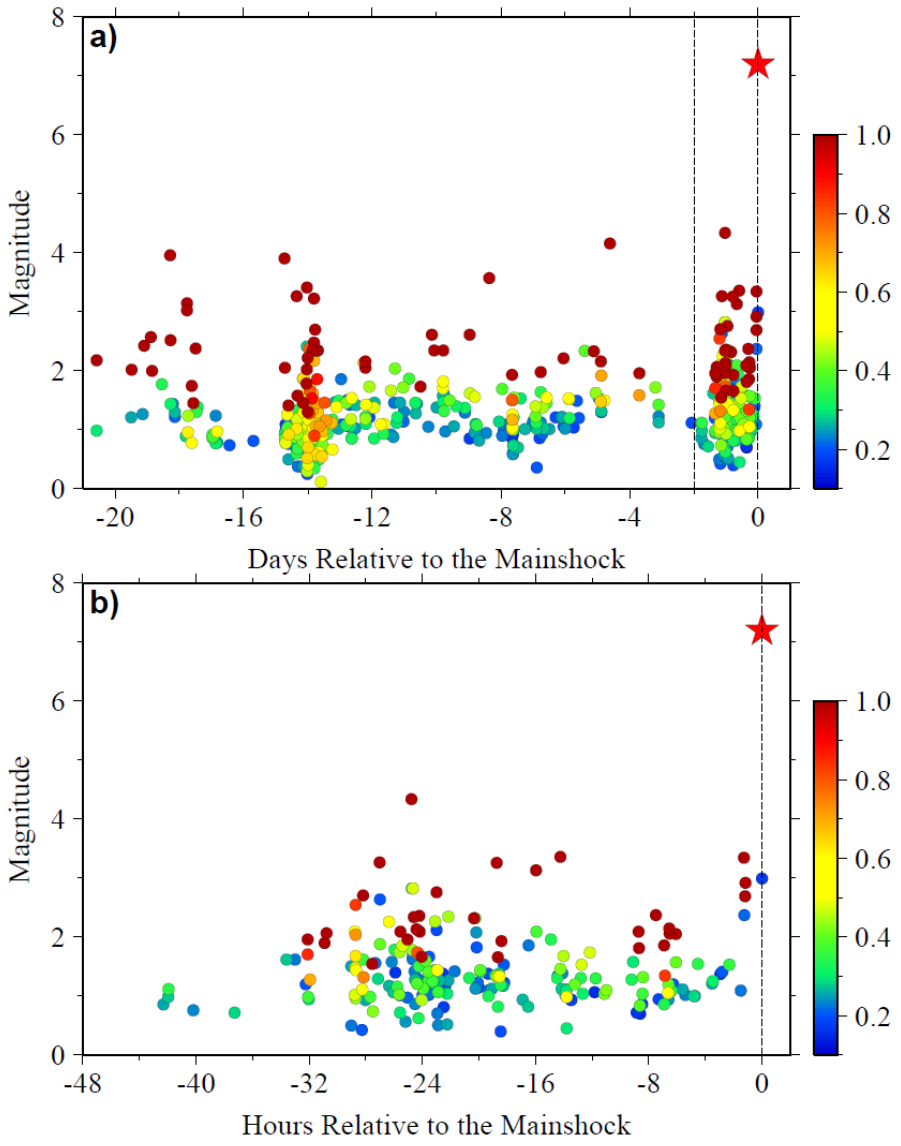

Figure 6.3 Magnitude vs. time for all detection events. a) Detection result starting 21 days before the mainshock. b) The detected events within 2 days prior to the mainshock. Events are color-coded with the mean cross-correlation values.

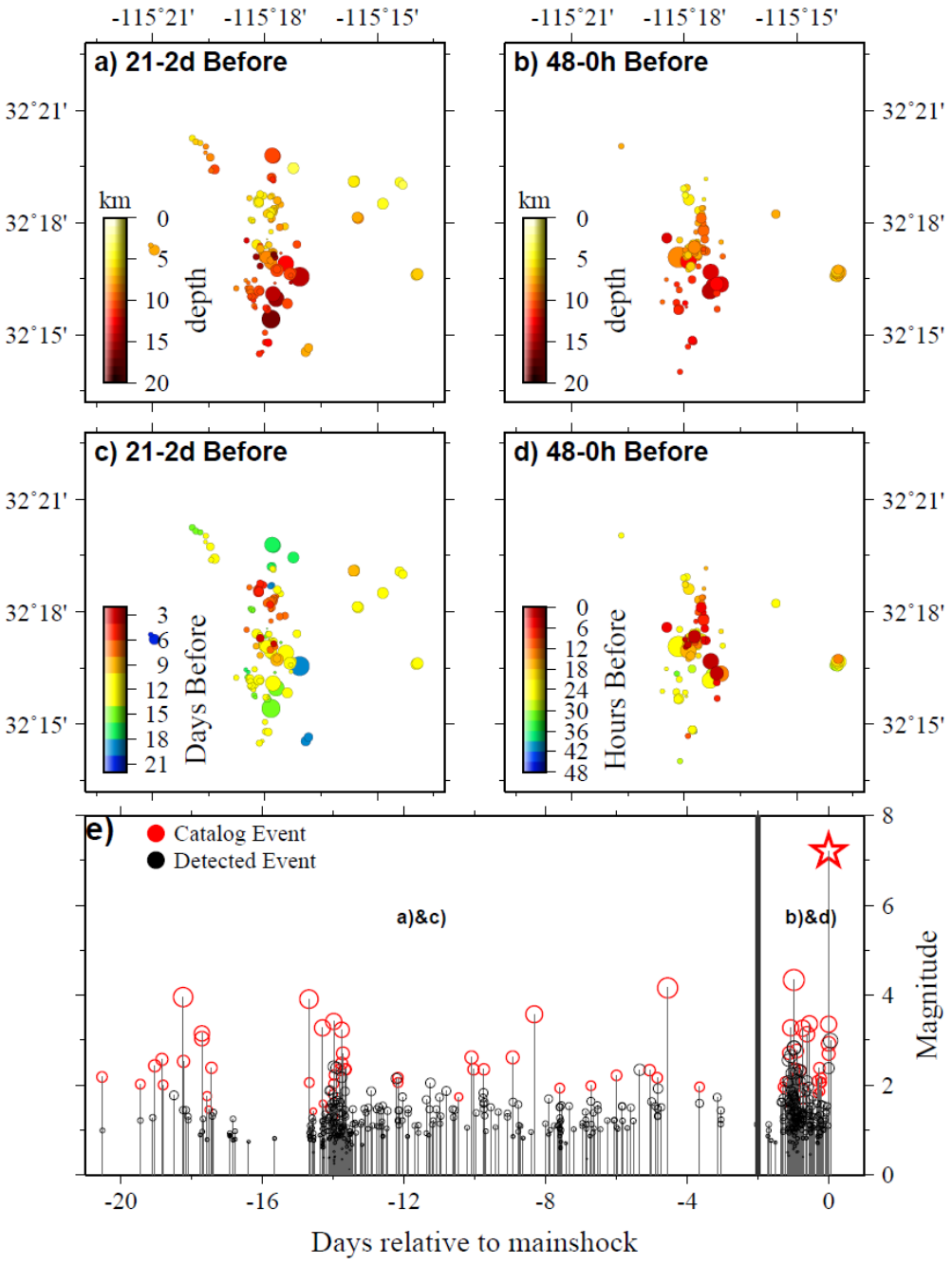

Figure 6.4 Spatial distribution of detected events. a) and c) show the foreshock activity starting from 21 days to 2 days before the mainshock color-coded with depth and time relative to mainshock, respectively. b) and d) show similar plot for the swarm starting 2 days before up to the mainshock. e) magnitude vs. time for the new detected catalog.

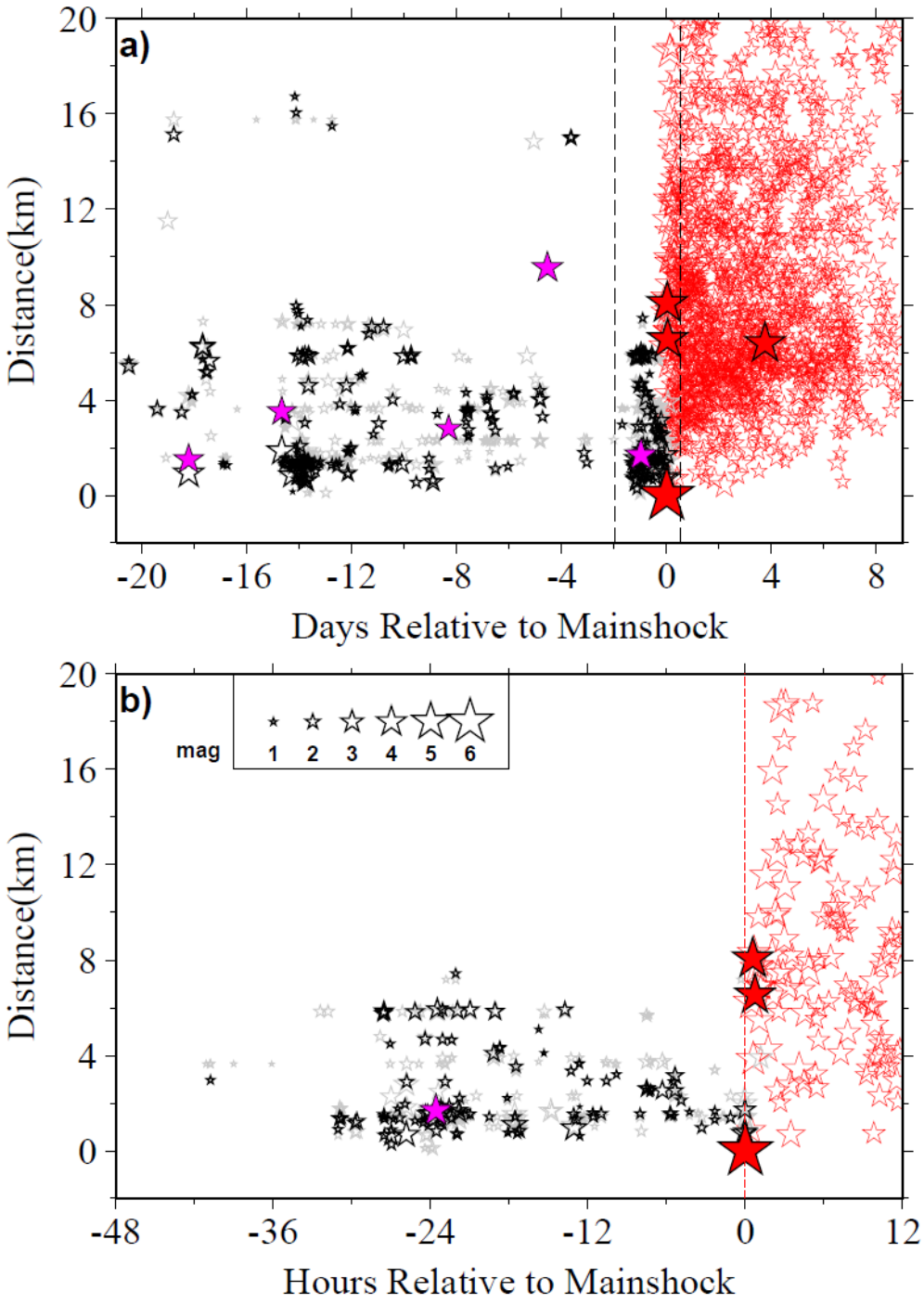

Figure 6.5 Distance relative to the mainshock vs. time for seismicity before and after the 2010 mainshock. a) 21 days before and 9 days after the mainshock. Gray stars show all detected events, while relocated ones are shown with black stars. Pink stars show foreshocks with magnitudes above 3.5, while filled red stars are mainshock and *M*>5 aftershocks. b) similar to a) around the zoomed-in window (48 hours before and 12 hours after).

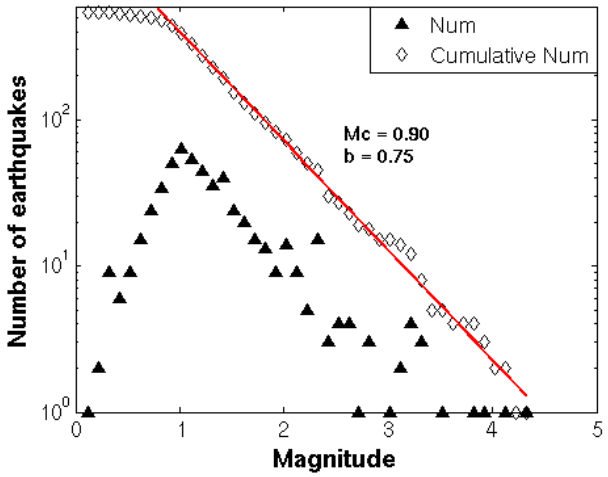

Figure 6.6 Frequency-magnitude distribution of the detected catalog

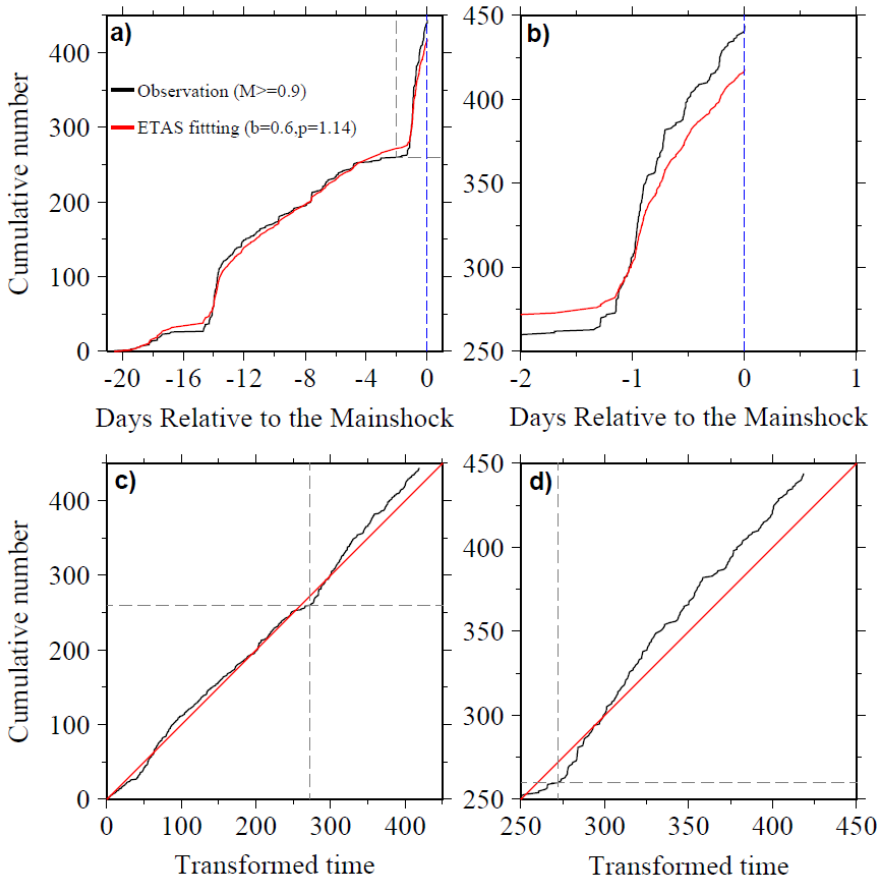

Figure 6.7 Observation and ETAS fitting of the foreshock sequence. The best fitted parameters are based on the earthquake sequence starting ~15 days to ~2 days before the mainshock.

CHAPTER 7. SYSTEMATIC SEARCH FOR REPEATING EVENTS ALONG THE CENTRAL SAN JACINTO FAULT

7.1 Introduction

A remaining challenging question is how to combine the seismic observations with other types of observations, such as GPS, InSAR, strainmeter, etc. One candidate is the repeating earthquakes, which rupture nearly the same asperity and can be used to accurately measure the amount of aseismic slip surrounding that asperity [*Vidale et al.*, 1994; *Nadeau et al.*, 1995; *Igarashi et al.*, 2003; *Matsuzawa et al.*, 2004; *Peng et al.*, 2005].

Various studies use the waveform cross-correlation coefficient (CCC) to identify repeating pairs [*Nadeau et al.*, 1995; *Peng and Ben-Zion*, 2006, etc.], and then group them into sequences. Additionally, many researchers use refined relocations to evaluate the overlapping fraction of source patches among different members in each repeating sequence [*Peng and Ben-Zion*, 2006; *Lengline and Marsan*, 2009]. This is applicable to cases when good station coverage exists, and generally fails for repeater studies offshore [e.g., *Igarashi et al.*, 2003; *Meng et al.*, 2015, etc.]. Mathematically, the waveform CCC is a value to quantify the similarity of two waveforms averaging across a given frequency band. This could be strongly affected by seismic waves with large amplitude at dominating frequencies. After taking this into consideration, recent studies also propose to utilize the coherence function to further measure the similarity at each frequency [*Lengline and Marsan*, 2009; *Materna et al.*, 2018].

Multiple studies have provided evidence for deep creep along the central San Jacinto Fault [*Wdowinski*, 2009; *Meng and Peng*, 2016; *Inbal et al.*, 2017, etc.]. We propose to conduct a systematic search of possible repeating earthquakes, which are expected if the deep part of the fault is creeping. I will briefly summarize some preliminary results obtained so far below, and introduce additional efforts to verify and categorize repeaters.

7.2 Study Region and Analysis Procedure

Figure 7.1 shows the study region around the central segment of the San Jacinto Fault. In details, I start with the relocated catalog events between 2010 and 2016 listed in *Hauksson et al.* [2012], and request the event waveform from Southern California Earthquake Data Center (SCEDC) using STP. Station AZ.SND (coordinates: 33.5519N, 116.6129W) within the Anza Gap (AG) is selected as the reference station, and ~60 stations within 50 km relative to AZ.SND are used in further analysis. I run cross-correlation among all selected event pairs (i.e., with epicentral distance less than 20 km) using an 8-s window starting 0.5 s before P arrivals (also from SCEDC) on vertical channels. A repeating pair is registered when the CCC is larger than 0.95 on at least 5 stations (see one example pair in Figure 7.2), similar to previous studies [e.g., *Meng et al.*, 2015].

7.3 Preliminary Results

A total number of ~11,500 repeating pairs are found, containing ~6,550 events with magnitudes between 0 and 3. This corresponds to nearly 20% of all examined earthquakes (33,100). The magnitude distribution of all members within above repeating pairs with time is shown in Figure 7.3. I identify a similar trend when compared to the

background seismicity: besides regular occurrence of repeating events, they seem to be modulated by large regional mainshock (*M*4.5+ Anza earthquakes). This could be a combination of both characteristic repeating earthquakes driven by fault creep and repeaters modulated by transient slip episodes (e.g., mainshock afterslip, earthquake swarms, etc.).

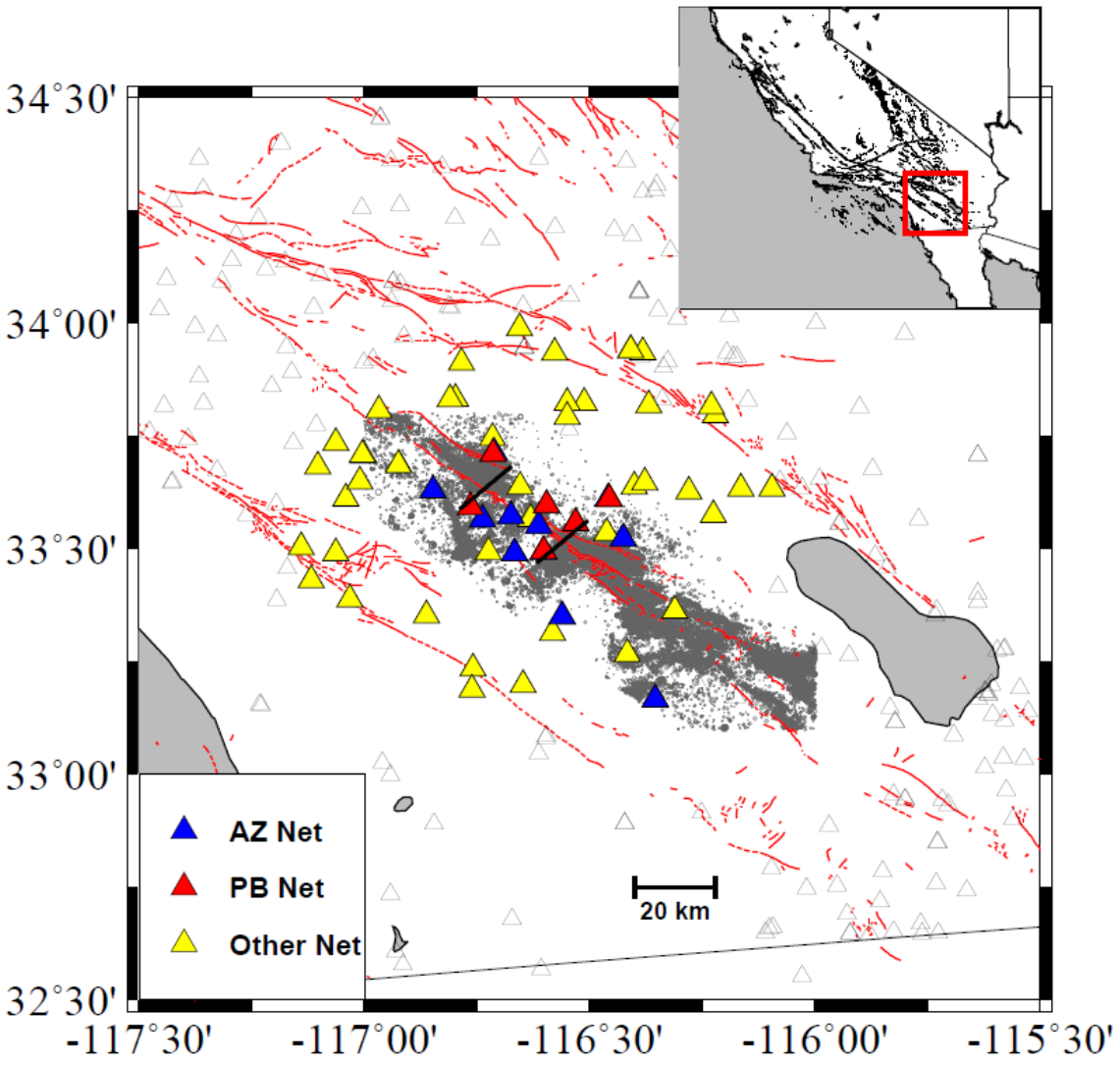

Figure 7.1 Study region around the central segment of San Jacinto Fault. Main map shows the relocated seismicity within 20km relative to the SJF (gray circles) between 2010 and 2016 [*Hauksson et al.*, 2012], used stations (filled triangles), and active faults (red dashed lines) in southern California. Insert outlines the study region in a bigger tectonic context.

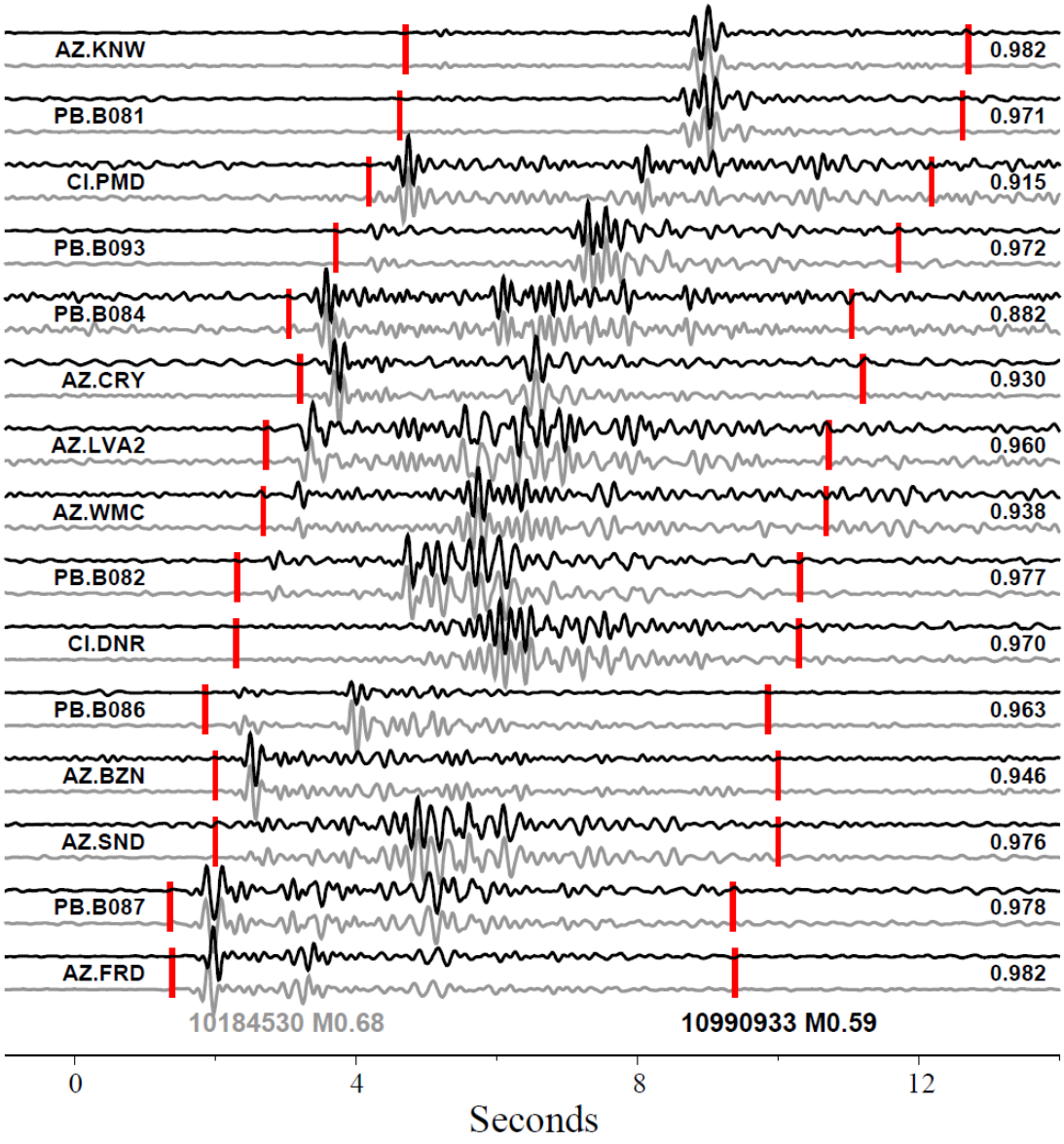

Figure 7.2 A repeating pair example. Waveforms of the M0.68 (ID 10184530, 2011-05-28 07:35:39.52) and M0.59 (ID 10990933, 2011-08-11 04:08:28.01) event are shown with gray and black colors. NET.STA and the CC values are marked on both sides, respectively. Red vertical bars show the windows for running CC.

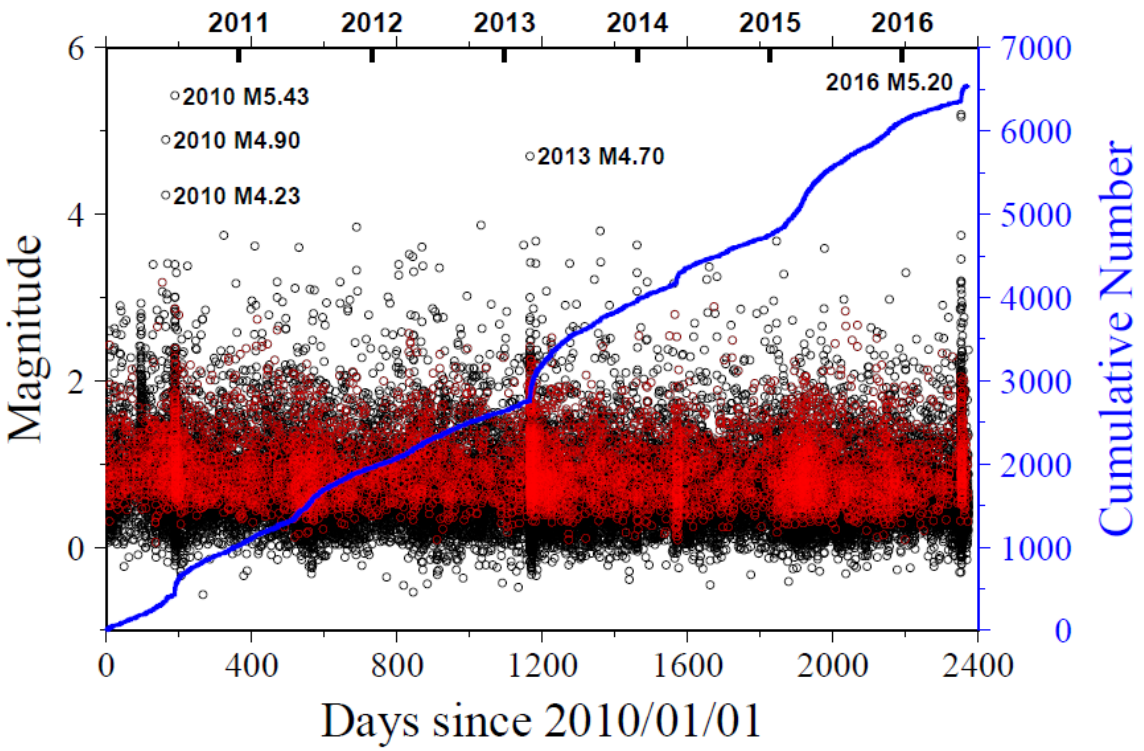

Figure 7.3 Magnitude vs. time for all exported event pairs between 2010 and 2016.

7.4 Discussion

The high percentage of repeating earthquakes among all examined events might be due to the inclusion of events spatially close to each other, but not true repeating earthquakes with nearly overlapping source patches. This leads to the question of how we set up a robust criterion for selecting repeating pairs. One option, as mentioned before, is to measure the mean coherence values at each frequency within a frequency band [*Lengline and Marsan*, 2009; *Materna et al.*, 2018], instead of using an averaged cross-correlation value, which could be dominated by waves of large amplitude at certain frequencies. Additional relocation could help to refined locations of sub-sample accuracy, but it requires a consistent network of relatively good station coverage. Motivated by recent studies [e.g., *Materna et al.*, 2018], I plan to implement the coherence method to

calculate the mean coherence value across pre-defined frequency ranges. An example below shows the comparison between the previous cross-correlation function and newly implemented coherence function (Figure 7.4). We note relatively high similarities between 4 and 10 Hz, while some differences exist at lower and higher frequencies. Considering their close timings and magnitude difference, it could be possible that the second event is a later "aftershock" type event occurring nearby. Our further analysis includes evaluating the identified repeaters, carefully clustering repeating pairs into sequences, and categorizing different types of repeaters.

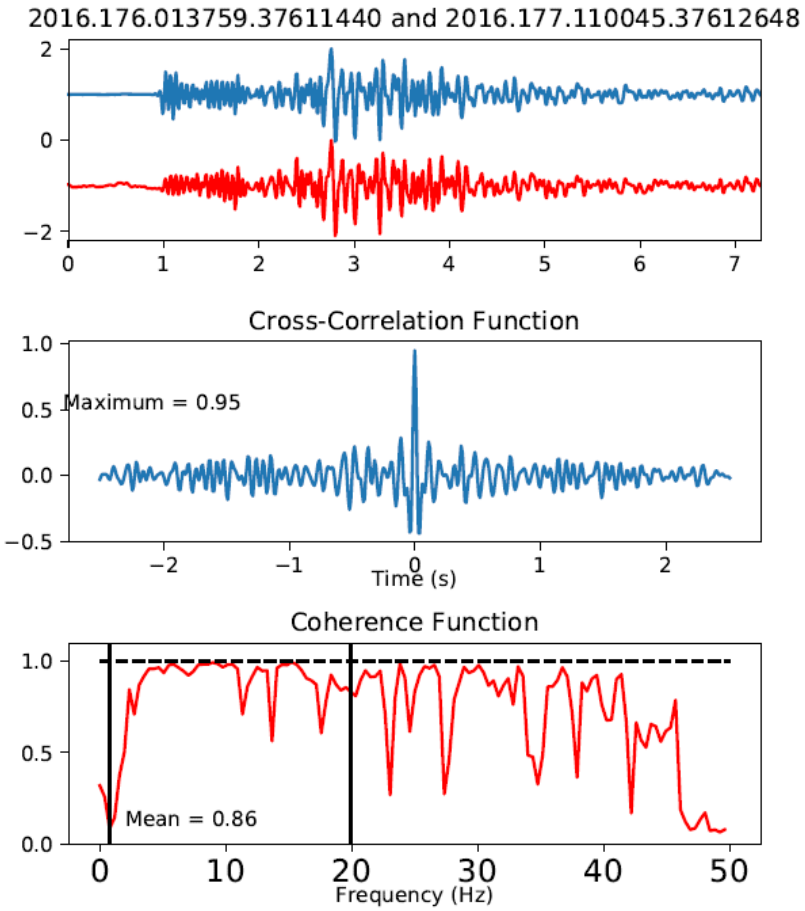

Figure 7.4 An example showing both cross-correlation and coherence functions.

CHAPTER 8. CONCLUSION AND FUTURE WORK

This dissertation included several studies on earthquake triggering and broad fault slip behaviors using updated earthquake catalogs after matched filter detection. I reported clear evidences of dynamically triggered earthquake near Gaize in South-Central Tibet following two M_w 8.5+ mainshock off the west coast of northern Sumatra [*Yao et al.*, 2015], within the North Island of New Zealand following the 2016 M_w 7.8 Kaikoura mainshock [*Yao et al.* (under review)]. For instantaneous triggering cases, triggered earthquake sequences last for shorter durations and decay following the Omori's law. On the other hand, secondary mechanisms (such as aseismic slip) are responsible for elongated or delayed triggered sequences.

Using the newly detected catalogs from the matched filter technique, we can obtain a better picture of seismicity evolution within an earthquake cycles. The long-term seismicity preceding the Wenchuan earthquake and foreshock activity before the El Mayor-Cucapah provide new insights on the mainshock nucleation process. Moreover, by carefully detecting and relocation aftershocks following the Nicoya mainshock, I showed how the megathrust continued to slip in the early stage after the mainshock.

As we shown in CHAPTER 3, the NWMFT strongly depends on the quality of templates and may result in more erroneous detections. It fails in cases where no prior catalog exists, or the quality of template catalog is poor, and generate erroneous "target signals" by passing the template information (location, magnitude, etc.) to its associated detections. In cases where no catalog event exists, one classic method is to build the initial catalog using the standard procedures (such as using Antelope [*Yao et al.*, 2015;

Walter et al., 2015]). Alternative approaches include source-scanning algorithm [*Kao and Shan*, 2004], auto-correlation [*Brown et al.*, 2008], a combination of both [*Frank et al.*, 2014], or local similarity method [*Li et al.*, 2018]. Besides using all existing catalog events as templates, and running cross-correlation in the time domain, researchers also suggest speeding up the computation using a subspace of templates [*Harris*, 2006], fingerprint [*Yoon et al.*, 2015], etc. Most recently the convolutional neural network (CNN) has been applied to phase picking and earthquake detection [*Ross et al.*, 2018; *Perol et al.*, 2018; *Zhu and Beroza*, 2018; *Zhu et al.*, 2018] and turned out to more generalized to different cases.

The above new advancements and challenges inspire me to recognize the limitations of the "conventional" template matching algorithm and devote additional efforts to go beyond it. Utilizing machine learning algorithms to efficiently detect events across a whole network and provide more event information could be one direction during my future academic career. Moreover, repeating earthquakes, together with different types of observations, would be used to quantify transient slip episodes, which could help to unravel how active faults move and release the accumulated strain in both slow and fast manners. I am also interested in combining observations with frictional models and numerical simulations to understand the physical process controlling the continuum of slip spectrum during my postdoctoral program in University of Michigan.

REFERENCES

Abercrombie, R. E., and J. Mori (1996), Occurrence patterns of foreshocks to large earthquakes in the western United States, *Nature*, 381(6580), 303-307.

Aiken, C., and Z. Peng (2014), Dynamic triggering of microearthquakes in three geothermal/volcanic regions of California, *J. Geophys. Res.*, 119, 9, 6992-7009.

Allen, R. V. (1982), Automatic phase pickers: their present use and future prospects, *Bull. Seismol. Soc. Am.*, 72, S225-S242.

Allmann, B. P., and P. M. Shearer (2009), Global variations of stress drop for moderate to large earthquakes, *J. Geophys. Res.*, 114, B01310, doi:10.1029/2008JB005821.

Anderson, J. G., J. N. Brune, J. N. Louie, Y. Zeng, M. Savage, G. Yu, Q. Chen, and D. dePolo (1994), Seismicity in the Western Great Basin Apparently Triggered by the Landers, California, Earthquake, 28 June 1992, *Bull. Seism. Soc. Am.*, 84, 3, 863-891.

Aron, A., and J. L. Hardebeck (2009), Seismicity rate changes along the central California coast due to stress changes from the 2003 M6.5 San Simeon and 2004 M6.0 Parkfield earthquakes, *Bull. Seism. Soc. Am.*, 99, 4, 2280-2292.

Bartlow, N. M., L. M. Wallace, R. J. Beavan, S. Bannister, and P. Segall (2014), Time-dependent modeling of slow slip events and associated seismicity and tremor at the Hikurangi subduction zone, New Zealand, *J. Geophys. Res. Solid Earth*, 119, 734–753, doi:10.1002/2013JB010609.

Beavan, J., L. M. Wallace, N. Palmer, P. Denys, S. Ellis, N. Fournier, S. Hreinsdottir, C. Pearson, and M. Denham (2016), New Zealand GPS velocity field: 1995–2013. *New Zeal. J. Geol. Geophys.*, 59(1), 5–14.

Beeler, N. M., D. A. Lockner, and S. H. Hickman (2001), A simple stick-slip and creep slip model for repeating earthquakes and its implication for micro-earthquakes at Parkfield, *Bull. Seismol. Soc. Am.*, 91, 1797–1804.

Ben-Zion, Y., and Zhu L. (2002), Potency-magnitude scaling relations for southern California earthquakes with 1.0 < Ml < 7.0, *Geophys. J. Int.*, 148, F1–F5.

Ben-Zion, Y. (2003), Appendix 2. Key formulas in earthquake seismology. In The IASPEI International Handbook of Earthquake and Engineering Seismology, Part B (eds. Lee, W.H.K., Kanamori, H., Jennings, P.C., and Kisslinger C.) (Academic Press, London 2003) pp. 1857–1875.

Bilek, S., W. Phillips, J. Walter, Z. Peng, S. Schwartz, M. Brudzinski, and D. Yao (2015), Source Parameters for Repeating Earthquakes along the Middle America Trench (invited),

Abstract S44A-01 presented at 2015 Fall Meeting, AGU, San Francisco, Calif., 14-18 Dec.

Brenguier, F., M. Campillo, T. Takeda, Y. Aoki, N. M. Shapiro, X. Briand, K. Emoto, and H. Miyake (2014), Mapping pressurized volcanic fluids from induced crustal seismic velocity drops, *Science*, 345(6192), 80-82.

Brodsky, E. E., and H. Kanamori (2004), The Physics of Earthquakes, *Rep. Prog. Physics*, 67(8), 1429-1496.

Brodsky, E. E., and S. G. Prejean (2005), New constraints on mechanisms of remotely triggered seismicity at Long Valley Caldera, *J. Geophys. Res.*, 110, B04302.

Brodsky, E. E. (2006), Long-range triggered earthquakes that continue after the wave train passes, *Geophys. Res. Lett.*, 33, L15313.

Brodsky, E. E., and N. J. van der Elst (2014), The use of dynamic earthquake triggering, *Annu. Rev. Earth Planet. Sci.*, 42, 317–339.

Brown, J. R., G. C. Beroza, and D. R. Shelly (2008), An autocorrelation method to detect low frequency earthquakes within tremor, *Geophysical Research Letters*, *35*(16).

Brown, J. R., G. C. Beroza, S. Ide, K. Ohta, D. R. Shelly, S. Y. Schwartz, W. Rabbel, M. Thorwart, and H. Kao (2009), Deep low-frequency earthquakes in tremor localize to the plate interface in multiple subduction zones, *Geophys. Res. Lett.*, 36, L19306, doi:10.1029/ 2009GL040027.

Bosl, W. J., and A. Nur (2002), Aftershocks and pore fluid diffusion following the 1992 Landers earthquake, *J. Geophys. Res.*, 107(B12), 2366, doi:10.1029/2001JB000155.

Bouchon, M., H. Karabulut, M. Aktar, S. Ozalaybey, J. Schmittbuhl, and M. P. Bouin (2011), Extended nucleation of the 1999 Mw 7.6 Izmit earthquake, *Science*, 331(6019), 877-880, doi: 10.1126/science.1197341.

Chao, K., Z. Peng, C. Wu, C.-C. Tang, and C.-H. Lin (2012), Remote triggering of non-volcanic tremor around Taiwan, *Geophys. J. Int.*, 188, 301-324.

Chaves, E. J., L. Duboeuf, S. Y. Schwartz, T. Lay, and J. Kintner (2017), Aftershocks of the 2012 M_w 7.6 Nicoya, Costa Rica, earthquake and mechanics of the plate interface, *Bull. Seismol. Soc. Am.* **107**, 1227–1239.

Chen, Z., B. C. Burchfiel, Y. Liu, R. W. King, L. H. Royden, W. Tang, E. Wang, J. Zhao, and X. Zhang (2000), Global Positioning System measurements from eastern Tibet and their implications for India/Eurasia intercontinental deformation, *J. Geophys. Res.*, 105, 16,215–16,227.

Chen, J., Q. Liu, S. Li, B. Guo, Y. Li, J. Wang, and S. Qi (2009), Seismotectonic study by relocation of the Wenchuan M_S 8.0 earthquake sequence [in Chinese with English abstract], *Chin. J. Geophys.*, 52, 390–397.

Chen, T., and N. Lapusta (2009), Scaling of small repeating earthquakes explained by interaction of seismic and aseismic slip in a rate and state fault model, *J. Geophys. Res.*, 114, B01311, doi:10.1029/2008JB005749.

Chen, X. W., and P. M. Shearer (2013), California foreshock sequences suggest aseismic triggering process, *Geophysical Research Letters*, *40*(11), 2602-2607.

Cochran, E. S., J. E. Vidale, and S. Tanaka (2004), Earth tides can trigger shallow thrust fault earthquakes, *Science*, *306*(5699), 1164-1166.

Cui, X., X. Hu, C. Yu, K. Tao, Y. Wang, and J. Ning (2011), Research on focal mechanism solutions of Wenchuan earthquake sequence, *Acta Sci. Nat. Univ. Pekinensis*, 6, 1063–1072.

DeMets, C., R. G. Gordon, and D. F. Argus (2010), Geologically current plate motions, *Geophys. J. Int.*, 181, 1–80, doi:10.1111/j.1365-246X. 2009.04491.x.

Deng, K., S. Zhou, R. Wang, R. Robinson, C. Zhao, and W. Cheng (2010). Evidence that the 2008 Mw 7.9 Wenchuan earthquake could not have been induced by the Zipingpu reservoir, *Bull. Seismol. Soc. Am.*, 100, no. 5B, 2805–2814.

DeShon, H. R., S. Y. Schwartz, A. V. Newman, V. Gonz ález, M. Protti, L. M. Dorman, T. H. Dixon, D. E. Sampson, and E. R. Flueh (2006), Seismogenic zone structure beneath the Nicoya Peninsula, Costa Rica, from three-dimensional local earthquake P- and S-wave tomography, *Geophys. J. Int.*, 164(1), 109–124.

Dieterich, J. H. (1979), Modeling of Rock Friction .2. Simulation of Pre-Seismic Slip, *J Geophys Res*, *84*(Nb5), 2169-2175.

Dixon, T. H, S. Y. Schwartz, J. M. Protti, V. Gonz ález, A. V. Newman, J. Marshall, and J. Spotila (2013), Detailed Data Available for Recent Costa Rica Earthquake, *EOS Trans. Amer. Geoph. Union.* 94(2), 17-18, doi:10.1002/2013EO02.

Dixon, T.H., Y. Jiang, R. Malservisi, R. McCaffrey, N. Voss, M. Protti, and V. Gonzalez (2014), Earthquake and tsunami forecasts: Relation of slow slip events to subsequent earthquake rupture, *Proc. Nat. Academy Science*, 111(48), 17039-17044, doi:10.1073/pnas.1412299111.

Dodge, D. A., G. C. Beroza, and W. L. Ellsworth (1996), Detailed observations of California foreshock sequences: Implications for the earthquake initiation process, *J Geophys Res-Sol Ea*, *101*(B10), 22371-22392.

Ellsworth, W. L. (2013), Injection-Induced Earthquakes, *Science*, *341*(6142), 142.

Ellsworth, W. L., and F. Bulut (2018), Nucleation of the 1999 Izmit earthquake by a triggered cascade of foreshocks, *Nature Geoscience*, 11, 531-535.

Enescu, B., J. Mori, and M. Miyazawa (2007), Quantifying early aftershock activity of the 2004 mid-Niigata Prefecture earthquake (*Mw* 6.6), *J. Geophys. Res.*, **112**, B04310, doi:10.1029/2006JB004629.

Evans, J. R., D. Eberhart-Phillips, and C. H. Thurber (1994), User's manual for SIMULPS12 for imaging Vp and Vp/Vs: A derivative of the ''Thurber'' tomographic inversion SIMUL3 for local earthquakes and explosions, U.S. Geol. Surv. Open File Rep., 94-431.

Felzer, K. R., R. E. Abercrombie, and G. Ekstrom (2004), A common origin for aftershocks, foreshocks, and multiplets, *Bulletin of the Seismological Society of America, 94*(1), 88-98.

Felzer, K. R., and E. E. Brodsky (2006), Decay of aftershock density with distance indicates triggering by dynamic stress, *Nature*, 441, 735–738.

Feng, L., A. V. Newman, M. Protti, V. González, Y. Jiang, and T. H. Dixon (2012), Active deformation near the Nicoya Peninsula, northwestern Costa Rica, between 1996 and 2010: Interseismic megathrust coupling, *J. Geophys. Res.*, 117, B06407, doi:10.1029/2012JB009230.

Frank, W. B., N. M. Shapiro, A. L. Husker, V. Kostoglodov, A. Romanenko, and M. Campillo (2014), Using systematically characterized low-frequency earthquakes as a fault probe in Guerrero, Mexico, *J. Geophys. Res.*, 119, 7686–7700.

Freed, A. (2005), Earthquake triggering by static, dynamic, and postseismic stress transfer, *Annu. Rev. Earth Planet. Sci.*, 33, doi: 10.1146/annurev.earth.33.092203.122505.

Gao, S., P. G. Silver, A. T. Linde, and I. S Sacks (2000), Annual modulation of triggered seismicity following the 1992 Landers earthquake in California, *Nature*, 406, 500–504.

Ge, S., M. Liu, N. Lu, J. W. Godt, and G. Lou (2009). Did the Zipingpu reservoir trigger the 2008 Wenchuan earthquake? *Geophys. Res. Lett.*, 36, no. 20, doi: 10.1029/2009GL040349.

Ghosh, A., A. V. Newman, A.M. Thomas, G. T. Farmer (2008), Interface Locking along the Subduction Megathrust from Microseismicity near Nicoya, Costa Rica, *Geophy. Res. Lett.*, **35** (L01301), doi:10.1029/2007GL031617.

Ghosh, A., J. E. Vidale, Z. Peng, K. C. Creager, and H. Houston (2009), Complex nonvolcanic tremor near Parkfield, California, triggered by the great 2004 Sumatra earthquake, *J. Geophys. Res.*, 114, B00A15.

Gibbons, S. J., and F. Ringdal (2006), The detection of low magnitude seismic events using array-based waveform correlation, *Geophys. J. Int.*, 165, 149-166.

Gomberg, J., P. Reasenberg, P. Bodin, and R. Harris (2001), Earthquake triggering by seismic waves following the Landers and Hector Mine earthquakes, *Nature*. 411, 462–466.

Gomberg, J., P. Bodin, K. Larson, and H. Dragert (2004), Earthquake nucleation by transient deformations caused by the M = 7.9 Denali, Alaska, earthquake, *Nature*, 427, 621-624.

Gupta, H. K. (2002), A review of recent studies of triggered earthquakes by artificial water reservoirs with special emphasis on earthquakes in Koyna, India**,** *Earth-Sci. Rev.*, 58, 279-310.

Hainzl, S. (2016), Rate-dependent incompleteness of earthquake catalogs, *Seismol. Res. Lett.*, 87(2A), 337–344, doi:10.1785/0220150211.

Hainzl, S., T. Fischer, H. Čermáková, M. Bachura, and J. Vlček (2016), Aftershocks triggered by fluid intrusion: Evidence for the aftershock sequence occurred 2014 in West Bohemia/Vogtland, *J. Geophys. Res. Solid Earth*, 121, 2575–2590.

Hamling, I. J., S. Hreinsdóttir, K. Clark, J. Elliott, C. Liang, E. J. Fielding, N. Litchfield, P. Villamor, L. M. Wallace, T. J. Wright, E. D'Anastasio, S. Bannister, D. Burbridge, P. Denys, P. Gentle, J. Howarth, C. Mueller, N. Palmer, C. Pearson, W. Power, P. Barnes, D. Barrell, R. Van Dissen, R. Langridge, T. Little, A. Nicol, J. Pettinga, J. Rowland, and M. Stirling (2017), Complex multi-fault rupture during the 2016 Mw 7.8 Kaikoura earthquake, New Zealand, *Science*, http://dx.doi.org/ 10.1126/science.aam7194.

Hao, K. X., H. Si, H. Fujiwara, and T. Ozawa (2009), Coseismic surface-ruptures and crustal deformations of the 2008 Wenchuan earthquake Mw7.9, China, *Geophys. Res. Lett.*, 36, L11303, doi:10.1029/2009GL037971.

Harris, D. (2006), Subspace detectors: Theory, *Lawrence Livermore Natl. Lab. Rep. UCRL–TR–222758*, 46 pp., Lawrence Livermore Natl. Lab., Livermore, Calif.

Harris, R. N., and K. Wang (2010), Thermal models of the Middle America Trench at the Nicoya Peninsula, Costa Rica, *Geophys. Res. Lett.*, 29(21), doi:10.1029/2002GL015406, 2002.

Harris, R. A., and R. W. Simpson (1998), Suppression of large earthquakes by stress shadows: A comparison of Coulomb and rate-and-state failure, *J. Geophys. Res.*, 103, 24,439–24,451, doi:10.1029/98JB00793.

Hauksson, E. (2010), Spatial Separation of Large Earthquakes, Aftershocks, and Background Seismicity: Analysis of Interseismic and Coseismic Seismicity Patterns in Southern California, *Pure Appl Geophys*, *167*(8-9), 979-997.

Hauksson, E., J. Stock, K. Hutton, W. Yang, J. A. Vidal-Villegas, and H. Kanamori (2011), The 2010 Mw 7.2 El Mayor-Cucapah earthquake sequence, Baja California,

Mexico and southernmost California, USA: Active seismotectonics along the Mexican Pacific Margin, *Pure Appl. Geophys.*, **168**, 1255–1277.

Hauksson, E., W. Yang, and P. M. Shearer (2012), "Waveform Relocated Earthquake Catalog for Southern California (1981 to 2011)", *Bull. Seismol. Soc. Am.*, 102(5), 2239-2244, doi: 10.1785/0120120010.

Helmstetter, A., D. Sornette, and J. R. Grasso (2003), Mainshocks are aftershocks of conditional foreshocks: How do foreshock statistical properties emerge from aftershock laws, *J. Geophys. Res.-Sol. Ea.*, *108*(B1).

Hill, D. P., and S. G. Prejean (2015), Dynamic triggering, 2nd edition, *Treatise on Geophysics*, Vol. 4, ed. Kanamori, H., Elsevier, Amsterdam.

Hobbs, T. E., C. Kyriakopoulos, A. V. Newman, M. Protti, and D. Yao (2017), Large and primarily updip afterslip following the 2012 M_w 7.6 Nicoya, Costa Rica, earthquake, *J. Geophys. Res. Solid Earth*, 122.

Holden, C., Y. Kaneko, E. D'Anastasio, R. Benites, B. Fry, and I. J. Hamling (2017), The 2016 Kaikōura earthquake revealed by kinematic source inversion and seismic wavefield simulations: Slow rupture propagation on a geometrically complex crustal fault network, *Geophy. Res. Lett.*, 44, 11,320–11,328.

Hough, S. E., L. Seeber, and J. G. Armbruster (2003), Intraplate triggered earthquakes: observations and interpretation, *Bull. Seism. Soc. Am.*, 93, 2212-2221.

Hsu, Y., et al. (2006), Frictional afterslip following the 2005 Nias-Simeulue earthquake, Sumatra, *Science*, 312, 1921–1926, doi:10.1126/science.1126960.

Hu, X. P., C. Q. Yu, K. Tao, X. F. Cui, J. Ning, and Y. H. Wang (2008), Focal mechanism solutions of Wenchuan earthquake and its strong aftershocks obtained from initial *P* wave polarity analysis [in Chinese], *Chin. J. Geophys.*, 51(6), 1711–1718.

Huang, Y., J. P. Wu, T. Z. Zhang, and D. N. Zhang (2008), Relocation of the M_s 8.0 Wenchuan earthquake and its aftershock sequence, *Sci. China Ser.*, 12, 1703–1711.

Hurst, T., A. D. Jolly, and S. Sherburn (2014), Precursory characteristics of the seismicity before the 6 August 2012 eruption of Tongariro volcano, North Island, *New Zealand. J. Volcanol. Geotherm. Res.*, 286, 294–302.

Hutnak, M., et al. (2007), The thermal state of 18–24 Ma upper lithosphere subducting below the Nicoya Peninsula, northern Costa Rica margin, in The Seismogenic Zone of Subduction Thrust Faults, edited by T. Dixon, and J. C. Moore, pp. 86–122, Columbia University Press, New York.

Igarashi, T., T. Matsuzawa, and A. Hasegawa (2003), Repeating earthquakes and interplate aseismic slip in the northeastern Japan subduction zone, *J. Geophys. Res.*, 108(B5), doi:10.1029/2002JB001920.

Inbal, A., Ampuero, J., and J. P. Avouac (2017), Locally and remotely triggered aseismic slip on the central San Jacinto Fault near Anza, CA, from joint inversion of seismicity and strainmeter data, *J. Geophys. Res. Solid Earth*, 122, 3033-3061.

Jiang, T., Z. Peng, W. Wang, and Q.-F. Chen (2010), Remotely triggered seismicity in continental China following the 2008 Mw 7.9 Wenchuan earthquake, *Bull. Seism. Soc. Am.*, 100, 5B, 2574-2589.

Jiang, Y., S. Wdowinski, T. H. Dixon, M. Hackl, M. Protti, and V. Gonz á lez (2012), Slow slip events in Costa Rica detected by continuous GPS observations, 2002–2011, *Geochem. Geophys. Geosyst.*, 13, Q04006, doi:10.1029/2012GC004058.

Jones, L. M., and P. Molnar (1979), Some Characteristics of Foreshocks and Their Possible Relationship to Earthquake Prediction and Premonitory Slip on Faults, *J Geophys Res*, *84*(Nb7), 3596-3608.

Jolly, A. D., S. Sherburn, P. Jousset, and G. Kilgour (2010), Eruption source processes derived from seismic and acoustic observations of the 25 September 2007 Ruapehu eruption-North Island, *New Zealand. J. Volcanol. Geotherm. Res.*, 191(1–2), 33–45.

Kaiser, A. E., N. Balfour, B. Fry, C. Holden, N. Litchfield, M. Gerstenberger, E. D'Anastasio, N. Horspool, G. McVerry, J. Ristau, K. Gledhill, S. Bannister, A. Christopherson, K. Clark, W. Power, D. Rhoades, I. J. Hamling, L. M. Wallace, J. Mountjoy, Y. Kaneko, R. A. Benites, C. Van Houtte, C. Massey, S. Dellow, and S. Hreinsdottir (2017), The 2016 Kaikoura (New Zealand) earthquake: preliminary seismological report, *Seismol. Res. Lett.*, 88 (3). http://dx.doi.org/10.1785/0220170018.

Kanamori, H., and D. L. Anderson (1975), Theoretical basis of some empirical relations in seismology, *Bull. Seismol. Soc. Am.*, 65, 1073–1095.

Kao, H., and S. Shan (2004), The source-scanning algorithm: mapping the distribution of seismic sources in time and space, *Geophys. J. Int.*, 157(2), 589–594.

Kapp, P., A. Yin, T. M. Harrison, and L. Ding (2005), Cretaceous-Tertiary shortening, basin development, and volcanism in central Tibet, *Geol. Soc. Am. Bull.*, 117, 865–878.

Kasahara, K., Earthquake Mechanics (Cambridge University Press, New York 1981).

Kato, A., and T. Igarashi (2012), Regional extent of the large coseismic slip zone of the 2011 Mw 9.0 Tohoku-Oki earthquake delineated by on-fault aftershocks, *Geophys. Res. Lett.*, 39, L15301, doi:10.1029/2012GL052220.

Kato, A., K. Obara, T. Igarashi, H. Tsuruoka, S. Nakagawa, and N. Hirata (2012), Propagation of slow slip leading up to the 2011 Mw 9.0 Tohoku-Oki earthquake, *Science*, 335, 705-708.

Kato, A., and K. Obara (2014), Step-like migration of early aftershocks following the 2007 Mw 6.7 Noto-Hanto earthquake, Japan, *Geophys. Res. Lett.*, 41, 3864-3869, doi:10.1002/2014GL060427.

Kato, A., and S. Nakagawa (2014), Multiple slow-slip events during a foreshock sequence of the 2014 Iquique, Chile Mw 8.1 earthquake, *Geophys. Res. Lett.*, 41, 15, 5420–5427.

Kilb, D., J. S. Gomberg, and P. Bodin (2000), Triggering of earthquake aftershocks by dynamic stresses, *Nature*. 408, 570–574.

Kilb, D., J. Gomberg, and P. Bodin (2002), Aftershock triggering by complete Coulomb stress changes, *J. Geophys. Res.*, 107, B4, ESE 2-1–ESE 2-14.

King, G. C. P., R. S. Stein, and J. Lin (1994), Static stress changes and the triggering of earthquakes, *Bull. Seismol. Soc. Am.*, 84, 935–953.

King, G. C. P, and M. H. Devès (2015), Fault Interaction, Earthquake Stress Changes and the Evolution of Seismicity, *Treatise on Geophysics*, Edition: Elsevier, Chapter 7, doi: 10.1016/B978-0-444-53802-4.00077-4.

Klein, F. W. (2002), User's guide to HYPOINVERSE2000, a Fortran program to solve for earthquake locations and magnitudes, U.S. Geol. Surv. Open File Rep., 02, 172, 123 pp., 01−113, Menlo Park, California.

Kyriakopoulos, C., A. V. Newman, A. M. Thomas, M. Moore-Driskell, and G. T. Farmer (2015), A new seismically constrained subduction interface model for Central America, *J. Geophys. Res.*, *120*, doi:10.1002/2014JB011859.

Kyriakopoulos, C., and A. V. Newman (2016), Structural Asperity focusing locking and earthquake slip along the Nicoya megathrust, Costa Rica, *J. Geophys. Res. Solid Earth*, 121, doi: 10.1002/2016JB012886.

Lay et al. (2005), The great Sumatra-Andaman earthquake of 26 December 2004, *Science*, 308, 5725, 1127-1133.

Lay, T. (2015), The surge of great earthquakes from 2004 to 2014, *Earth Planet. Sci. Lett*, 409, 133-146, doi: 10.1016/j.epsl.2014.10.047.

Li, C., Z. Peng, D. Yao, H. Guo, Z. Zhan, and H. Zhang (2018), Abundant aftershock sequence of the 2015 M_w7.5 Hindu Kush intermediate-depth earthquake, *Geophys. J. Int.*, 213, 2, 1121–1134, https://doi.org/10.1093/gji/ggy016.

Li, G., A. J. West, A. L. Densmore, Z. Jin, R. N. Parker, and R. G. Hilton (2014), Seismic mountain building: Landslides associated with the 2008 Wenchuan earthquake in the context of a generalized model for earthquake volume balance, *Geochem. Geophys. Geosyst.*, 15, 833–844, doi:10.1002/2013GC005067.

Li, L., D. Yao, X. Meng, Z. Peng, and B. Wang (2017), Increasing seismicity in Southern Tibet following the 2015 Mw 7.8 Gorkha, Nepal earthquake, *Tectonophysics*, http://dx.doi.org/10.1016/j.tecto.2016.08.008.

Li, Z., and Z. Peng (2016), An automatic phase picker for local earthquakes with predetermined locations: Combining a signal-to-noise ratio detector with 1D velocity model inversion, *Seismol. Res. Lett.*, 87(6), doi: 10.1785/0220160027.

Li, Z., Z. Peng, D. Hollis, L. Zhu, and J. McClellan (2018), High-resolution seismic event detection using local similarity for Large-N arrays, *Scientific Report*, 8:1646, doi: 10.1038/s41598-018-19728-w.

Liu, C., A. Linde, and I. Sacks (2009), Slow earthquakes triggered by typhoons, *Nature*, *459*(7248), 833-836.

Lei, X. L. (2011), Possible roles of the Zipingpu Reservoir in triggering the 2008 Wenchuan earthquake, *J. Asian Earth Sci.*, 40, 844–854.

Lei, J., and D. Zhao (2009), Structural heterogeneity of the Longmenshan fault zone and the mechanism of the 2008 Wenchuan earthquake (*Ms* 8.0), *Geochem. Geophys. Geosyst.*, **10**, Q10010, doi:10.1029/2009GC002590.

Lengliné, O., B. Enescu, Z. Peng, and K. Shiomi (2012), Decay and expansion of the early aftershock activity following the 2011, Mw 9.0 Tohoku earthquake, *Geophys. Res. Lett.*, 39, L18309.

Lengline, O, and D. Marsan (2009), Inferring the coseismic and postseismic stress changescaused by the 2004 Mw= 6 Parkfield earthquake from variationsof recurrence times of microearthquakes, *Journal of Geophysical Research*, 114, B10303, doi:10.1029/2008JB006118.

Lu, X., X. Zhang, L. Zhou, and Z. Zhang (2010), Accurate relocation and analysis of earthquakes in the Zipingpu reservoir area, Sichuan, China, Earthquake, 30, 2, pp. 10-19 (in Chinese).

Lundgren, P., M. Protti, A. Donnellan, M. Heflin, E. Hernandez, and D. Jefferson (1999), Seismic cycle and plate margin deformation in Costa Rica: GPS observations from 1994 to 1997, *J. Geophys. Res.*, 104, 28,915–28,928.

Ma, W., C. Xu, X. Zhang, X. Xu, H. Li, and J. Yuan (2011). Study on the relationship between the reservoir-induced seismicity at Zipingpu reservoir and the Ms 8.0 Wenchuan earthquake, *Seismol. Geol.*, 33, no. 1, 175–190 (in Chinese).

Materna, K., T. Taira, and R. Bürgmann (2018), Aseismic transform fault slip at the Mendocino Triple Junction from characteristically repeating earthquakes, *Geophys. Res. Lett.*, 45, 10.1002/2017GL075899

Matsuzawa, T., N. Uchida, T. Igarashi, T. Okada, and A. Hasegawa (2004), Repeating earthquakes and quasi-static slip on the plate boundary east off northern Honshu, Japan, *Earth Planets Space*, 56, 803–812.

Matthews, M. V., and P. A. Reasenberg (1988), Statistical methods for investigating quiescence and other temporal seismicity patterns, *Pure and Applied Geophysics*, 126, 357–372.

Meng, L., H. Huang, R. Bürgmann, J. P. Ampuero, and A. Strader (2015), Dual megathrust slip behaviors of the 2014 Iquique earthquake sequence, *Earth Planet. Sci. Lett.*, 411, 177–187.

Meng, X., X. Yu, Z. Peng, and B. Hong (2012), Detecting earthquakes around Salton Sea following the 2010 M_w7.2 El Mayor-Cucapah earthquake using GPU parallel computing, *Procedia Computer Science.*, 9, 937-946, doi:10.1016/j.procs.2012.04.100.

Meng, X., Z. Peng, and J. L. Hardebeck (2013), Seismicity around Parkfield correlates with static shear stress changes following the 2003 Mw 6.5 San Simeon earthquake, *J. Geophys. Res.*, 118, 3576–3591.

Meng, X., and Z. Peng (2014), Seismicity rate changes in the San Jacinto Fault Zone and the Salton Sea Geothermal Field following the 2010 Mw 7.2 El Mayor-Cucapah Earthquake, *Geophys. J. Int.*, 197, 3, 1750-1762.

Meng, X., and Z. Peng (2016), Increasing lengths of aftershock zones with depths of moderate‐size earthquakes on the San Jacinto Fault suggests triggering of deep creep in the middle crust, *Geophys. J. Int.*, 204(1), 250–261, doi:10.1093/gji/ggv445.

McGarr, A., D. Simpson, and L. Seeber(2002), Case histories of induced and triggered seismicity, in *International Handbook of Earthquake and Engineering Seismology*, vol. 81A, pp. 647–661, Academic Press, San Francisco, Calif.

McGuire, J. J., M. S. Boettcher, and T. H. Jordan (2005), Foreshock sequences and short-term earthquake predictability on East Pacific Rise transform faults, *Nature*, *434*(7032), 457-461.

Mignan, A. (2014), The debate on the prognostic value of earthquake foreshocks: A meta-analysis, *Sci Rep-Uk*, *4*.

Mogi, K. (1962), Magnitude frequency relations for elastic shocks accompanying fractures of various materials and some related problems in earthquakes, *Bull. Earthquakes Res. Inst. Univ. Tokyo*, *40*, 831-853.

Miyazawa, M., and J. Mori (2006), Evidence suggesting fluid flow beneath Japan due to periodic seismic triggering from the 2004 Sumatra-Andaman earthquake, *Geophys. Res. Lett.*, 33, L05303.

Moore-Driskell, M., H. R. DeShon, W. Rabbel, M. Thorwart, Y. Dzierma, and I. G. Arroyo (2013), Integration of arrival-time datasets for consistent quality control: A case study of amphibious experiments along the Middle America Trench, *Bull. Seismol. Soc. Am.*, 103(5), 2752–2766, doi:10.1785/0120120274.

Nabelek et al. (2009), Underplating in the Himalaya-Tibet Collison Zone Revealed by the Hi-CLIMB Experiment, *Science*, 325, 1371-1374.

Nadeau, R. M., W. Foxall, and T. V. McEvilly (1995), Clustering and periodic recurrence of microearthquakes on the San Andreas fault at Parkfield, California, *Science*, 267, 503–507.

Nadeau, R.M., and L.R. Johnson (1998), Seismological studies at Parkfield VI: moment release rates and estimates of source parameters for small repeating earthquakes, *Bull. Seismol. Soc. Am.*, 88, 790–814.

Newman, A. V., S. Y. Schwartz, V. Gonzalez, H. R. DeShon, J. M. Protti and L. Dorman (2002), Along-Strike Variability in the Updip Limit of the Seismogenic Zone Below Nicoya Peninsula, Costa Rica, *Geoph. Res. Lett.*, **29(**20), 38:1-4.

Newman, A. V., D. Yao, C. Kyriakopoulos, M. Moore-Driskell, T. E. Hobbs, Z. Peng, S. Y. Schwartz, M. Protti and V. Gonzalez (2016), The Possible Decapitation of a Megathrust Indenter: Evidence from Imaging of Time-dependent Microseismic Structures before and after the 2012 Mw 7.6 Nicoya, Costa Rica, Abstract T53A-01 presented at 2016 Fall Meeting, AGU, San Francisco, Calif., 12-16 Dec.

Nicol, A., and J. Beavan (2003), Shortening of an overriding plate and its implications for slip on a subduction thrust, central Hikurangi Margin, *New Zealand. Tectonics.*, 22(6), 1070, doi:10.1029/2003TC001521.

Ogata, Y. (1988), Statistical-Models for Earthquake Occurrences and Residual Analysis for Point-Processes, *J. Am. Stat. Assoc.*, *83*(401), 9-27.

Ogata, Y. (2006), Fortran programs statistical analysis of seismicity -updated version (point process data), EPTREN, LINLIN, SIMBVP, LINSIM and PGRAPH included in Time Series and Control Program Package, SASeis2006, *Computer Science Monograph, No. 33*.

Ohnaka, M. (1992), Earthquake Source Nucleation - a Physical Model for Short-Term Precursors, *Tectonophysics*, *211*(1-4), 149-178.

Omori, F. (1894), On the aftershocks of earthquakes, *J. Coll. Sci., Imp. Univ. Tokyo*, *7*, 111-200.

Papadopoulos, G. A. (2002), The Athens, Greece, earthquake (Ms 5.9) of 7 September 1999: an event triggered by the İzmit, Turkey, 17 August 1999 earthquake? *Bull. Seism. Soc. Am.*, 92, 1, 312-321.

Peng, Z., J. E. Vidale, C. Marone, and A. Rubin (2005), Systematic variations in recurrence interval and moment of repeating aftershocks, *Geophys. Res. Lett.*, 32, L15301, doi:10.1029/2005GL022626.

Peng, Z., and Y. Ben-Zion (2005), Spatiotemporal variations of crustal anisotropy from similar events in aftershocks of the 1999 M7.4 İzmit and M7.1 Düzce, Turkey, earthquake sequences, *Geophys. J. Int.*, 160, 1027–1043, doi:10.1111/j.1365-246X.2005.02569.x.

Peng, Z., J. E. Vidale, and H. Houston (2006), Anomalous early aftershock decay rate of the 2004 Mw6.0 Parkfield, California, earthquake, *Geophys. Res. Lett.*, 33, L17307, doi:10.1029 /2006GL026744.

Peng, Z., and Y. Ben-Zion (2006), Temporal changes of shallow seismic velocity around the Karadere-Duzce branch of the north Anatolian fault and strong ground ground motion, *Pure Appl. Geophysics*, 163, 567-599, doi:10.1007/s00024-005-0034-6.

Peng, Z., J. E. Vidale, M. Ishii, and A. Helmstetter (2007), Seismicity rate immediately before and after main shock rupture from high-frequency waveforms in Japan, *J. Geophys. Res.*, 112, B03306, doi:10.1029/2006JB004386.

Peng, Z., and P. Zhao (2009), Migration of early aftershocks following the 2004 Parkfield earthquake, *Nature Geosci.*, 2, 877-881.

Peng, Z., J. E. Vidale, A. G. Wech, R. M. Nadeau, and K. C. Creager (2009), Remote triggering of tremor along the San Andreas Fault in central California, *J. Geophys. Res.*, 114, B00A06.

Peng, Z., and J. Gomberg (2010), An integrated perspective of the continuum between earthquakes and slow-slip phenomena, *Nature Geosci.*, 3, 599–607.

Peng, Z., W. Wang, Q.-F. Chen, and T. Jiang (2010), Remotely triggered seismicity in north China following the 2008 Mw 7.9 Wenchuan earthquake, *Earth Planets Space*, 62, 893-898.

Peng, Z., D. R. Shelly, and W. L. Ellsworth (2015), Delayed dynamic triggering of deep tremor along the Parkfield‐Cholame section of the San Andreas Fault following the 2014 *M*6.0 South Napa earthquake, *Geophys. Res. Lett.*, 42, 7916–7922.

Peng, Z., B. Fry, K. Chao, D. Yao, X. Meng, and A. Jolly (2018), Remote triggering of microearthquakes and tremor in New Zealand following the 2016 M7.8 Kaikoura earthquake, *Bull. Sci. Soc. Am.*, doi: 10.1785/0120170327,

Perfettini, H., and J.-P. Avouac (2004), Postseismic relaxation driven by brittle creep: A possible mechanism to reconcile geodetic measurements and the decay rate of aftershocks, application to the Chi-Chi earthquake, Taiwan, *J. Geophys. Res.*, 109, B02304, doi:10.1029/2003JB002488.

Perfettini, H., and J.-P. Avouac (2007), Modeling afterslip and aftershocks following the 1992 Landers earthquake, *J. Geophys. Res.*, 112, B07409, doi:10.1029/2006JB004399.

Perol, T., M. Gharbi, and M. Denolle (2018), Convolutional neural network for earthquake detection and location, *Science Advances*, 4(2), e1700578.

Pollitz, F. F., R. Bürgmann, R. S. Stein, and V. Sevilgen (2014), The profound reach of the 11 April 2012 M 8.6 Indian Ocean earthquake: Short-term global triggering followed by a longer-term global shadow, *Bull. Seism. Soc. Am.*, 104, 2, 972-984.

Press, W., Flannery, B., Teukolsky, S. and Vetterling, W. (1986), Numerical Recipes, Cambridge University Press, Cambridge.

Protti, M., M. F. Güendel, and E. Malavassi (2001), Evaluación del Potencial Sísmico de la Península de Nicoya, 1st ed., 144 pp., Ed. Fund. Univ. Nac., Heredia, Costa Rica.

Protti, M, Alfaro-Diaz, R, Brenn, G R, Fasola, S, Murillo, A, Marshall, J S, Gardner, T W, (2013) Identical Aftershocks from the Main Rupture Zone 10 Months After the Mw=7.6 September 5, 2012, Nicoya, Costa Rica, Earthquake, Abstract G23B-0787 presented at 2013 Fall Meeting, AGU, San Francisco, Calif., 9-13 Dec.

Protti, M., V. González, A. V. Newman, T. H. Dixon, S. Y. Schwartz, J. S. Marshall, L. Feng, J. I. Walter, R. Malservisi and S. E. Owen (2014), Nicoya Earthquake Rupture Anticipated by Geodetic Measurements of the Locked Plate Interface, *Nature Geoscience*, *7*(2), 117-121, doi: 10.1038/ngeo2038.

Reasenberg, P. A., and D. Oppenheimer (1985), FPFIT, FPPLOT, and FPPAGE: Fortran computer programs for calculating and displaying earthquake fault-plane solutions, U.S. Geol. Surv. Open-File Rep. 85-739.

Ross, Z. E, M. A. Meier, E. Hauksson, and T. H. Heaton (2018), Generalized seismic phase detection with deep learning, submitted to *Bull. Seismol. Soc. Am.*, under review.

Royden, L. H., B. C. Burchfiel, B. C., and R. D. van der Hilst (2008), The Geological Evolution of the Tibetan Plateau, *Science*, 321, 1054-1058.

Ruan, X., X. Meng, Z. Peng, F. Long, and R. Xie (2017), Microseismic activity in the last five months before the M_w7.9 Wenchuan Earthquake, *Bull. Seism. Soc. Am.*, 107(4), 1582–1592.

Ryder, I., R. Bürgmann, and J. Sun (2010), Tandem afterslip on connected fault planes following the 2008 Nima-Gaize (Tibet) earthquake, *J. Geophys. Res.*, 115, B03404.

Ryder, I., and R. Bürgmann (2011), Communication between multiple large earthquakes at different spatial scales across and beyond the Tibetan Plateau, American Geophysical Union, Fall Meeting 2011, abstract #S21D-07.

Ryder, I., R. Bürgmann, and E. Fielding (2012), Static stress interactions in extensional earthquake sequences: An example from the South Lunggar Rift, Tibet, *J. Geophys. Res.*, 117, B09405.

Savage, J. C., and M. D. Wood (1971), The relation between apparent stress and stress drop, *Bull. Seismol. Soc. Am.*, 61, 1381–1388.

Schaff, D. P., G. C. Beroza (1998), and B. E. Shaw, Postseismic response of repeating aftershocks, *Geophys. Res. Lett.*, 25, 4549–4552.

Schaff, D. P., G. H. R. Bokelmann, G. C. Beroza, F. Waldhauser, and W. L. Ellsworth (2002), High-resolution image of Calaveras Fault seismicity, *J. Geophys. Res.*, 107(B9), 2186, doi:10.1029/2001JB000633.

Schaff, D. P., and G. C. Beroza (2004). Coseismic and postseismic velocity changes measured by repeating earthquakes, *J. Geophys. Res.*, 109, B10302, doi:10.1029/2004JB003011.

Schwartz, S. Y., and H. R. Deshon (2007), Distinct updip limits to geodetic locking and microseismicity at the northern Costa Rica seismogenic zone: Evidence for two mechanical transitions, in The Seismogenic Zone of Subduction Thrust Faults, edited by T. Dixon and J. C. Moore, pp. 576–599, Columbia University Press, New York.

Schwartz, S. Y., and J. M. Rokosky (2007), Slow slip events and seismic tremor at circum-Pacific subduction zones, *Rev. Geophys.*, 45, RG3004.

Scholz, C. H. (1990), The Mechanics of Earthquakes and Faulting, Cambridge University Press, New York.

Shelly, D., G. Beroza, and S. Ide (2007), Non-volcanic tremor and low-frequency earthquake swarms, *Nature*, 446(7133), 305–307.

Shelly, D. R., and J. L. Hardebeck (2010), Precise tremor source locations and amplitude variations along the lower-crustal central San Andreas Fault, *Geophysical Research Letters*, *37*.

Shelly, D. R., Z. Peng, D. P. Hill., and C. Aiken (2011), Triggered creep as a possible mechanism for delayed dynamic triggering of tremor and earthquakes, *Nature Geosci.*, 4, 384-388.

Shelly, D. R., D. P. Hill, F. Massin, J. Farrell, R. B. Smith, and T. Taira (2013), A fluid-driven earthquake swarm on the margin of the Yellowstone caldera, *J. Geophys. Res. Solid Earth*, 118,4872–4886, doi:10.1002/jgrb.50362.

Silver, P. (1998), Why is earthquake prediction so difficult? *Seism. Res. Lett.*, 69, 111–113.

Simpson, D. W. (1976), Seismicity changes associated with reservoir loading, *Eng. Geol.*, 10, 123–150.

Skoumal, R. J., M. R. Brudzinski, B. S. Currie, and J. Levy (2014), Optimizing multi-station earthquake template matching through re-examination of the Youngstown, Ohio, sequence, *Earth Plant. Sc. Lett.*, 405, 274–280, doi: 10.1016/j.epsl.2014.08.033.

Stankova-Pursley, J., S. L. Bilek, W. S. Phillips, and A. V. Newman (2011), Along-strike variations of earthquake apparent stress at the Nicoya Peninsula, Costa Rica, subduction zone, *Geochem. Geophys. Geosyst*, 12, Q08002.

Stein, R. S., G. C. P. King, and J. Lin (1994), Stress triggering of the 1994 M = 6.7 Northridge, California, earthquake by its predecessors, *Science*, 265, 1432–1435.

Stein, R. S., A. A. Barka, and J. H. Dieterich (1997), Progressive failure on the North Anatolian fault since 1939 by earthquake stress triggering, *Geophys. J. Int.*, 128, 594–604.

Stein, R. S. (1999), The role of stress transfer in earthquake occurrence, *Nature*, *402*(6762), 605-609.

Su, J., and T. Chen (2012), The application of S wave polarization analysis in determining the focal depth of the Ms 8.0 Wenchuan earthquake, *Recent Developments in World Seismology* (in Chinese Abstract), 6:189.

Sun, W. F., Z. Peng, C. H. Lin, and K. Chao (2015), Detecting deep tectonic tremor in Taiwan with a dense array, *Bull. Seismol. Soc. Am.*, 105(3), 1349–1358.

Tang, C.-C., Z. Peng, K. Chao, C.-H. Chen, and C.-H. Lin (2010), Detecting low-frequency earthquakes within non-volcanic tremor in southern Taiwan triggered by the 2005 Mw 8.6 Nias earthquake, *Geophys. Res. Lett.*, 37, L16307.

Tang, C.-C., C.-H. Lin and Z. Peng (2014), Spatio-temporal evolutions of early aftershocks following te 2010 ML 6.4 Jiashian earthquake in Southern Taiwan, *Geophys. J. Int.*, 199, 1772-1783, doi:10.1093/gji/ggu361.

Tao, W., and Z. Shen (2008), Heat flow distribution in Chinese continent and its adjacent areas, *Progress in Natural Science*, 18, 843-849.

Tao, W., T. Masterlark, Z. K. Shen, and E. Ronchin (2015), Impoundment of the Zipingpu reservoir and triggering of the 2008 M_w 7.9 Wenchuan earthquake, China, *J. Geophys. Res. Solid Earth*, 120, 7033–7047, doi: 10.1002/2014JB011766.

Tape, C., S. Holtkamp, V. Silwal, J. Hawthorne, Y. Kaneko, J. P. Ampuero, C. Ji, N. Ruppert, K. Smith, and M. E. West (2018), Earthquake nucleation and fault slip complexity in the lower crust of central Alaska, *Nature Geoscience*, 11, 536-541.

Taylor, M., and A. Yin (2009), Active structures of the Himalayan-Tibetan orogen and their relationships to earthquake distribution, contemporary strain field, and Cenozoic volcanism, *Geosphere*, 5, 3, 199-214.

Thurber, C., H. Zhang, F. Waldhauser, J. Hardebeck, A. Michael, and D. Eberhart-Phillips (2006), Three-dimensional compressional wavespeed model, earthquake relocations, and focal mechanisms for the Parkfield, California, region, *Bull. Seismol. Soc. Am.*, 96, 38-49.

Tong, X., D. T. Sandwell, and Y. Fialko (2010), Coseismic slip model of the 2008 Wenchuan earthquake derived from joint inversion of interferometric synthetic aperture radar, GPS, and field data, *J. Geophys. Res.*, 115, B04314, doi:10.1029/2009JB006625.

Towns, J., T. Cockerill, M. Dahan, I. Foster, K. Gaither, A. Grimshaw, V. Hazlewood, S. Lathrop, D. Lifka, G. D. Peterson, R. Roskies, J. R. Scott and N. Wilkins-Diehr (2014), "XSEDE: Accelerating Scientific Discovery", *Computing in Science & Engineering*, vol.16, no. 5, pp. 62-74, doi:10.1109/MCSE.2014.80.

Utsu, T., Y. Ogata, and R. Matsu'ura (1995), The centenary of the Omori formula for a decay law of aftershock activity, *Journal of Physics of the Earth*, *43*(1), 1-33.

van der Elst, N. J., and E. E. Brodsky (2010), Connecting near-field and far-field earthquake triggering to dynamic strain, *J. Geophys. Res.*, 115, B07311.

van der Elst, N. J., E. E. Brodsky, and T. Lay (2013), Remote triggering not evident near the epicenters of impending great earthquakes, *Bull. Seism. Soc. Am.*, 103, 1522-1540.

Velasco, A. A, S. Hernandez, T. Parsons, and K. Pankow (2008), Global ubiquity of dynamic earthquake triggering, *Nature Geosci.*, 1, 375-379.

Vidale, J. E., W. L. Ellsworth, A. Cole, and C. Marone (1994), Variations in rupture process with recurrence interval in a repeated small earthquake, *Nature*, 368, 624–626.

Wang, W., Meng, X., Peng, Z., Chen, Q. F., & Liu, N. (2015). Increasing background seismicity and dynamic triggering behaviors with nearby mining activities around Fangshan Pluton in Beijing, China, *Journal of Geophysical Research: Solid Earth*, 120, 5624–5638.

Waldhauser, F., and W. L. Ellsworth (2000), A double-difference earthquake location algorithm: Method and application to the northern Hayward Fault, California, *Bull. Seismol. Soc. Am.*, 90, 1353–1368, doi:10.1785/0120000006.

Wallace, L. M., and J. Beavan (2010), Diverse slow slip behavior at the Hikurangi subduction margin, New Zealand, *J. Geophys. Res.*, 115, B12402.

Wallace, L. M., J. Beavan, R. McCaffrey, and D. Darby (2004), Subduction zone coupling and tectonic block rotations in the North Island, New Zealand., *J. Geophys. Res.*, 109, B12406, doi:10.1029/2004JB003241.

Wallace, L. M., Y. Kaneko, S. Hreinsdotir, I. J. Hamling, Z. Peng, N. Bartlow, E. D'Anastasio, and B. Fry (2017), Large-scale dynamic triggering of shallow slow slip enhanced by overlying sedimentary wedge, *Nat. Geosci.*, doi: 10.1038/ngeo3021.

Wallace, L. M., S. Hreinsdottir, S. Ellis, I. J. Hamling, E. D'Anastasio, and P. Denys (2018), Triggered slow slip and afterslip on the southern Hikurangi subduction zone following the Kaikōura earthquake, *Geophys. Res. Lett.*, 45.

Walter, J. I., S. Y. Schwartz, J. M. Protti, and V. Gonzalez (2011), Persistent tremor within the northern Costa Rica seismogenic zone, *Geophys. Res. Lett.*, 38, L01307, doi:10.1029/2010GL045586.

Walter, J. I., S. Y. Schwartz, M. Protti, and V. Gonzalez (2013), The synchronous occurrence of shallow tremor and very low frequency earthquakes offshore of the Nicoya Peninsula, Costa Rica, *Geophys. Res. Lett.*, 40, 1517–1522, doi:10.1002/grl.50213.

Walter, J. I., X. Meng, Z. Peng, S. Y., Schwartz, A. V., Newman and M. Protti (2015), Far-field triggering of foreshocks near the nucleation zone of the 5 September 2012 (MW 7.6) Nicoya Peninsula, Costa Rica earthquake, *Earth and Planetary Science Letters*, 431, 75-86, doi: 10.1016/j.epsl.2015.09.017.

Wang, T., S. Wei, X. Shi, Q. Qiu, L. Li, D. Peng, R. J. Weldon, and S. Barbot (2018), The 2016 Kaikōura earthquake: Simultaneous rupture of the subduction interface and overlying faults, *Earth and Planetary Science Letters*, 482, 44–51.

Wdowinski, S. (2009), Deep creep as a cause for the excess seismicity along the San Jacinto fault, *Nat. Geosci.*, 2, 882–885, doi:10.1038/ngeo684.

Wessel, P., and W. Smith (1991), Free software helps map and display data, Eos Trans. AGU, 72, 441, 445–446.

Wei, B., P. Chen, F. Li, and H. Huang (1992), Focal mechanisms and tectonic stress field of the Xinfengjiang earthquake, *Acta Seismologica Sinica*, 5, 3, 539-548.

Wei, S., et al. (2010), Regional earthquakes in northern Tibetan Plateau: Implications for lithospheric strength in Tibet, *Geophys. Res. Lett.*, 37, L19307.

Wei, S., et al. (2011), Superficial simplicity of the 2010 El Mayor-Cucapah earthquake of Baja California in Mexico, *Nat. Geosci.*, 4, 615–618.

West, M., J. J. Sanchez, and S. R. McNutt (2005), Periodically triggered seismicity at Mount Wrangell, Alaska, after the Sumatra Earthquake, *Science*, 308, 5725, 1144-1146.

Wessel, P., W. H. F. McNutt, R. Scharroo, J. Luis, and F. Wobbe (2013), Generic Mapping Tools: Improved Version Released, *Eos Trans. AGU*, 94, 45, 409.

Wiemer, S. (2001), A software package to analyze seismicity: ZMAP, *Seism. Res. Lett.*, 72, 3, 373-382.

Williams, C. A., D. Eberhart-Phillips, S. Bannister, D. H. N. Barker, S. Henrys, M. Reyners, and R. Sutherland (2013), Revised interface Geometry for the Hikurangi Subduction Zone, New Zealand, *Seismol. Res. Lett.*, 84(6), 1066–1073.

Wu, C., Z. Peng, W. Wang, and Q.-F Chen (2011), Dynamic triggering of shallow earthquakes near Beijing, China, *Geophys. J. Int.*, 185, 3, 1321-1334.

Wu, C., X. Meng, Z. Peng, and Y. Ben-Zion (2014), Lack of spatiotemporal localization of foreshocks before the 1999 Mw 7.1 Düzce, Turkey, earthquake, *Bull. Seismol. Soc. Am.*, 104(1), 560–566.

Xu, W., G. Feng, L. Meng, A. Zhang, J. P. Ampuero, R. Bürgmann, and L. Fang (2018), Transpressional rupture cascade of the 2016 M_w 7.8 Kaikoura earthquake, New Zealand, *J. Geophys. Res.*, 123, 2396–2409. https://doi.org/10.1002/2017JB015168.

Xu, X., X.Wen, G. Yu, G. Chen, Y. Klinger, J. Hubbard, and J. Shaw (2009). Coseismic reverse- and oblique-slip surface faulting generated by the 2008 Mw 7.9 Wenchuan earthquake, China, *Geology*, 37, 515–518.

Yang, H., L. Zhu, and R. Chu (2009), Fault-plane determination of the 18 April 2008 Mount Carmel, Illinois, earthquake by detecting and relocating aftershocks, *Bull. Seism. Soc. Am.*, 99(6), 3413-3420.

Yang, Z., Y. Chen, J. Su, T. Chen, and P. Wu (2012), The hypocenter and origin time of the M_w7.9 Wenchuan earthquake of May 12, 2008 [in Chinese], *Acta Seismol. Sin.*, 34(2), 127–136.

Yao, D., Z. Peng and X. Meng (2015), Systematical search for remotely triggered earthquakes in Tibetan Plateau following the 2004 M 9.0 Sumatra and 2005 M 8.6 Nias earthquakes, *Geophys. J. Int.*, 201(2), 543–551, doi: 10.1093/ gji/ggv037.

Yao, D., Z. Peng, X. Meng, X. Chen, R. Castro, and S. Deng, Comprehensive Detection and Relocation of the 2010 Mw 7.2 El Mayor-Cucapah Foreshock Sequence, in prep.

Yao, D., J. I. Walter, X. Meng, T. E. Hobbs, Z. Peng, A. V. Newman, S. Y. Schwartz, and M. Protti (2017), Detailed spatio-temporal evolution of microseismicity and repeating earthquakes following the 2012 M_w7.6 Nicoya earthquake, *J. Geophys. Res. Solid Earth*, 121, doi:10.1002/2016JB013632.

Yao, D., Z. Peng, C. Daniels, and X. Meng, Systematic Search for Repeating Earthquakes along the Central San Jacinto Fault, in prep.

Yao, D., Z. Peng, Y. Kaneko, B. Fry, and X. Meng (2018), Isolated Locations of Dynamically Triggered Earthquakes in the North Island of New Zealand Following the 2016 M_w7.8 Kaikoura Earthquake, *Earth and Planetary Science Letters*, submitted.

Yao, D., Z. Peng, X. Ruan, X. Meng, F. Long, and J. Su, Microseismicity before the 2008 Mw 7.9 Wenchuan earthquake and its relationship with nearby water reservoir, in prep.

Yin Y., F. Wang, and P. Sun (2009), Landslide hazards triggered by the 2008 Wenchuan earthquake, Sichuan, China. *Landslides*, 6:139–151.

Yoon, C., O. O'Reilly, K. Bergen, and G. Beroza (2015), Earthquake detection through computationally efficient similarity search, *Sci. Adv.*, 1, doi:10.1126/sciadv.1501057.

Yue, H. T. Lay, S. Y. Schwartz, L.Rivera, M. Protti, T. H. Dixon, S. Owen, and A. V. Newman (2013), The 5 September 2012 Nicoya, Costa Rica Mw 7.6 earthquake rupture process from joint inversion of high-rate GPS, strong-motion, and teleseismic P wave data and its relationship to adjacent plate boundary interface properties, *J. Geoph. Res.* 118, 5453-5466, doi:10.1002/jgrb.50379.

Yukutake, Y., M. Miyazawa, R. Honda, M. Harada, H. Ito, M. Sakaue, K. Koketsu, K., and A. Yoshida (2013), Remotely triggered seismic activity in Hakone volcano during and after the passage of surface waves from the 2011 M9.0 Tohoku-Oki earthquake, *Earth and Planetary Science Letters*, 373, 205-216.

Zhang, P., Z. Shen, M. Wang, W. Gan, R. Burgmann, and P. Molnar (2004), Continuous deformation of the Tibetan Plateau from global positioning system data, *Geology*, 32, 809–812.

Zhang, H., and C. H. Thurber (2003), Double-difference tomography: The method and its application to the Hayward fault, California, *Bull. Seismol. Soc. Am.*, 93, 1875–1889.

Zhang, M., and L. Wen (2015), An effective method for small event detection: Match and locate (M&L), *Geophys. J. Int.*, 200(3), 1523–1537.

Zhang, X., J. Yan, X. Zhang, L. Yan, and C. Zhao (2013), The aftershock determination of hypocenter and origin time of the Mw 7.9 Wenchuan earthquake of May 12, 2008, *Earthquake Research in China*, 2, 230-235 (in Chinese).

Zheng, Y., H. Ma, J. Lv, S. Ni, Y. Li, and S. Wei (2009), Source mechanism of strong aftershocks (M_s5.6) of the 2008/05/12 Wenchuan earthquake and the implication for seismotectonics, *Sci. China Ser. D*, 52(6), 739–753.

Zhu, W., and G. C. Beroza (2018), PhaseNet: A Deep-Neural-Network-Based Seismic Arrival Time Picking Method, *Geophys. J. Int.*, submitted.

Zhu, L., Z. Peng, J. McClellan, C. Li, D. Yao, Z. Li, and L. Fang (2018), Deep learning for seismic phase detection and picking in the aftershock zone of 2008 Mw 7.9 Wenchuan Earthquake, *Phys. Earth Planet. Inter.*, submitted.